Visualization and modeling of evaporation from pore networks by representative 2D micromodels

Der Fakultät für Geowissenschaften, Geotechnik und Bergbau
der Technischen Universität Bergakademie Freiberg
eingereichte

DISSERTATION

zur Erlangung des akademischen Grades
Doktor der Naturwissenschaften
Dr. rer. nat
vorgelegt

von MSc. Yi Ding
geboren am 23.04.1990 in Gansu, China

Freiberg, 13.02.2022

Table of Contents

List of Equations

List of Figures

List of Tables

Abbreviations

BF	Bulk flow
CF	Corner flow
CLD	Chord length distribution
CRP	constant rate period
E	Evaporation
ET	Evapotranspiration
FIB-SEM	Focused Ion Beam Scanning Electron Microscopy
FRP	Falling rate period
ICP-DRIE	Inductively coupled plasma-deep reactive ion etching
IP	Image processing
IPE	Isolated pore evaporation
IWC	Isolated water cluster
LB	Liquid bridge
LR	Liquid ring
LUT	Lookup table
micro-CT	Microcomputed tomography
MM4-glass	Glass-ceramic micromodel with irregular pore structure
MM4-Si	Silicon micromodel with irregular pore structure
MM5-glass	Glass-ceramic micromodel with regular pore structure
MM5-Si	Silicon micromodel with regular pore structure
PSD	Pore size distribution
PT	Pore throat
REV	Representative elementary volume
RH	Relative humidity
SEM	Scanning electron microscopy
SSC	Single square capillary
T	Transpiration
TFF	Thick-film flow

Nomenclature

$\Delta m_w(t_c)$	Cumulated water mass loss at detachment time, applied in SSC-model
$\Delta m_w(x_2)$	Cumulated water mass loss in stage 2, applied in SSC-model
$\langle j_x^{diff} \rangle$	Mass evaporation rate density
$\langle Q_{ev} \rangle$	Averaged evaporation flux
$\langle v \rangle$	Average velocity of corner flow
ΔC	Vapor concentration difference
Δm	The evaporative mass loss calculated by image processing

Δm_{tot}	Evaporative mass loss in IPE model
Δm_w	Evaporated water mass loss, applied in SSC-model
ΔP_w	Water pressure difference
A	Cross sectional area
a	Half of the pore width in IPE model
$A(\theta)$	Contact angle dependent cross sectional area of corner flow
A_{cross}	Surface pore area, applied in the IPE model
A_{eq}	An equivalent cross sectional area of micromodel for evaporation only occuring in vertical direction
$A_{gw}^{fractal}$	The fractal gas-water interface of evaporation front
A_g	Cross sectional area of the gas phase for diffusion
A_g^0	Approximated A_g by a square cross section
a_i, *(i=0,1,2,3,4,5,6)*	θ and T dependent constants defined in Eq. 2.2.22b, 2.2.22c, 2.2.23b, 2.2.24b, 2.2.24c, 2.2.26c and 2.2.26c, respectively
$b(\theta, T)$	Key variable of the SSC-model given in Eq.2.2.15b
B_0	Bond number
C(z,y)	Vapor concentration field, applied in IPE model
C^*, $C^*(\theta)$	θ-dependent constant given in Eq.2.2.8b
C_1, C_2, C_3	Best polynomial fitting parameters of Eq.2.2.37a
Ca	Capillary number
C_a	Ambient vapor concentration
C_s	Saturated vapor concentration
$C_s(molar)$	Saturated vapor molar concentration
D	The wavelength parameter to estimate surface roughness
d	Micromodel depth
d_0	Mean pore width in SSC model
D_{diff}	Diffusion coefficient of the ambient air, applied in the IPE model
D_g^{eff}	Effective vapor diffusion coefficient of the water molecules inside the porous media
d_{eff}	Effective capillary width in stage 2 in SSC model
D_f	Fractal dimension
d_{FT}	The film thickness of TFF
D_g^0, $D_g^0(T)$	Molecular diffusion coefficient
d_{mean}	Mean pore width of MM5 structure
$e(t)$	Evaporation rate, applied in the IPE model
$f(\theta)$	Defined variable in Eq.2.2.34
F_c	Capillary forces
f_k, *i=1,2,3…k*	Defined variable in Eq.2.2.32
g	Gravitational acceleration
$g(\theta)$	Defined variable in Eq.2.2.36
$H(r_1, r_2)$	Mean curvature of water meniscus, dependent on the principal curvature radii r_1 and r_2
$H(r_x, r_y)$	Mean curvature of water meniscus, dependent on the curvature radii in principal directions x and y, applied in the SSC model
h_0	The mean height of the first layer grains in micromodel
h_{BL}	The mean depth of the equivalent water table when stage 1 starts in MM4 micromodels

h_c	Capillary height
$I(x, x_2)$	Integral defined in Eq.2.2.9d
I_{gw}	Water-gas interface
$j_y(z, y)$	Diffusive flux density, applied in the IPE model
k	Permeability
$k(r)$	The rate constant of a certain active pore with radius r, applied in the IPE model
k_{diff}	Diffusion rate constant, applied in the IPE model
k_{REV}	The ensemble average of the rate constant for REV scale, applied in the IPE model
L	Pipe length in Hagen-Poiseuille equation
L_c	Characteristic depth of drying front
L_e	Length of the fractal evaporation front
L_G	Gravitational length
L_m	Micromodel width (= 80mm)
L_{uc}	Length of unit cell in IPE model
L_{visc}, $L_{visc}(t, T)$	Viscous length
m_0	Total water capacity of the evaporating section in a capillary
M_0	The total water capacity of micromodel
M_{H_2O}	The water molar mass
$m_{loss}(t)$	Cumulative mass loss
m_{tot}	Total evaporation mass loss
m_w	The residual water mass in the corners of the evaporating section in a capillary
m_{w0}	Water mass of the liquid phase in the volume element dV
N	The number of boxes of the box counting method in Eq.4.6.1
N_{uc}	Number of unit cells, applied in the IPE model
P_c	Capillary pressure
P_g	Gas phase pressure
P_h	Hydrostatic pressure
$P_{vapor}(T)$	Saturated vapor pressure
P_w	Water phase pressure
$P_{w,BF}$	Water phase pressure of bulk flow
$P_{w,CF}$	Water phase pressure of corner flow
$P_{w,TFF}$	Water phase pressure of thick-film flow
Q	Volumetric flow rate
Q_{ev}, $Q_{ev}(t,T)$	Vapor flux / evaporation rate
Q_w	Internal water flow (CF or TFF)
q_w	Water flux
Q_{wc}, $Q_{wc}(x, t, \theta)$	Corner flow flux
Q_{wf}	Thick-film flow flux
r	Pore radius
R	The ideal gas constant
R^2	Regression coefficient
$r(x, y)$	Curvature radius of corner flow meniscus in SSC model
r_0	Half of the mean capillary width d_0

R_0	Pipe radius in Hagen-Poiseuille equation
r_1	The low limit of pore size, applied in the IPE model
r_2	The high limit of pore size, applied in the IPE model
R_a	The mean surface height as parameter to estimate surface roughness
r_{BF}	Curvature radius of bulk flow
r_c	Critical radius which divides the PSD into active and inactive pores, applied in the IPE model
r_{CF}	Curvature radius of corner flow
r_{cf}	Cuvature radius at corner flow front tip
r_F	Degree of roughness
R_H	Curvature radius of the water-gas meniscus in IPE model
r_i	Equivalent radius of the wet square pore, applied in the IPE model
r_{mean}	Mean pore radius of MM4 structure
r_{min}	Lower integration limit of radius in the continuous IPE model
r_p	Curvature radius at the corner flow root, applied in the SSC model
r_{tf}	Curvature radius at thick-film flow front tip
r_{TFF}	Curvature radius of thick-film flow
r_x	Curvature radius of corner flow meniscus in x-direction in SSC model
r_y, $r_y(x,t)$	Curvature radius of corner flow meniscus in y-direction in SSC model
S_w	The residual water saturation calculated by image processing
t	Time
T	Temperature
t_c	Detachment time of hydraulic connectivity at open surface
tetatc	Contact angle derived by $t_c$extrapolation
u	Dimensionless form of the axial velocity of corner flow
u_w	Receding velocity of percolation front
V	Control volume
$v(r,\emptyset,x)$	Axial velocity of corner flow expressed by cylindrical coordinate system
$V_{cap}(r,r_c)$	The cap volume of an air-invaded pore, applied in the IPE model
$V_{tube}(r,r_c)$	The tube volume of an air-invaded pore, applied in the IPE model
$w(t)$	The CF/TFF region extension
$\tilde{x}$	Defined variable in Eq.2.2.31b
x_1	Position of mean percolation front, applied in the SSC model
x_2	Position of mean evaporation front, applied in the SSC model
x_i	Evaporation front depth
x_p	Mean percolation front depth
$-x_\Sigma$	Position of water meniscus, applied in SSC model

Greek Letters

α	Corner angle
$\alpha(\theta)$	Rescaled flow resistance from $\beta(\theta)$
$\alpha(r,r_c)$	r and r_c determined angle in IPE model, Eq. 2.1.9b

$\beta, \beta(\theta)$	Dimensionless flow resistance
Δ	Difference (e.g., $\Delta r = r_1 - r_2$)
δ	Boundary layer thickness
ε	Defined variable in Eq.2.2.29b
ε_0	The box size of box counting method in Eq.4.6.1
θ	Contact angle
θ_c	Critical contact angle for the complete-wetting condition defined in Eq.4.5.1
θ_{t_c}	Contact angle derived by t_c extrapolation
θ_{x_p}	Contact angle derived by x_p extrapolation
θ_0	The intrinsic contact angle
θ_{2D}	Surface water content
$\mu(T)$	Temperature dependent dynamic viscosity
μ_w	Dynamic viscosity of water
$v_w(T)$	Kinematic viscosity of water
$\xi(x)$	Defined variable in Eq.2.2.21b
$\xi^n(x)$,*n=0,1,2,3…n*	The n-th proximation of $\xi(x)$
$\rho, \rho(x,t)$	Normalized curvature radius
ρ_w	Water density
Σ	Water meniscus
σ	Surface tension
σ_{gw}	Interfacial tension of gas-water interface
τ	The tortuosity
ϕ	2D porosity of the porous medium
ϕ_{eq}	The equivalent evaporation front porosity
ϕ_s	Ratio of the dry part of the surface area
$\phi(x)$	Defined variable in Eq.2.2.13b

Units

cm	Centimeter
g	gram
h	Hour
m	Meter
mg	miligram
min	Minute
mm	Millimeter
mol	Mole
nm	Nanometer
s	Second
μm	Micrometer

Acknowledgement

When I look back the last five years, I feel so grateful to what I have in my life and I feel so thankful to a lot of people who gave me inspirations, encouragements and help. I want to thank my supervisors Prof. Dr. Helmut Geistlinger and Prof. Dr. Moh'd Amro, and Dr. Anne Routschek, Prof. Dr. Conrad Jackisch, Prof. Dr. Jürgen Schmidt and Dr. Corina Dunger from Institut für Bohrtechnik und Fluidbergbau, TU Freiberg, for offering me the opportunity as PhD candidate and the support and guidance during my PhD period. The most valuable thing I learned from Prof. Dr. Helmut Geistlinger is the strict, precise and scientific way of thinking in research work, as a young scientist, I should be responsible for every comment I make with truly scientific arguments and I should be honest about my experimental results as the basic respect for doing research work.

I also want to thank the colleagues in the Department of Soil System Science at Helmholtz Center for Environmental Research (UFZ), for their support and kindness when I worked there as guest student. Particularly, I want to thank Bernd Apelt and Dr. John Maximilian Köhne for their technical help in the lab, Dr. Steffen Schlüter, Dr. Wei Gao, Dr. Frederic Leuther and Saeed Golmohammadi for their scientific advices, Prof. Dr. Hans-Jörg Vogel and Frau Antje Heyne for their administrative help.

Moreover, many special thanks to my families, my husband and my parents in China gave me constant support and understanding through my entire PhD period, my German parents and grandparents in-law gave me plenty of support and love when I was away from my homeland. I feel so grateful by their unconditional love and their encouragement to make my own decisions in every step of my life. I will also thank my friends in Halle and Leipzig, many of them were doing PhD at the same time with me, we shared our difficulties in life and work and we supported each other as always.

Last, I want to thank for the financial support from the Deutsche Forschungsgemeinschaft (DFG), and thank for the reviewers to review this thesis and the referees who will participate in my PhD thesis defence.

1 Introduction

Evapotranspiration (ET; Fig. 1.1) is a fundamental component of the global hydrologic cycle where 60% of the terrestrial precipitation feeds back to the atmosphere by direct soil evaporation (20%) or plant transpiration (40%) (Oki and Kanae, 2006), and consumes nearly 25% of the incoming solar radiation energy (Trenberth et al., 2009). It is necessary to provide reliable partitioning of the evapotranspiration into soil evaporation (E) and plant transpiration (T) for the hydrological and climate models, and water resource management. It is especially crucial to provide accurate soil evaporation estimations in the semi-arid and arid regions, also the agricultural fields during bare or partially covered soil periods (Merlin et al., 2016).

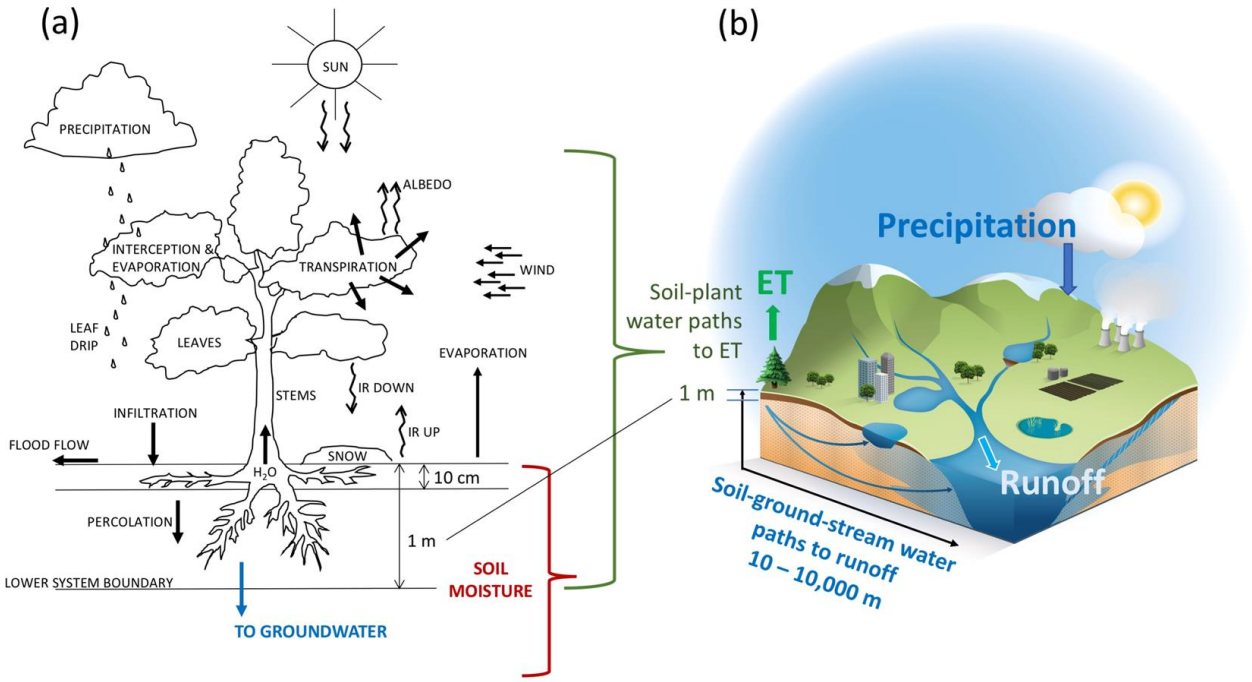

Figure 1. 1 Schematic conceptualization of (a) the near-surface soil-plant water system feeding actual evapotranspiration (ET), and (b) the full surface and subsurface hydrological catchment system feeding both ET and runoff/stream discharge (Figure 1; Ghajarnia et al., 2020).

The ground-based observational methods, for example, the eddy covariance (Baldocchi et al., 2001) or Bowen Ratio energy balance methods (Robock et al., 2003; Spittlehouse and Black, 1980) measure the total ET flux, soil evaporation can only be estimated during the period when plant transpiration is negligible (e.g. seasonal senescence; Abolafia-Rosenzweig et al., 2020). Some ground-based measurement, e.g. weighing lysimeter, can provide soil evaporation estimation directly, but is labor

consumed and difficult to be applied at regional scale for long-term monitoring (Abolafia-Rosenzweig et al., 2020). Land surface models can provide spatially and temporally continuous estimation of ET and the components. However, the simulated component flux is determined by model structure and parameters, uncertainties in one parameter can easily cause errors in the others (Lawrence et al., 2007). Global land surface models often applies the Penman method or Penman-Monteith method (Penman, 1948; Monteith, 1965), which utilizes the weather components of solar radiation, relative humidity, wind run and air temperature to estimate a reference crop ET (Burt et al., 2005). The known FAO-56 (Allen et al., 1998) adopted the Penman-Monteith method and became a global standard based on meteorological data. The FAO-56 presented the crop coefficient procedure which computes both E and T components of crop ET, but the application is problematic in regions where climate data are limited (Cordova et al., 2015; Stöckle et al., 2004; Trajkovic and Kolakovic, 2009; Li et al., 2012; Rahimikhoob et al., 2012), especially for tropical regions (Wohl et al., 2012) and high-altitude areas (Kollas et al., 2014). Remote sensing is an alternative for ET estimation. Many remote sensing methods estimate the ET largely based on thermal data as the key input for the ET algorithm (Kustas et al., 1999; Allen et al., 2007; Anderson, 1997; Bastiaanssen et al., 1998). The algorithms only provide the total ET flux rather than the individual components of ET, which can be applicable for the soil evaporation estimation only at the locations where the transpiration is known to be zero, e.g., over bare soil (Small et al., 2018). Small et al. (2018) proposed an approach to estimate direct evaporation from soil which uses the SMAP data (Soil Moisture Active Passive from NASA's satellite) as a lysimeter, the soil moisture change is resulted by the sum of vertical flux (runoff), transpiration and evaporation. However, the approach cannot be applied during overpass intervals with precipitation exceeding 2 mm as the infiltration in the applied water balance equation was considered as zero.

Physical models for estimating surface evaporation from soil properties give direct calculation, not being constrained by the partitioning of ET. The models are often explained by evaporation dynamics, hence, facing less spatial and seasonal uncertainties of the parameters as the semi-empirical or empirical models. The predictions of physical models achieved agreements with field data and other global models (Or & Lehmann, 2019; Balugani et al., 2018; Lehmann et al., 2018; Wang et al., 2019), showing great potentials to be applied and incorporated in land surface models and remote sensing estimations. Physically, soil evaporation is the transition of soil water to vapor phase and escape to the above atmosphere, which involves mass and energy transport. The main difficulty to present a solid evaporation model is the ambiguities regarding the processes that control evaporation rates, as reported by literatures, including the soil water transport (capillary flow; Lehmann et al., 2008); vapor diffusion from either the soil surface or the receding vaporization plane (Or et al., 2013); evaporation resistance related to surface water content

(Lehmann et al., 2018; Merlin et al., 2016); enhancement factors due to temperature gradients in the soil (Philip & Vries, 1957); and atmospheric demand (temperature, humidity and air velocity; Lehmann et al., 2008).

Under the low atmospheric demand (<5mm/d; Shahraeeni et al., 2012), evaporation rate from an initially saturated porous medium often exhibits a two-stage behavior, that stage-1 is a constant rate period (CRP) and stage 2 is a falling rate period (FRP; Brutsaert & Chen, 1995). In stage-1, there is liquid continuity from the saturated zone upwards till the soil surface due to capillary flow, which keeps the vaporization plane at the soil surface and maintains a constant evaporation rate. The transition from stage 1 to stage 2 occurs when the drying front recedes to a characteristic depth L_c (determined by soil properties; Lehmann et al., 2008), the capillary forces (against gravitational and viscous dissipation) can no longer ensure the liquid continuity till the soil surface and a dry soil layer develops (Balugani et al., 2018). As the vaporization plane recedes below the soil surface in stage 2, water moves only as vapor diffusion through the dry soil layer. Many models have applied the concept of L_c (Or & Lehmann, 2019; Balugani et al., 2018; Lehmann et al., 2008, 2018; Shahraeeni et al., 2012), that, the liquid phase above the drying front is close to hydrostatic equilibrium and L_c can be derived by the soil hydraulic properties (e.g. pore size distribution, retention curve). These models only consider the capillary flow through the pore ducts, which is driven by the capillary pumping from large pores to small pores. However, other studies have proved the retained liquid films in surface crevices (roughness) and angular corners facilitate and dominate evaporation, as the films lead to a stronger capillary flow than the duct flow and provide hydraulic conductivity for mass transport (Tuller and Or, 2001; Eijkel et al., 2005; Yiotis et al., 2003, 2012b). Still, a systematic study of the liquid films including the visualizations, mechanisms and influences on evaporation is missing in literatures. Another improper consideration in many models is the oversimplified flat evaporation/drying front (Shahraeeni et al., 2012; Geistlinger & Leuther, 2018; Or & Lehmann, 2019; Yiotis et al, 2012b; Balugani et al., 2018; Lehmann et al., 2018; Wang et al., 2019), as the evaporation/drying front is only relatively flat when the pore size distribution is very narrow (Lehmann et al., 2008), oftentimes, the actual evaporation plane is rather fractal and possesses a larger cross-sectional interface for vapor diffusion than the approximated flat front.

Direct visualization and monitoring of evaporation from porous media is an optimal method to explain those dynamical uncertainties, which are not easy to achieve in the field studies, but applicable by a lab setup. Compared to the filed, the most limited laboratory atmospheric condition is the air velocity. However, studies have shown that, the sole role of air velocity is to define the boundary layer thickness across which vapors diffusion occurs and can be quantified (Shahraeeni et al., 2012; Geistlinger & Leuther, 2018). Many studies applied packed glass beads as representative of real soil for the

experimental study (Shaw, 1987; Laurindo & Prat, 1998; Yiotis et al., 2012b), which give good contrast between the different phases regions (e.g. the dry region, film region and saturated region), but it is not ideal to display the multiphase flow dynamics at the interface and at pore scale, especially difficult for the visualizations of liquid films. For the purpose of in-depth dynamics study, an alternative visualization method is needed.

In short, there are still several main problems in the current evaporation studies:

1. Difficulties in separating the component of evaporation (E) from the total evapotranspiration (ET) for certain soil types.
2. Problematic application of the semi-empirical or empirical models in regions where soil structure is known but climate data are limited.
3. Uncertainties of other parameters in the applied water balance equation (precipitation = ET + runoff + soil moisture change) may cause errors in the ET estimation.
4. Which role does the viscous boundary layer thickness (air velocity dependent) play?
5. Do the soil hydraulic properties (e.g. pore size distribution, retention curve) play an essential role in evaporation?
6. Is the capillary flow through pore ducts the only dominant flow for evaporation process as described in many models?
7. What is a good alternative medium as representative of soil to display the multiphase flow dynamics at pore scale apart from the packed glass beads?
8. Why are the angularity of the pore space and inner surface roughness so important for evaporation?
9. Is the approximated flat evaporation front realistic for estimating evaporation?

My thesis will make new contributions to the above listed issues 1 and 3 by proposing a physical evaporation model based on the essential evaporation mechanisms, and give answers for the problems 6, 7, 8 and 9 with in-depth explanations.

Suzuki and Maeda (1968) developed a two dimensional model of evaporation, which describes the mass transfer from discontinuous but interacting menisci of water-filled pores to the ambient air. It has been shown that, for the sufficiently thick boundary layer (low atmospheric demand), a partially dry medium surface may sustain a constant evaporation rate. Shahraeeni et al. (2012) extended the Suzuki and Maeda theory and developed the "isolated pore evaporation model" (IPE model), which maps the porous medium as an interacting network. The IPE model regards the vaporization surface consisting of numerous spatially isolated but hydraulically connected pores, evaporation contributions from different pore classes are summed up. Once evaporation starts, the curvature radius of meniscus decreases monotonically with increasing mass loss till equal to the pore radius r. The pore with largest radius and least capillary resistance is invaded first, and consequently becomes "***inactive***" as the pore surface is no longer wet. The gradient of capillary pressure ($P_c \propto \frac{1}{r}$) caused by different pore sizes drives water transporting from large pores to small pores (denoted as the capillary pumping), which maintains the small pores to be water filled and "***active***" for evaporation (Fig.1.2). The term "inactive" implies that vapor diffusion from receding menisci (dashed red arrow in Fig. 1.2) can be neglected, vapor flux from pores at the surface is dominant.

Figure 1.2 gives an example of evaporation process by IPE model (Geistlinger & Leuther, 2018). The capillaries cover a pore size distribution (PSD) of Δr and are hydraulically connected. Due to the capillary pumping, drying front in the large pore (inactive pore) is receding into the medium with an increasing front depth L_c. Water flux q_w in the active pore supplies for evaporation, that, vapor diffuses from the active pore meniscus into air across the boundary layer thickness δ (red arrow in Fig.1.2). If the viscous forces is ignored, when L_c reaches the maximum extension given by the gravitational length $L_G = \Delta h_c \propto (\frac{1}{r_1} - \frac{1}{r_2})$, where Δh_c is the capillary height difference, meniscus in the small capillary will detach from the open surface as the end of stage-1 ($t = t_c$).

The reduce of surface water content during evaporation causes an increase of the dry regions or spacing between the remaining active pores. The IPE model shows, when the remaining active pores become gradually isolated, the corresponding vapor concentration fields become increasingly three-dimensional, which enhances the evaporative flux from each pore. For low atmospheric demand, such enhancement effect may fully compensate for the reduced active evaporative pores and on average maintains a constant evaporation rate for the entire porous medium (Shahraeeni et al. 2012).

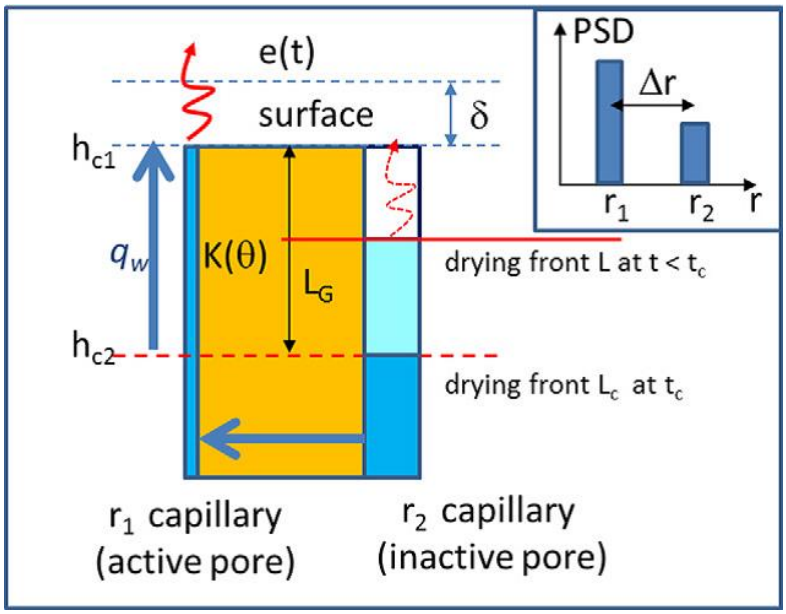

Figure 1. 2 Capillary pumping from an inactive pore with radius r_2 to an active pore with radius r_1. Drying front depths are L and L_c at corresponding times t and t_c. The e(t) is evaporation rate, δ is the viscous boundary layer thickness, h_{c1} and h_{c2} are capillary heights, $L_G = h_{c1} - h_{c2}$ is the gravitational length, and PSD denotes the pore-size distribution (Geistlinger & Leuther, 2018).

Based on the IPE model with a discrete PSD, Geistlinger and Leuther (2018) developed a continuous IPE model which approximates the integration over PSD as a sum using an analytical integral formulation. The porous medium consists of N_{uc} unit cells of length L_{uc}, each unit cell contains a wet square pore of equivalent radius r_i and a dry area surrounding the wet pore (Fig. 1.3). A critical radius r_c divides the PSD into active and inactive pores. With the decreasing of active pores during evaporation, r_c is shifting towards smaller values. The model couples the REV scale and the pore scale by analytical integration over the surface fluxes from active pores with the upper integration limit r_c and lower integration limit r_{min}, r_{min} (about 30 μm) defines below which pore size the viscous and gravitational forces become comparable with capillary forces, thus the IPE model is not applicable.

Geistlinger and Leuther (2018) applied the continuous IPE model to sandy soil and loamy sand drying experiments, the model suitably describes the characteristic stage-1 behavior for both soils in the case of low atmospheric demand. In general, the IPE model well captures the correct stage-1 dynamics because the model realistically maps the porous media as a network with the interacting between different pore classes. While, as a big drawback, the model doesn't consider a realistic picture within the capillary, that water transport through the liquid films in corners and surface cavities is ignored.

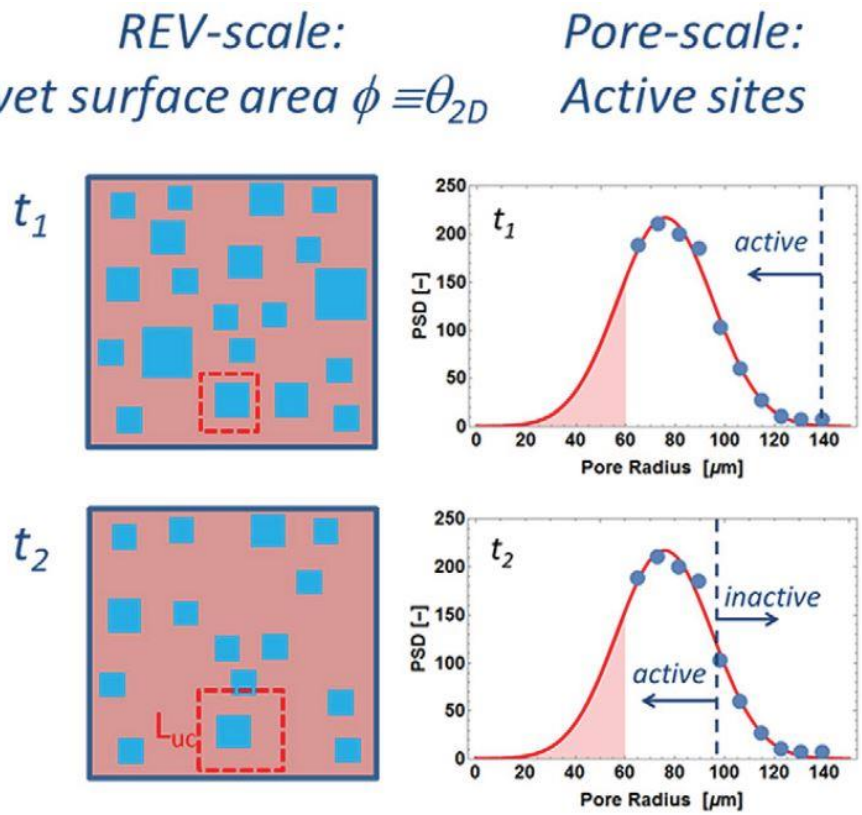

Figure 1. 3 Conceptual IPE model that couples REV scale and pore scale at different times ($t_1 < t_2$). The water-filled active pores are shown by blue squares and the unit cell L_{uc} is indicated by the red dashed square. The blue dashed lines indicate the critical radius r_c that separates the PSD into active and inactive pores (Geistlinger & Leuther, 2018).

Different types of capillary flows can occur depending on the morphology of the pore space, the geometric and physico-chemical properties of the pore-solid interface. For angular pores, the geometrical structure of sharp corners enables the existence of capillary flow along the corners, denoted as the corner flow (CF; Blunt & Scher, 1995; see red arrows in Figs. 1.4a and 1.4b), which has smaller curvature radius and higher capillary pressure than the bulk flow in the pore ducts. For porous media with rough inner surface, another type of capillary flow occurs inside the surface cavities. This capillary flow is driven by the high capillary pressure in the tiny cavities and generally carpets the entire rough surface, it is denoted as thick-film flow (TFF; Geistlinger et al., 2016; see the light blue section in Fig. 1.4b with flow direction showed by yellow arrow). I emphasize my study is in pore scale (microns), the pore diameters of the applied porous media (2D micromodel) are mainly in the range between 200 to 600 μm and the surface roughness of the applied glass-ceramic micromodel is within several microns (1~10 μm). Besides, there

can be an ultra-thin film flow on surfaces which has different physico-chemical reason: the nanoscale ultra-thin film flow is based on solid-liquid intermolecular adsorption due to the chemical surface properties, flow in this film is driven by the disjoining pressure (de Gennes, 1985; Hu et al., 2020). In my study I focus on the corner flow and thick-film flow which are determined by the geometric properties of the pore space and pore-solid interface, denoted as the *geometric* capillary flows.

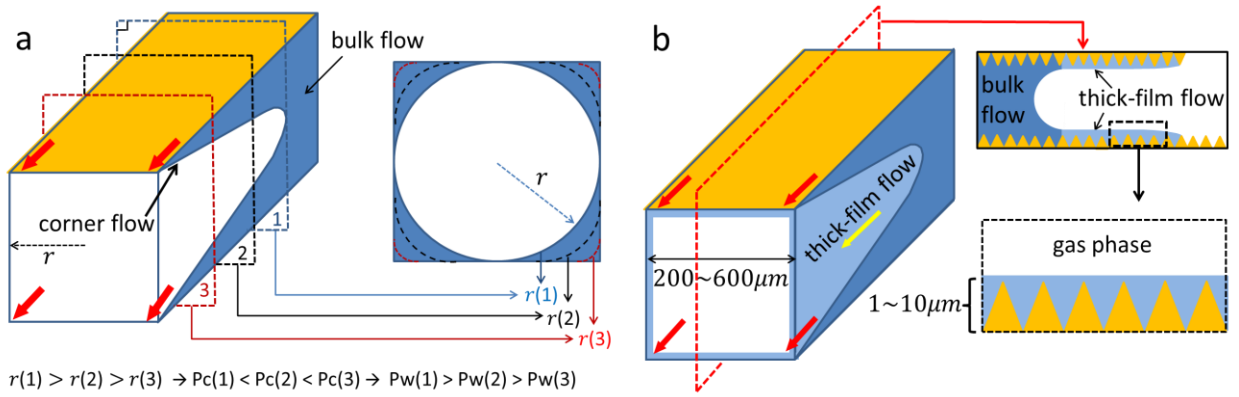

Figure 1. 4 Schematic models showing capillary flow during evaporation, where the water phase is shown in blue, and corner flow is indicated by red arrows: (a) Smooth surface capillary with corner and bulk flows; the water-gas interfaces at positions 1, 2, and 3 are indicated by the blue solid, black dashed, and red dashed lines, respectively, in the cross-sectional image. Capillary pressure P_c increases and water pressure P_w decreases along the corner flow direction due to the decreasing curvature radius r. (b) Rough surface capillary with bulk, corner, and thick-film flows; the thick-film flow is shown in light blue with its flow direction indicated by a yellow arrow. The cross-sectional image of the red dashed rectangle shows the thick-film flow filling the surface cavities and carpeting the entire rough surface (Fig. 1; Ding & Geistlinger, 2021).

The hierarchy of the three capillary flows is determined by the driving water pressure P_w, which is given by the negative capillary pressure P_c (at steady state, $P_c = P_g - P_w$, the gas phase pressure $P_g \cong 0$). According to the Young-Laplace law, $P_c \propto \frac{1}{r}$, because the curvature radii of the three different flows obey the following relationship: $r_{BF} > r_{CF} > r_{TFF}$, the water pressure gradient shows a tendency: $P_{w,BF} > P_{w,CF} > P_{w,TFF}$, water transports from the bulk flow towards the corner flow and thick-film flow. Even though the meniscus of bulk flow is receding during evaporation, with the liquid delivery by corner flow and thick-film flow, the open surface is kept partially wet for a certain time. Due to the lack of considering corner/thick-film flow, the IPE model has a modeled evaporation front at the bulk flow

meniscus, while practically vapor diffusion occurs intensively near the corner/thick-film flow front tips, where the vapor concentration undergoes s sharp decline.

Eijkel et al. (2005) proved the dominance of corner flow by conducting both theoretical modeling and experiments of evaporation from an array of parallel noncylindrical micromachined Pyrex nanochannels. The nanochannels have wedge-shaped corners and high aspect ratio (width >> height of the cross-sectional surface), the identical height of all the channels is 72 nm while the widths vary from 2 to 30 μm. Three evaporation mechanisms were considered, corner flow, film flow and vapor diffusion. Evaporation caused by film flow and vapor diffusion doesn't depend on the channel width, while evaporation due to corner flow is influenced by the width, because the number of corners is identical in each nanochannel but the total water volume is proportional to the width. The narrow channels dried faster than wide channels and the observed evaporation rates were linearly related to the inverse channel width (1/width), which indicates the dominance of corner flow. The observed evaporation rates were enhanced by a factor of 50–500 relative to the theoretical rate by vapor diffusion only. Although relative humidity (RH) can largely affect the efficiency of vapor diffusion, Eijkel et al. (2005) theoretically and experimentally evidenced that the evaporation rate is independent of RH (up to RH=93%), because corner flow is dominant over vapor diffusion.

Yiotis et al. (2012) developed an evaporation model incorporating the effects of corner flow. They obtained analytical expressions for all relevant variables, such as the evaporation rates, film region extension and the critical saturation that marks the transition from the constant to the falling rate periods. The model considers a pore throat or pore body as an effective capillary with a rectangular geometry and defined by the mean pore size d_0, thus named as the single square capillary model (SSC-model). Corner flow is geometrically parametrized by the curvature radius of the corner flow menisci $r(x, y)$ (Fig. 1.5). The curvature along x direction can be neglected compared to the curvature in y direction (rectangular to the x direction). The change of r_y leads to a water pressure gradient, which drives the water transport from bulk flow towards open surface through corner flow.

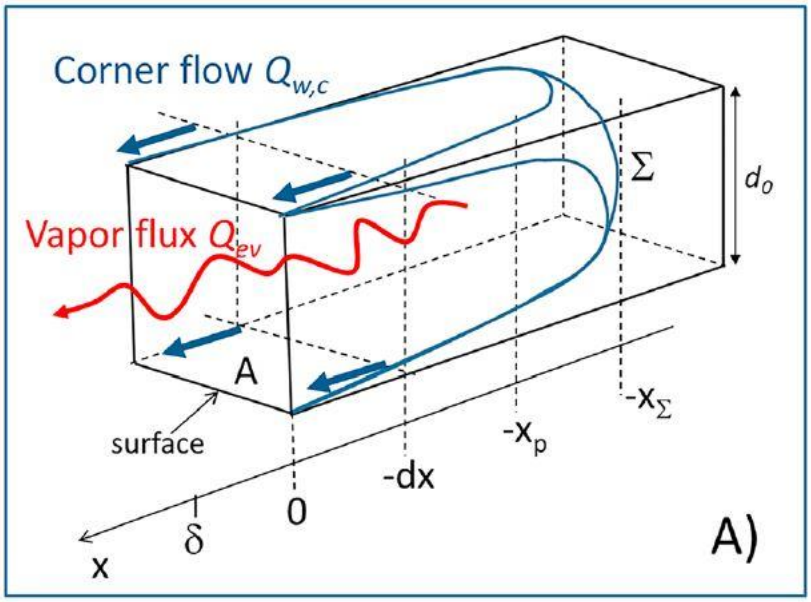

Figure 1. 5 Conceptual evaporation model of a square capillary (width d_0). Shown is the end of stage-1, at which the corner flow tips detach from the open surface. The notations: corner flow flux Q_{wc}, water vapor flux Q_{ev} (evaporation rate, red arrow), water meniscus Σ at $-x_\Sigma$, mean percolation front at $-x_p$, open surface at x = 0, viscous boundary layer thickness δ (Geistlinger et al., 2019).

As long as corner flow reaches the open surface, the wicking action keeps the surface at least partially wet, and a constant drying rate is maintained (stage-1). At a certain length, corner flow cannot sustain over the increasingly large lengths and detach from the open surface, a completely dry region develops between the corner flow front and open surface, symbolizing the onset of stage 2. Later on, three regions are formed based on the wetting condition. Below the dry region is the film region where pores are partially wet by corner flow, and beneath is the liquid saturated region (Fig. 1.6). Practically, evaporation occurs intensively near the corner flow front tips, as vapor diffusion is suppressed by the saturated vapor concentration along the whole liquid-gas interface in the film region. Therefore, corner flow is the dominant mass transport mechanism within the film region and mass transport by diffusion is only in the dry region. Under the quasi-steady-state assumption, the corner flow flux Q_{wc} transported to the mean evaporation front is equal to the vapor flux Q_{ev} (evaporation rate, red arrow in Fig. 1.5) across the mean evaporation front.

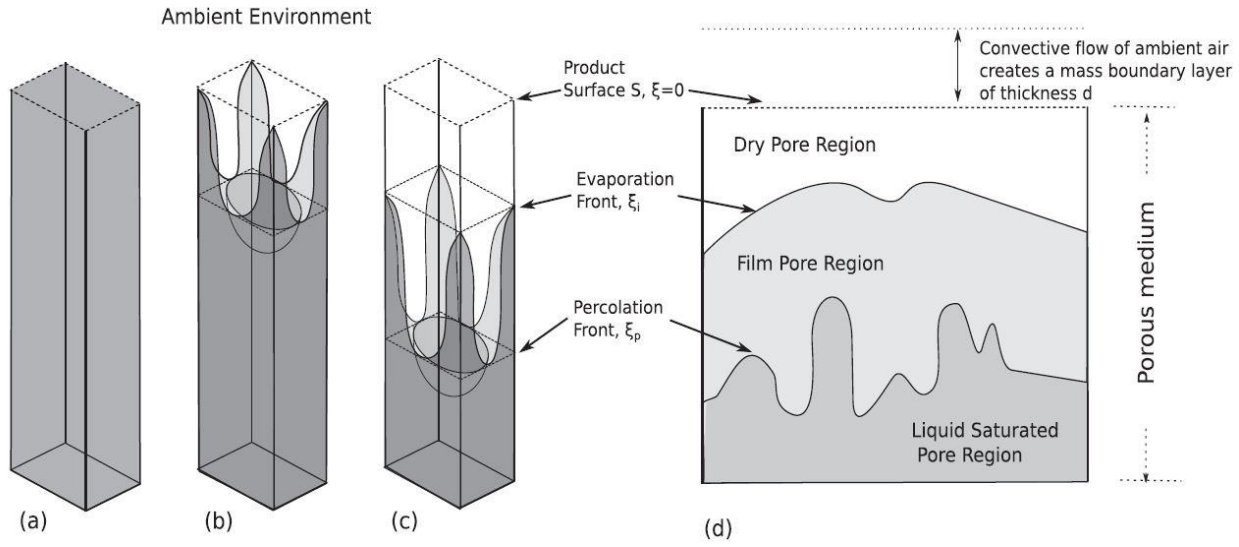

Figure 1. 6 Schematics of a square capillary during evaporation (a-c). (a) The capillary is initially saturated. (b) As liquid evaporates, the bulk flow meniscus recedes into capillary while four paths of corner flow are developed, the corner flows expand till the open surface which still maintains a constant evaporation rate. (c) After the bulk flow meniscus recedes deeper in the capillary, corner flows detach from the open surface and a dry region is developed. (d) The porous medium is then separated into three regions, the liquid saturated region and film region are divided by the percolation front, the dry region and film region are divide by the evaporation front (Yiotis et al., 2012).

Yiotis et al. (2012b) tested their model by a series of isothermal drying experiments in packed glass beads saturated with volatile hydrocarbons. The experimental image shows a region with completely dry glass beads (the dry region). Then a brighter region where the gas phase has invaded the central part of the pores, while a continuous liquid film covers the beads (the film region). Lastly, there exists a darker-color region of beads corresponding to the liquid-saturated region. The evaporation front appears to be flat and recedes quite smoothly in the medium while the percolation front is more fractal and moves in the manner of Haines jump. The SSC model results show a good agreement with the experimental data. Due to the suppressing effect of gravitational force (Bond number $B_0 < 0$), larger bead packings display shorter duration of stage-1 and shorter film zone extension. Besides, a linear dependence of the evaporation rate with the position of the film tips x_i is achieved, which supports the argument that practically evaporation occurs near the film zone tips. The experimental images show the phase patterns of different zones but no visualization of corner flow was displayed.

The SSC model describes the realistic dynamics within a single capillary, considering the dominance of corner flow in film zone. While in REV-scale or larger scale, this model maps the porous medium into non-interacted isolated pores, which is unrealistic for natural soil system. Besides, the model doesn't take into account the factor of contact angle, instead, they introduced a "roundness factor" into the model, which can weaken the capillary pressure in corners with similar influence of contact angle. They artificially adjusted the roundness factor and found the best agreement between modeling and experiments, but the accuracy of the roundness factor cannot be experimentally proved.

Geistlinger et al. (2019) extended the SSC model as a function of contact angle θ and temperature, and tested the model with water evaporation experiments from a 2D silicon micromodel (named MM5-Si). The micromodel MM5-Si is designed with lognormal-distributed "ideal" square channels, and fabricated by the inductively coupled plasma-deep reactive ion etching (ICP-DRIE) technology (Küchler et al., 2003; Chomsurin & Werth, 2003; Willingham, et al., 2008; Zuo et al., 2013), which reduces the corner rounding effects to the largest extent and results in high edge steepness, absolute smoothness and a true mapping of the lattice structure. The contact angle dependence on evaporation process is derived by inverse modeling. As a result, the derived contact angle of water on the SiO_2 surface 38° ± 1° is very close to the measured contact angle 42° ± 2°. In my work, I further tested the SSC model with regular (quadratic lattice) and irregular (soil structure) pore structures, for the evaporations of water and ethanol. I expected the SSC model can appropriately describe evaporation process from capillary with smooth surface where corner flow transport is dominant in the film zone.

The work of Eijkel et al. (2005) and Yiotis et al. (2012) theoretically and experimentally indicate the dominance of corner flow for evaporation, but they didn't present a visualization of the corner flow appearance in pore-scale. Zhao et al. (2016) conducted fluid-fluid displacement experiments with fluorescence microscopy and displayed a good visualization of corner flow during imbibition within 2D micromodels. During strong imbibition (θ = 7°), invading fluid advances by coating the perimeter of the grains via corner flow rather than filling the pore bodies (bulk flow). In intermediate imbibition (θ = 28°), co-existence of pore-body displacement and corner flow is observed. The width of corner flow in intermediate imbibition is visually smaller than that in strong imbibition. In the weak imbibition (θ = 60°), the invading fluid advances only by bulk flow, corner flow is not seen. The experimental observations can be explained by the geometric constraint for corner flow appearance: for a given interfacial curvature, the interface of corner flow is forced further into the corner when the contact angle θ increases, thereby reducing the cross-sectional area available for corner flow. To enables the appearance of corner flow, the contact angle must satisfy the geometric relation $\theta < (\pi - \alpha)/2$, where α is the corner angle.

Due to the angular geometry and rough surface of the real soil and sand grains, corner flow and thick-film simultaneously coexist in the natural porous media. To my best knowledge, there is no literature showing visualizations of corner flow and thick-film flow during evaporation. Therefore, the first goal of my study is to give good visualizations of corner and thick-film flow, and present the water transport between different capillary flows during evaporation in 2D micromodels.

Lenormand and Zarcone (1984) demonstrated the importance of thick-film flow and that the time scale determines the relevant flow type during displacement. A capillary number $Ca = \frac{\mu_w u_w}{\sigma_{gw}}$ (Blunt & Scher, 1995) was measured to present the relative effect of viscous forces versus capillary forces (μ_w - dynamic viscosity of water, σ_{gw} - water surface tension, u_w - the receding velocity of percolation front). At a high flow rate (capillary number: $Ca > 10^{-5}$), the wetting fluid only exists in the duct (bulk flow BF). At low capillary numbers ($Ca = 10^{-6}$), corner flow (CF) and thick-film flow (TFF) occur with the same order of magnitude; for low flow rates ($Ca < 10^{-6}$), TFF is the most significant water transport mechanism, facilitating the movement of wetting fluid throughout the network by flowing over the surface roughness, as the roughness term leads to a decrease in free energy (Zulfiqar et al., 2020). In my study, as the equivalent capillary numbers were in the range of 10^{-8} to 10^{-7} (u_w was derived by the experimental evaporation flux Q_{ev} over cross sectional area *A*), I expect the TFF to be an *effective water transport mechanism* in the evaporation process.

Most literatures address their focus on corner flow enhancement for evaporation, only few studies mentioned the influence of thick-film flow. Dullien et al. (1989) visualized the residual wetting fluid filling the cavities of the rough surface of etched beads using scanning electron microscopy (SEM) and microscopy. At the end of their drainage experiment, the etched beads' surfaces appeared like they have been treated with several paint coats compared to the surface of unused etched beads. The bead surface cavities were filled with wetting fluid, forming a hydraulically conductive continuum of microchannels (TFF). Laurindo and Prat (1998) compared the drying curves for smooth and etched rough bead packs, finding that the etched beads' drying rate was enhanced more by TFF than pure vapor diffusion in the smooth beads. Eijkel et al. (2005) expected the drying rate to be increased by the combination of TFF and vapor diffusion relative to vapor diffusion alone.

As few studies have investigated the impact of thick-film flow on the evaporation process, we conducted evaporation experiments with 2D micromodels of different materials (silicon vs. glass-ceramics). The silicon micromodels have a smooth inner surface where no TFF occurs, while the glass-ceramic micromodels contain a rough inner surface where TFF exists. As thick-film flow has a lower water phase

pressure than corner flow ($r_{CF} > r_{TFF}$), I expect that TFF will lead to a longer extension than CF. The longer film extension can maintain the medium surface partially wet for a longer period with a constant rate (stage 1). Additionally, I expect that, in stage 2, evaporation from the glass-ceramic micromodels will be more enhanced by TFF than that of the silicon micromodels.

The pore system of fine-textured soils is organized hierarchically, with the micropores (smaller than 0.08 mm) between the textural grains within aggregates and the macropores (larger than 0.08mm) between aggregates. The micropores retain water and agrochemicals and are responsible for capillary water distribution. The macropores promote aeration, gas exchange, free water flow (which can transport dissolved nutrients and agrochemicals) and evaporation in the soil profile (Easton and Bock, 2016). Witkowska-Walczak (2000) investigated the impact of aggregate size on evaporation rate with two soil samples, the Eutric Cambisol derived from clay silt (loess) and Gleyic Phaeozem derived from loam silt. After sieving each soil sample into six aggregate size classes (from <0.25 mm up to 5-10 mm), soil columns were filled with different aggregate size distribution. In both low and high evaporativity cases, the evaporation rates decrease successively with the increase of the fraction of large aggregates in the soil columns, and the corresponding water diffusivity decreases rapidly with the increase of aggregates size (up till the maximum size class is 1-3 mm). The decrease of capillary rise in the large aggregates causes the decline of diffusivity and leads to lower hydraulic conductivity in the upper layer of columns, this factor is so significant that cannot be compensated by the effective surface of big pores.

Advanced imaging techniques, such as Focused Ion Beam Scanning Electron Microscopy (FIB-SEM) and X-ray microcomputed tomography (micro-CT), have been applied quite often in porous media research to obtain 2D or 3D high resolution static images. However, the long scanning time (on the order of minutes or even hours) makes it difficult to capture the real-time dynamics of flow (Anbari et al., 2018). As alternative method, micromodel is a transparent interconnected porous network considered as presentative for pore system of soil, it enables the direct visualization of the complex fluid structure and flow dynamics in pore scale which cannot be directly achieved by soil samples. In this study, micromodels of two pore structures were applied, an irregular pore structure named as MM4 and a regular pore structure named as MM5. MM5 is a quadratic lattice pore network with porosity of 0.52 and pore sizes between 0.2 to 0.6 mm (lognormal distributed width $d_{mean} = 400 \pm 62\ \mu m$), the grain particles have relatively homogeneous size in the class of 0.5-1 mm (equivalent circle diameter), which is a good representative model for coarse sand (Udden, 1914; Wentworth, 1922). MM4 has a porosity of 0.42 and pore sizes ranging from 0.006 to 1.2 mm (lognormal distributed mean radius $r_{mean} = 205 \pm 53 \mu m$). MM4 has relatively heterogeneous grain size distribution (Table 1.1), mostly between 0.5 to 2 mm, but still some

small grains exhibiting with minimum size of 0.1 mm. Therefore, MM4 can be a representative model for the coarse to very coarse sand (Udden, 1914; Wentworth, 1922).

Table 1. 1 The grain size distribution of MM4 pore structure.

Grain diameter (mm)	<0.25	0.25-0.5	0.5-1	1-2
Fraction (%)	0.287	2.742	67.915	29.055

In summary, the main objectives of this study are summarized as follows:

1. I applied 2D micromodels with different manufacture materials and pore structures, for evaporations at different temperatures, to present the complex interaction of different capillary flows on evaporation process and give answers for the previously listed problems 6, 7 and 8. I expect that the micromodels with rough surface will lead to enhanced evaporation than the micromodel with smooth surface. I also expect that the irregular structure micromodel will have stronger corner flow transport and lead to higher evaporation efficiency than the regular structure micromodel.
2. I applied DSLR camera and fluorescence microscopy for the 2D micromodel experiments, to give good visualizations of corner flow, thick-film flow, and the liquid transport between the different capillary flows during evaporation.
3. I will test the SSC model with water and ethanol, I expect the SSC model can appropriately describe evaporation process from an ideal square capillary with smooth surface where corner flow transport is dominant in the film zone. Therefore, offering new contributions for the previously listed issues 1 and 3.
4. I give answer for the listed problem 9 and present the fractality of the evaporation front must be taken into account.
5. Based on the results of the study of evaporation, I aim to give insights for soil treatments with the purpose of reducing soil water evaporation.

2 Theory

2.1 Physics of the Evaporation Process: IPE model

2.1.1 Surface Tension and Capillary Pressure

Below water surface, water molecule has attractions in all directions, while at water surface, the water molecules have no neighboring molecules above, and consequently exhibit attraction forces inward (Fig 2.1). A molecule bonded with neighbors is in a lower energy state than if it's alone, which makes the energy state of interior molecules lower than the surface molecules. Water droplet tends to minimize its energy, as a result, surface water molecules try to maintain a minimum surface area (spherical surface) and allow more molecules to have a lower energy state. This physical property is referred as surface tension σ, which describes the amount of surface potential increased when a unit surface area is expanded.

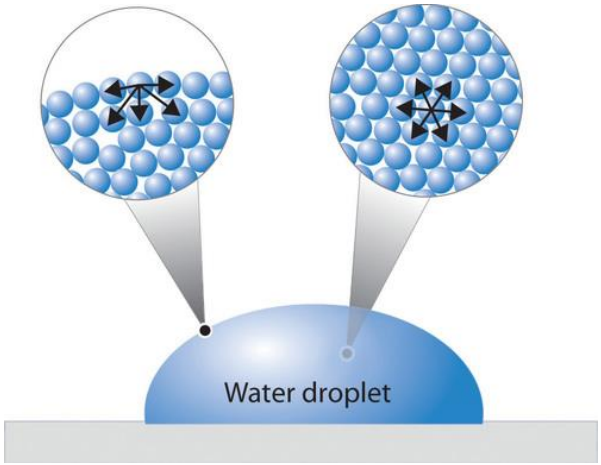

Figure 2. 1 Molecule bindings at the water surface and in the interior.

Besides the intermolecular cohesive force holding the water molecules together with minimum surface area, there is also an adhesive force between water molecules and other type molecules (e.g. glass wall molecules), it is the interfacial tension trying to make the water droplet spreading out. If the adhesive force is stronger than the intermolecular cohesive force, water rises up through matrix walls which referred as capillary action with capillary force F_c (Fig. 2.2). The water phase shows a concave meniscus with contact angle θ below 90°, in this case we define the wettability of the solid material as hydrophilic. If the contact angle θ is 0, the solid surface has completely wetting behavior, water spreads over the whole surface and forms a water film, otherwise, the solid surface is partial wetting with θ between 0° and 90°. If the water-matrix adhesive force is not as strong as the water intermolecular cohesive force,

water table at matrix walls moves downwards and the water interface shows a convex with θ above 90°, the solid surface is considered as hydrophobic.

The interactions of the cohesive and adhesive forces result the capillary pressure P_c in a thin tube, which is described by the Young-Laplace equation,

$$P_c = \sigma_{gw} \cdot H(r_1, r_2) = \sigma_{gw}\left(\frac{1}{r_1} + \frac{1}{r_2}\right) \qquad \text{Eq.2.1. 1}$$

where σ_{gw} [N/m] is the interfacial tension of the gas-water interface. P_c is dependent on the meniscus shape formed by the mean curvature $H(r_1, r_2)$ (Fig. 2.2), where r_1 and r_2 are the principal radii of curvature.

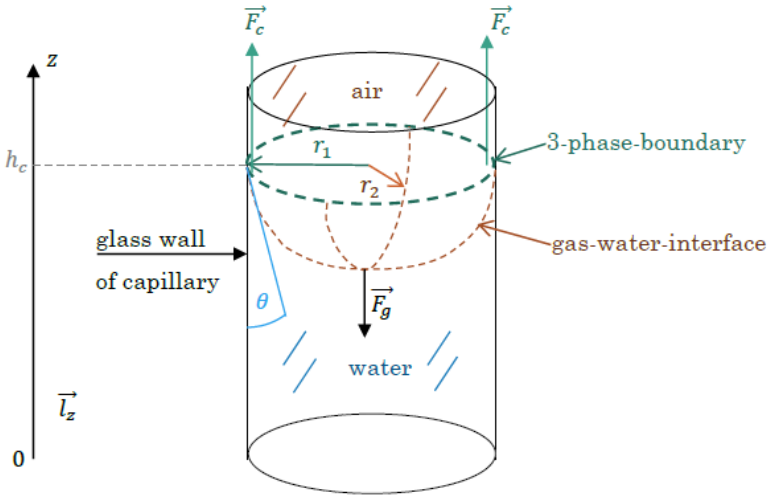

Figure 2. 2 Young-Laplace law derivation in a capillary tube with three-phase boundary and gas-water interface (Vogel, 2017).

2.1.2 Capillary Pumping and IPE model

When the water-gas interface forms a meniscus with curvature radius of R_H, the capillary pressure P_c can be represented by half of the pore width a and contact angle θ

$$P_c = \frac{2\sigma_{gw}}{R_H} = \frac{2\sigma_{gw}\cos\theta}{a}. \quad \text{Eq.2.1. 2}$$

In order to maintain a hydrostatic equilibrium, the capillary pressure is balanced by the hydrostatic pressure P_h

$$P_h = \rho_w g h_c = P_c, \quad \text{Eq.2.1. 3}$$

where ρ_w is water density, g is the gravitational acceleration and h_c is the height of capillary rise ($h_c > 0$ when $0 \leq \theta < 90°$, and $h_c \leq 0$ when $90° \leq \theta < 180°$). The capillary height h_c is given by

$$h_c = \frac{2\sigma_{gw}\cos\theta}{\rho_w g a}. \quad \text{Eq.2.1. 4}$$

Equilibrium between capillary pressure P_c, water phase pressure P_w and gas phase pressure P_g is established at the water-gas interface in steady-state:

$$P_c + P_w = P_g \cong 0, \quad \text{Eq.2.1. 5}$$

which yields

$$P_w = -P_c = -\frac{2\sigma_{gw}\cos\theta}{a}. \quad \text{Eq.2.1. 6}$$

Due to the P_w gradient, water moves from larger capillary to smaller capillary dark (blue arrows in Fig. 2.3, $a_3 > a_2 > a_1$), this water transport mechanism in porous media is defined as the ***capillary pumping***.

The IPE model is based on the capillary pumping mechanism, that the pore with largest radius and least capillary resistance is invaded first, and consequently becomes "inactive" as the pore surface is no longer wet (capillary 3 in Fig. 2.3). Meanwhile, capillary pumping maintains the smaller pores to be water filled and "active" for evaporation (capillaries 1 and 2 in Fig. 2.3). Figure 2.3 gives an illustration of capillary pumping, that the pore radii of the three capillaries show the gradient $a_3 > a_2 > a_1$, water moves from capillary 3 to capillaries 2 and 1. The gas-water interface conducts a spherical change during evaporation with increasing curvature. When the maximum curvature (hemisphere) is reached in a capillary, the corresponding pore radius (defined as the critical radius r_c; see a_2 in Fig. 2.3) divides the porous media

into active and inactive pores. With the decreasing number of active pores during evaporation, r_c is shifting towards lower values.

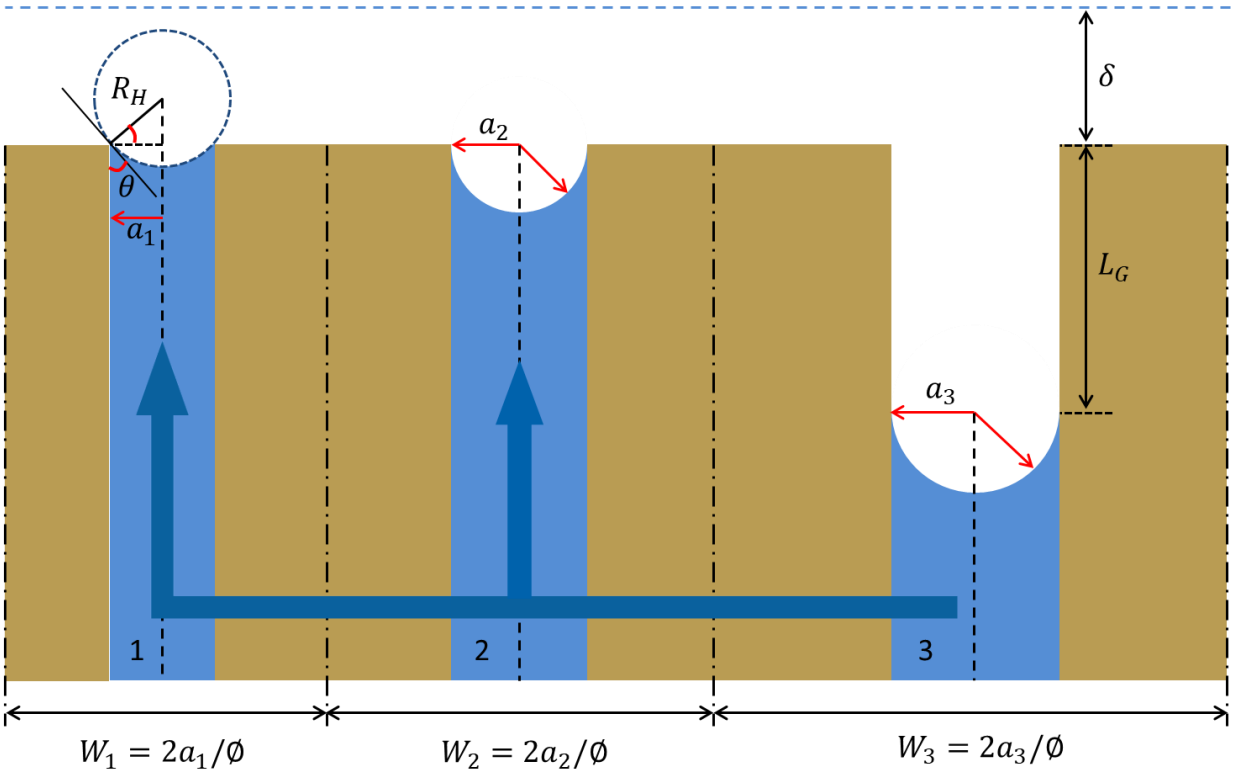

Figure 2. 3 Illustration of capillary pumping in the IPE model. Air invasion occurs to capillary 2 at the moment with the critical radius $r_c = a_2$, capillary 1 is active and capillary 3 is inactive with the meniscus receding down by L_G. Water moves from capillary 3 to capillaries 1 and 2. Capillaries 2 and 3 have the curvature radii equal to the pore radii a_2 and a_3, respectively, capillary 1 has the curvature radius of $R_H = a_2$. Vapor concentration drops from the saturated concentration C_s at menisci to the ambient concentration C_a at boundary layer thickness δ (modified Fig.5 of Shahraeeni et al. 2012)

The capillary height difference Δh_c between capillaries 2 and 3 equals to the meniscus receding distance L_G in capillary 3,

$$\Delta h_c = L_G = \frac{2\sigma_{gw}}{\rho_w g}\left(\frac{1}{a_2} - \frac{1}{a_3}\right). \qquad \text{Eq.2.1. 7}$$

Due to the restriction of $\frac{1}{a_2} - \frac{1}{a_3}$, L_G is the maximum rise in capillary 2 caused by the capillary pumping from capillary 3, afterwards, water meniscus in capillary 2 detaches from the open surface.

The IPE model assumes a porous medium consisting of number N_{uc} unit cells of length L_{uc}, each unit cell contains a ***wet square pore*** of equivalent radius r_i and a dry area surrounding the wet pore (Fig. 1.3). All unit cells are assumed to have the same surface water content θ_{2D} (initially equals to the 2D porosity ϕ; Fig. 2.3)

$$\phi = \theta_{2D} = \frac{(2r_i)^2}{{L_{uc}}^2}, \qquad \text{Eq.2.1. 8}$$

which subsequently reduces with time due to the increasing inactive pore sites.

For the porous media covering a PSD from the low pore size limit r_1 to the high limit r_2, the total mass loss m_{tot} at a certain time *t* geometrically comes from two contributions: the cap contribution from active pores, and the tube contribution from inactive pores (depending on the capillary height difference during a time step $\Delta t = t_2 - t_1$). The cap volume of a pore of radius *r* can be calculated by the curvature with the critical radius r_c:

$$V_{cap}(r, r_c) = \frac{\pi}{3} r_c^3 [2 - 3\,cos\,\alpha\,(r, r_c) + cos^3\alpha(r, r_c)], \qquad \text{Eq.2.1. 9a}$$

where the angle $\alpha(r, r_c)$ is given by

$$\alpha(r, r_c) = arcsin\frac{r}{r_c}. \qquad \text{Eq.2.1.9b}$$

The tube volume of a pore of radius *r* can be derived by:

$$V_{tube}(r, r_c) = \frac{2\sigma_{gw}}{\rho_w g}\left(\frac{1}{r_c} - \frac{1}{r}\right)(2r)^2. \qquad \text{Eq.2.1. 10}$$

The total evaporation mass loss m_{tot} is represented by (Geistlinger & Leuther, 2018)

$$\frac{m_{tot}}{\rho_w} = \int_{r_1}^{r_c} drPSD(r)\, V_{cap}(r, r_c) + \int_{r_c}^{r_2} drPSD(r)\, V_{tube}(r, r_c). \qquad \text{Eq.2.1. 11}$$

Note that, the lower integration limit r_1(about 30 μm) is not the real smallest pore radius, but defines below which pore size the viscous and gravitational forces become comparable with capillary forces, thus the IPE model is not applicable.

The term inactive implies that vapor diffusion from receding menisci (capillary 3 in Fig. 2.3) can be neglected, vapor flux from pores at the surface is dominant. The evaporation rate $e(t)$ is given by

$$e(t) = k_{REV}(C_s - C_a), \qquad \text{Eq.2.1. 12}$$

with the saturated vapor concentration C_s, the ambient vapor concentration C_a, and the ensemble average of the rate constant for REV scale k_{REV} (m/s) calculated by

$$k_{REV} = \int_{r_1}^{r_c} drPSD(r)k(r), \quad \text{Eq.2.1. 13}$$

where $k(r)$ denotes the rate constant of a certain active pore with radius r.

For pure diffusive evaporation (no convective surface fluxes), $k(r) = k_{diff}$ can be solved by the partial differential equation (Geistlinger & Leuther, 2018) that couples diffusion in the y direction (direction perpendicular to the surface). With the known vapor concentration field *C(z,y)* (Shahraeeni et al., 2012), k_{diff} can be calculated as an average across the solution region:

$$k_{diff} = \frac{2}{L_{uc}C} \int_0^{\frac{L_{uc}}{2}} j_y(z,0)dz, \quad \text{Eq.2.1. 14}$$

where the diffusive flux density is

$$j_y(z,y) = -D_{diff}\frac{\partial C}{\partial y}, \quad \text{Eq.2.1. 15}$$

with the diffusion coefficient of the ambient air D_{diff} (m^2/s).

The evaporation flux at surface equals to the internal water flux driven by capillary pumping from inactive pores to active pores. Therefore, the critical radius r_c for each time step can be determined by the equality between the geometrical mass loss (Eq. 2.1.11) and the mass loss Δm_{tot} derived from evaporation rate $e(t)$ (Eq. 2.1.12):

$$\Delta m_{tot} = e(t)A_{cross}\Delta t, \quad \text{Eq.2.1. 16}$$

where A_{cross} denotes the surface pore area.

2.2 Physics of the Evaporation Process: SSC model

The IPE model well captures the correct stage 1 dynamics by mapping the porous media as a network with the interacting between different pore classes. But the model doesn't map a realistic picture within the capillary, that the water transport through liquid films in corners and surface cavities are not considered. The SSC model considers a pore throat or pore body as an effective capillary with a square cross section, whose size is defined by the mean pore width of d_0 (Fig. 2.4). The angular geometry of capillary enables the liquid flow through corners (corner flow), which has strong capillary pressure and dominates the mass transport during evaporation.

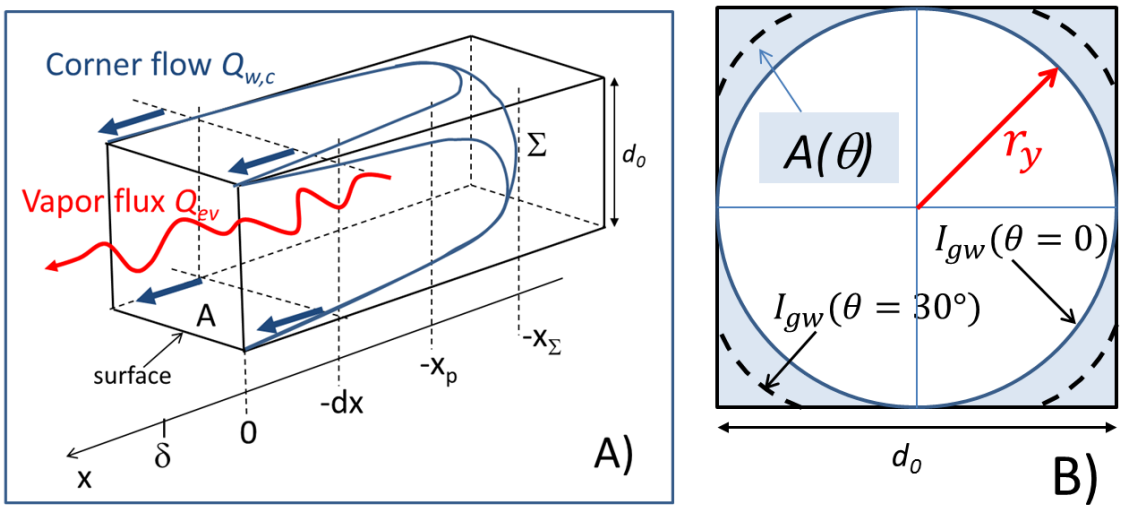

Figure 2. 4 (A) Conceptual evaporation model of a square capillary with width of d_0. Shown is the end of stage-1, when the corner flow tips detach from the open surface. The notations: corner flow flux Q_{wc}, water vapor flux Q_{ev} (evaporation rate, red arrow), water meniscus Σ at $-x_\Sigma$, mean percolation front at $-x_p$, open surface at $x = 0$, viscous boundary layer thickness δ. (B) Contact angle θ dependence of the cross section $A(\theta)$ (light blue area) and the curvature of water-gas interface I_{gw} ($\theta = 0$: blue solid line, with curvature radius of r_y; $\theta = 30°$: black dashed line; Geistlinger et al., 2019).

The 1-D analytical theory of the SSC model is based on the quasi-steady-state assumption between the evaporation flux Q_{ev} and the corner flow flux Q_{wc} (Fig. 2.4a), that the amount of water flux transported from pore ducts to the mean evaporation front through corner flow (Q_{wc}) is equal to the diffusion flux across the mean evaporation front to ambient (Q_{ev}). All the calculations below are based on one single

capillary, the MM5 and MM4 microstructures (Chapter 3.1.1) yield 79 and 91 equivalent capillaries at open surface, respectively. In stage 1, corner flow keeps the capillary open surface partially wet and maintains a constant evaporation rate. Stage 2 is initiated after corner flow detaches from the open surface (detachment time t_c). Set the open surface as zero position, the cross sectional profiles at the mean percolation front $x = -x_p$ with different contact angles are displayed in Fig 2.4b. For a certain curvature, the larger contact angle θ results a smaller cross section $A(\theta)$ available for corner flow.

The curvature of corner flow along *x*-direction can be neglected compared to the curvature in *y*-direction (perpendicular to *x*-direction; curvature radius $r_x \gg r_y$). Therefore, the capillary pressure P_c at the corner flow root $(-x_p)$ equals to the P_c at the bulk flow meniscus $(-x_\Sigma)$ because of the mutual curvature interface:

$$P_c(-x_\Sigma) = P_c\left(-x_\mathrm{p}\right) = \sigma_{gw} \cdot H\left(r_x, r_y\right) \cong \frac{\sigma_{gw}}{r_y(-x_\mathrm{p})}, \qquad \text{Eq.2.2. 1}$$

where r_x and r_y denote the curvature radii in principal directions *x* and *y*, respectively. According to Dong and Chatzis (1995), the curvature radius at corner flow root r_p is given by

$$r_y(x_1) \equiv r_p = r_0 F^{-1}(\theta), \quad (x_1 = -x_p), \qquad \text{Eq.2.2. 2a}$$

with

$$F(\theta) = \frac{\theta - \frac{\pi}{4} + cos^2\theta - sin\theta cos\theta}{cos\theta - \sqrt{\frac{\pi}{4} - \theta + sin\theta cos\theta}}, \qquad \text{Eq.2.2.2b}$$

where r_0 is half of the mean capillary width d_0. Equation 2.2.2a determines the validity range of the SSC model, that is, the following discussion considers only the range $x \geq -x_p$.

Equilibrium between the capillary pressure P_c, air pressure P_g, and water pressure P_w is established at the water-air interface in steady state: $P_c + P_w = P_g$, which yields ($P_g \cong 0$)

$$P_w = -P_c. \qquad \text{Eq.2.2. 3}$$

With the decreasing curvature radius of corner flow along positive *x* direction, the water pressure gradient drives the continuous water transport from the bulk flow towards the open surface through the four corner flow paths (Fig. 2.4a).

For the laminar flow in a cylindrical pipe, because the frictions between fluid and pipe surface hold back the fluid flowing, the flow velocity field displays a radial decrease from the circle center towards edge (pipe surface), and the volumetric flow rate Q is given by the Hagen-Poiseuille equation:

$$Q = \frac{\pi {R_0}^4}{8\mu_w L} * \Delta P_w, \quad \text{Eq.2.2. 4}$$

where R_0 is the pipe radius, L is the pipe length, μ_w is the dynamic viscosity of water and ΔP_w is the pressure difference between the two ends of pipe.

For the laminar flow along corners, the axial flow velocity can be expressed by the cylindrical coordinate system $v(r, \emptyset, x)$ (Fig. 2.5). Ransohoff and Radke (1988) gave the dimensionless form of the axial velocity of the wetting fluid u

$$u = \frac{\mu_w v}{{r_y}^2(-\frac{dP_w}{dx})}. \quad \text{Eq.2.2. 5}$$

The velocity profile $u(r, \emptyset)$ can be solved for a given corner flow geometry (r_y, θ) with an average $\langle u \rangle$. A dimensionless flow resistance β was defined by Ransohoff and Radke (1988; Fig. 2.6) as

$$\beta = \frac{1}{\langle u \rangle}. \quad \text{Eq.2.2. 6}$$

The average velocity $\langle v \rangle$ is calculated by

$$\langle v \rangle = \frac{{r_y}^2}{\mu_w \beta(\theta)}(-\frac{\partial P_w}{\partial x}), \quad \text{Eq.2.2. 7}$$

then the volumetric corner flow rate Q_{wc} is given by

$$Q_{wc} = A(\theta) * \langle v \rangle = -\frac{C^*(\theta)\, r_y^4}{\mu_w \beta(\theta)} \cdot \frac{\partial P_w}{\partial x} \quad \text{Eq.2.2. 8a}$$

with the cross section of corner flow $A(\theta) = C^*(\theta)\, r_y^2$. The θ-dependent constant C^* is given by (Dong & Chatzis, 1995)

$$C^*(\theta) = 4\frac{cos\theta cos\left(\frac{\pi}{4}+\theta\right)}{sin\left(\frac{\pi}{4}\right)} - \left(\frac{\pi}{4} - \theta\right). \quad \text{Eq.2.2.8b}$$

The $\frac{C^*(\theta)\, r_y^4}{\beta(\theta)}$ in equation 2.2.8a is considered as a corner flow geometry factor corresponding to the cylindrical flow geometry factor $\frac{\pi {R_0}^4}{8}$ in the Hagen-Poiseuille equation.

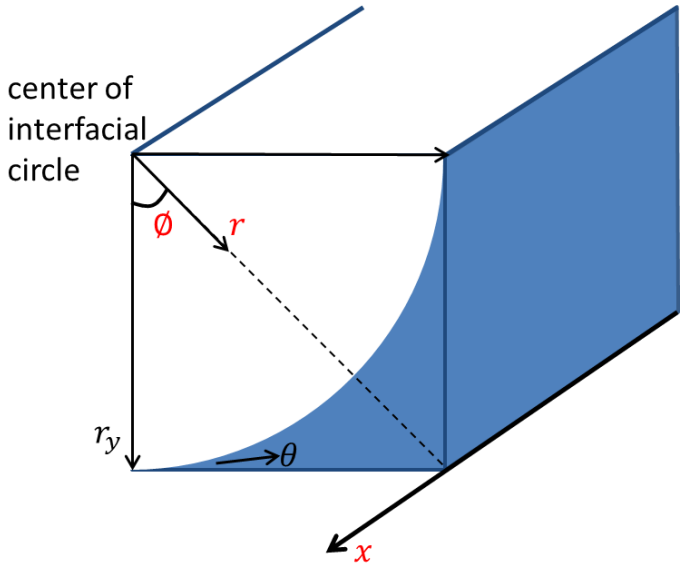

Figure 2. 5 The axial flow velocity in corner is expressed by the cylindrical coordinate system, flow is in the positive *x* direction, r_y is the curvature radius of corner flow interface in the *y* direction (perpendicular to *x*-direction) and θ is the contact angle.

Considering the hydrostatic pressure caused by gravitational force (vertical case with gravity stabilized front), the corner flow rate Q_{wc} which dominates the water mass transport within the film region is determined by:

$$Q_{wc}(x,t,\theta) = -\frac{C^*(\theta)}{\mu_w \beta(\theta)} \cdot r_y^4(x,t) \cdot \left\{\frac{\partial P_w}{\partial x} + \rho_w g\right\}. \qquad \text{Eq.2.2. 9a}$$

Replace P_w by P_c (Eq. 2.2.1; Eq.2.2.3), r_y by the normalized radius of curvature $\rho = r_y/r_p$ and $\beta(\theta)$ by the rescaled flow resistance $\alpha(\theta) = \frac{\beta(\theta)}{C^*(\theta)}$ (Fig. 2.6), respectively, Eq.2.2.9a can be reformulated as

$$Q_{wc}(x,t,\theta) = \frac{r_y^4(x,t)}{\mu_w \alpha(\theta)} \cdot \left\{\sigma_{gw} \cdot \frac{\partial}{\partial x}\left(\frac{1}{r_y}\right) - \rho_w g\right\}$$

$$= \frac{r_y^4(x,t)}{\mu_w \alpha(\theta)} \cdot \left\{\sigma_{gw} \cdot \left(-r_y^{-2}\right) \cdot \frac{\partial r_y}{\partial x} - \rho_w g\right\}$$

$$= -\frac{\sigma_{gw}}{3\mu_w \alpha(\theta)} \cdot \left\{ \frac{\partial}{\partial x}\left(r_y^3\right) + \frac{3r_y^4(x,t)\rho_w g}{\sigma_{gw}} \right\}$$

$$= -\frac{\sigma_{gw}}{3\mu_w \alpha(\theta)} \cdot \left\{ r_p^3 \cdot \frac{\partial}{\partial x}\{\rho^3(x,t)\} + r_p^3 \cdot \frac{r_p^2 \rho_w g}{\sigma_{gw}} \cdot \frac{3\rho^4}{r_p} \right\}. \qquad \text{Eq.2.2.9b}$$

At the evaporation front ($x = x_2$), curvature radius $r_y(x_2)$ of corner flow tip is approximated by 0, $\rho(x_2) = 0$, equation 2.2.9b can be modified to

$$Q_{wc}(x,t,\theta) = -\frac{\sigma_{gw} r_p^3}{3\mu_w \alpha(\theta)} \cdot \left\{ \frac{\partial}{\partial x}\{\rho^3(x,t)\} - B_0 \cdot \frac{3}{r_p} \cdot \frac{\partial}{\partial x}\left(\int_x^{x_2} dx \rho^4(x,t)\right) \right\}$$

$$= -\frac{\sigma_{gw} r_p^3}{3\mu_w \alpha(\theta)} \cdot \frac{\partial}{\partial x}\{\rho^3(x,t) - B_0 \cdot I(x,x_2)\} \qquad \text{Eq.2.2.9c}$$

with the bond number $B_0 = \frac{r_p^2 \rho_w g}{\sigma_{gw}}$ and the integral

$$I(x,x_2) = \frac{3}{r_p} \int_x^{x_2} d\tilde{x} \rho^4(\tilde{x},t). \qquad \text{Eq.2.2.9d}$$

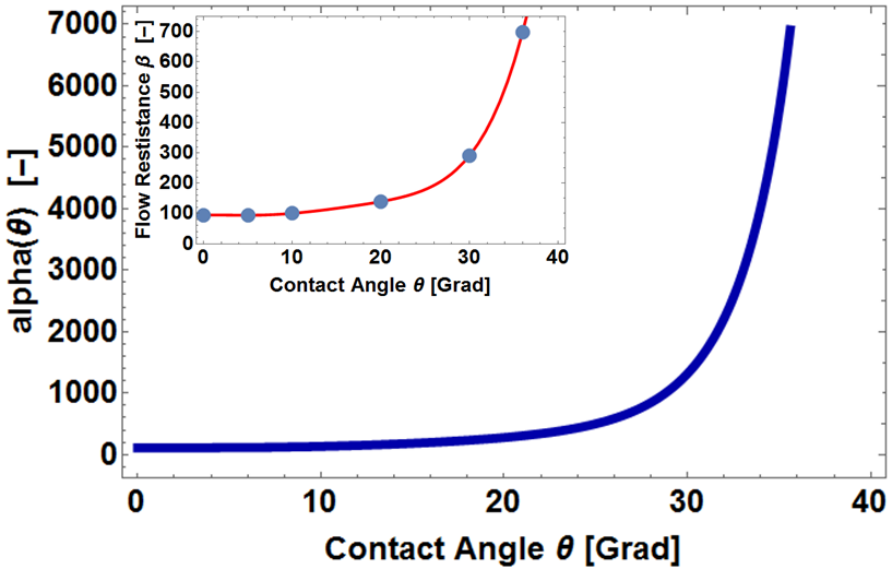

Figure 2. 6 Contact angle dependence of the corner flow caused by a reduced cross section and an increased flow resistance (insert figure). The red curve presents the best fit to the data points (blue dots). Those points are taken from Ransohoff and Radke (1988, Table IV) for the case of a square capillary (corner angle = 90°) and a free water surface (reduced viscosity = 0). The combined effect is expressed by rescaled flow resistance $\alpha(\theta) = \beta(\theta)/C^*(\theta)$.

The derived Q_{wc} is ***volumetric*** corner flow flux. For a control volume in the corner flow region $dV = A \cdot dx$ (Fig. 2.4a), the residual 2D volumetric flux of a sliced cross section (Fig. 2.4b) is

$$\frac{\partial V}{\partial t} = -\frac{\partial Q_{wc}}{\partial x} - Q_{ev}, \qquad \text{Eq.2.2. 10}$$

with the influx Q_{wc} and outflux Q_{ev} (volumetric evaporation flux). As evaporation process is a slow drainage process (capillary number $Ca = \frac{\mu_w u_w}{\sigma_{gw}}$, u_w – velocity of the receding percolation front), the steady-state between corner flow flux and averaged evaporation flux $\langle Q_{ev} \rangle$ is always established. The mass balance over the control volume V at the evaporation front $x = x_2 \equiv -x_i$ is

$$\rho_w \frac{\partial V}{\partial t} \cdot dx = \frac{\partial m_{w0}}{\partial t} = -\rho_w \frac{\partial Q_{wc}}{\partial x} \cdot dx - \langle Q_{ev} \rangle \cdot dx = 0, \qquad \text{Eq.2.2. 11a}$$

where m_{w0} denotes the water mass of the liquid phase in the volume element dV and ρ_w denotes the water density. The averaged evaporation flux $\langle Q_{ev} \rangle$ is given by the first Fick's law

$$\langle Q_{ev} \rangle = A_g \langle j_x^{diff} \rangle \cong -A_g D_g^{eff} \frac{\Delta C}{\Delta x}, \qquad \text{Eq.2.2.11b}$$

where A_g denotes the cross-sectional area of the gas phase at the evaporation front of control volume V. As the water saturation at the evaporation front is approximately 0 (only 4 corner flow tips), A_g is approximated by $A_g^0 = d_0^2$. $\langle j_x^{diff} \rangle$ is the mass evaporation rate density derived from the vapor concentration gradient $\frac{\Delta C}{\Delta x}$ and the effective vapor diffusion coefficient of the water molecules inside the porous media D_g^{eff}. The Millington-Quirk tortuosity model (Millington & Quirk, 1961) was applied for the D_g^{eff}, i.e.

$$D_g^{eff} = D_g^0 \tau, \qquad \text{Eq.2.2.11c}$$

with the tortuosity τ and the temperature-dependent molecular diffusion coefficient $D_g^0(T)$ ($\mathrm{m^2/s}$) given by (Shahraeeni et al., 2012),

$$D_g^0(T) = 2.31 \times 10^{-5} \left(\frac{T}{T_0}\right)^{1.81} (\text{T in K}) \qquad \text{Eq.2.2.11d}$$

$$\tau = (\phi)^{1/3} \quad (\phi \text{ - porosity}). \qquad \text{Eq.2.2.11e}$$

The vapor concentration within the film zone is approximately saturated (C_s). In stage 1, the evaporation front is near the open boundary, $x_2 = 0$, vapor concentration drops rapidly from C_s to the ambient vapor concentration C_a over the viscous boundary layer thickness δ. The vapor concentration gradient is given by

$$\frac{\Delta C}{\Delta x} = \frac{C_a - C_s}{\delta}. \quad \text{Eq.2.2. 12a}$$

In stage 2, the evaporation front has receded into porous media ($x_2 < 0$), the vapor concentration gradient is given by

$$\frac{\Delta C}{\Delta x} = \frac{C_a - C_s}{\delta - x_2}. \quad \text{Eq.2.2.12b}$$

According to the ideal gas law, C_s can be derived by

$$C_s(molar) = \frac{n}{V} = \frac{P_{vapor}(T)}{RT},$$

$$\rightarrow C_s = M_{H_2O} * C_s(molar) \quad \text{Eq.2.2.12c}$$

where R is the ideal gas constant, $P_{vapor}(T)$ is the temperature-dependent saturated vapor pressure, M_{H_2O} is the water molar mass (≈18 *g/mol*). Based on the experimental relative humidity (RH; %), the ambient vapor concentration C_a is determined by

$$C_a = C_s * RH. \quad \text{Eq.2.2.12d}$$

The equation 2.2.9c can be reformulated as

$$Q_{wc}(x, t, \theta) = -\frac{\sigma_{gw} r_p^3}{3\mu_w \alpha(\theta)} \cdot \frac{\partial}{\partial x} \phi(x), \quad \text{Eq.2.2. 13a}$$

with the new variable $\phi(x)$ defined as

$$\phi(x) = \rho^3(x) - B_0 \cdot I(x, x_2). \quad \text{Eq.2.2.13b}$$

Inserting equation 2.2.13a into the mass balance equation 2.2.11a yields

$$\rho_w \cdot \frac{\sigma_{gw} r_p^3}{3\mu_w \alpha(\theta)} \cdot \frac{\partial}{\partial x} \phi(x) = \langle Q_{ev} \rangle \cdot dx. \quad \text{Eq.2.2. 14}$$

Taking differentiations of both sides of Eq. 2.2.14 results

$$\frac{d^2}{dx^2}\phi(x) = \frac{3}{r_p^3}\frac{\mu_w(T)\cdot\alpha(\theta)}{\rho_w\cdot\sigma_{gw}(T)}\cdot\langle Q_{ev}\rangle = b(\theta,T), \quad \text{Eq.2.2. 15a}$$

the contact angle θ and temperature T dependent constant $b(\theta,T)$ as the key variable of the SSC-model c an be further modified as:

$$b(\theta,T) = \frac{3}{r_p^3}\frac{v_w(T)\cdot\alpha(\theta)}{\sigma_{gw}(T)}\cdot\langle Q_{ev}\rangle(T), \quad \text{Eq.2.2.15b}$$

where $v_w(T) = \frac{\mu_w(T)}{\rho_w}$ denotes kinematic viscosity.

Within the film zone, $b(\theta,T) = 0$ ($\Delta C \cong 0$, $\langle Q_{ev}\rangle \cong 0$), $\phi(x)$ is determined by the Laplace equation (Eq.2.2.15a)

$$\Delta_x\phi(x) = 0, \quad \text{Eq.2.2. 16a}$$

which yields a linear curve of $\phi(x)$. As $\rho = 0$ at $x = x_2$, and $\rho = 1$ at $x = x_1$, $\phi(x_1) > \phi(x_2)$ while $x_1 < x_2$, the general solution of equation 2.2.16a is given by

$$\phi(x) = b(x_2 - x). \quad \text{Eq.2.2.16b}$$

Inserting $\frac{\partial}{\partial x}\phi(x) = -b$ back to Eq.2.2.13a, the positive constant b can be determined by the flux-continuity boundary condition at the evaporation front x_2:

$$Q_{wc}\cdot\rho_w = \langle Q_{ev}\rangle, \quad \text{Eq.2.2. 17}$$

which yields $b = b(\theta,T)$.

Horizontal Case ($B_0 = 0$)

For the horizontal case ($B_0 = 0$), the steady-state solutions of $\phi(x)$ (Eq.2.2.16b) at detachment time t_c (red curve) and time $t_c + \Delta t$ (blue curve) are illustrated in Fig.2.7a. The $\phi(x)$ equals to 0 at the corner flow front tips ($x = x_2, r_y \cong 0$); $\phi(x) \cong 1$ at the corner flow root ($x = x_1$, $r_y = r_p$); and $\phi(x) = (r_0/r_p)^3$ at the water meniscus ($r_y = r_0$). The slope of $\phi(x)$, that is, the contact angle θ and temperature T dependent constant $b(\theta,T)$, is determined by the evaporation flux $\langle Q_{ev}\rangle$ (Eq.2.2.15b) and furtherly by the vapor concentration gradient shown in Fig. 2.7b. The evaporation front $x_2(t_c + \Delta t)$ recedes into the pore space in stage 2 and leads to a weaker concentration gradient (blue curve in Fig. 2.7b) than stage 1 (red

curve in Fig. 2.7b), and consequently causes a less steep $\phi(x)$ curve with a smaller $b(\theta, T)$ in Fig. 2.7a. A small recede of the evaporation front (Δx_2) in stage 2 leads to a larger recede of the percolation front (Δx_1), the ratio $\Delta x_1/\Delta x_2 > 1$ and increases with time. The area of the dashed rectangle (Fig. 2.7a): $\{x|x_1(t_c + \Delta t) \leq x \leq 0\} \cap \{y|0 \leq y \leq (r_0/r_p)^3\}$, represents the total water capacity of the evaporating section of a capillary at $t_c + \Delta t$. The area below the $\phi(x)$ curve (e.g. the beige area in Fig. 2.7a) represents the corresponding residual corner flow quantity in the capillary. Therefore, the evaporated water mass loss $\Delta m_w(t)$ is determined by the water capacity subtracting the corresponding residual corner flow area. The blue area in Fig. 2.7a determines the increase of water mass loss $\Delta(\Delta m_w)$ from t_c to $t_c + \Delta t$.

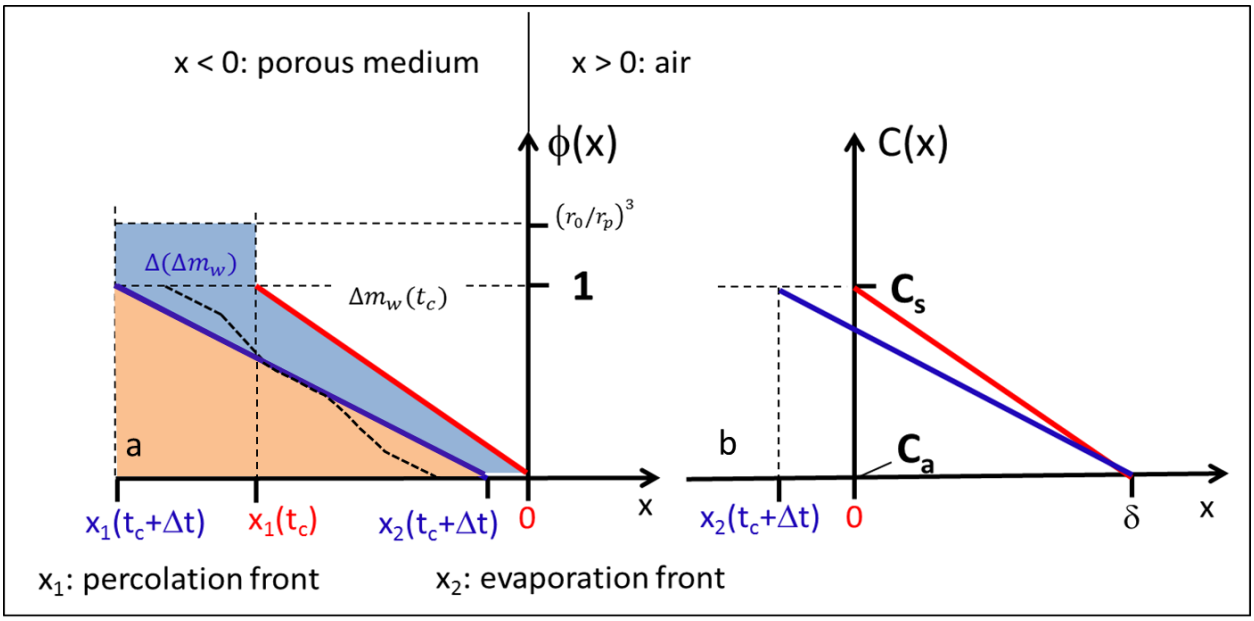

Figure 2. 7 The (a) steady-state solutions of $\phi(x)$ (B_0 = 0, horizontal case) and (b) the corresponding water vapor concentration fields *C(x)* at two different times: (i) at detachment time t_c (red curves), and (ii) at $t_c + \Delta t$ (blue curves). The thick black dashed line in Fig. 2.7a represents a hypothetical solution of a tortuous corner flow path satisfying the correct boundary conditions (modified Fig.7 of Geistlinger et al., 2019).

Derivation of the Detachment Time t_c and the Percolation Front Depth x_p at t_c

As $\phi(x_1) = 1$, the distance between the evaporation front and percolation front $x_2 - x_1$ is given by

$$x_2 - x_1 = \frac{1}{b(\theta,T)}, \quad \text{Eq.2.2. 18a}$$

the percolation front depth x_p at detachment time t_c ($x_2 = 0$) is given by

$$x_p(t_c) = -x_1(t_c) = \frac{1}{b(\theta,T)}. \quad \text{Eq.2.2.18b}$$

The water mass loss Δm_w is the subtraction between the total water capacity of the evaporating section of a capillary m_0 and the residual water mass in the four corners m_w, at detachment time t_c, water mass loss can be estimated by

$$\Delta m_w(t_c) = m_0 - m_w = \rho_w x_p(t_c) {d_0}^2 - \rho_w x_p(t_c) C^*(\theta) r_p^2. \quad \text{Eq.2.2. 19}$$

Since the evaporation rate is constant in stage 1, t_c can be deduced by

$$t_c = \frac{\Delta m_w(t_c)}{\langle Q_{ev} \rangle}. \quad \text{Eq.2.2. 20}$$

Stage 2 Water Mass Loss ($B_0 = 0$)

The water mass loss in stage 2 is given by

$$\Delta m_w(x_2) = m_0 - m_w = -\rho_w x_1 d_0^2 - \rho_w \cdot \int_{x_1}^{x_2} dx \cdot C^* r_y^2, \quad \text{Eq.2.2. 21a}$$

with a new variable $\xi(x) = \rho^3(x)$, equation 2.2.21a can be reformulated by

$$\Delta m_w(x_2) = -\rho_w x_1 d_0^2 - \rho_w C^* r_p^2 \cdot \int_{x_1}^{x_2} dx \cdot \xi(x)^{\frac{2}{3}}. \quad \text{Eq.2.2.21b}$$

Note $B_0 = 0$, $\xi(x) = \phi(x) = b(x_2 - x)$ (Eq. 2.2.16b). Equation 2.2.21b is reformulated by,

$$\Delta m_w(x_2) = -\rho_w x_1 d_0^2 - \frac{3}{5}\rho_w \cdot C^* \cdot r_p^2 \cdot b^{\frac{2}{3}} \cdot (x_2 - x_1)^{\frac{5}{3}}. \quad \text{Eq.2.2.21c}$$

When $\phi(x_1) = 1$, $x_2 - x_1 = \frac{1}{b}$ (Eq.2.2.18a), equation 2.2.21c can be modified as

$$\Delta m_w(x_2) = \rho_w \cdot d_0^2 (\frac{1}{b} - x_2) - \frac{3}{5}\rho_w \cdot C^* \cdot r_p^2 \cdot \frac{1}{b}$$

$$= \left(\rho_w \cdot d_0^2 - \frac{3}{5}\rho_w \cdot C^* \cdot r_p^2\right) \cdot \frac{1}{b} - \rho_w \cdot d_0^2 \cdot x_2$$

$$= -a_0 \cdot x_2 + \frac{a_1}{b}, \qquad \text{Eq.2.2. 22a}$$

with the θ and T dependent constants a_i given by

$$a_0(T) = \rho_w(T) d_0^2, \qquad \text{Eq.2.2.22b}$$

$$a_1(\theta, T) = a_0(T) - \frac{3}{5}\rho_w(T) C^*(\theta) r_p^2(\theta). \qquad \text{Eq.2.2.22c}$$

The constant b can be replaced by

$$b = \frac{3}{r_p^3} \cdot \frac{\nu_w(T)\alpha(\theta)}{\sigma_{gw}(T)} \cdot \left(-A_g^0 D_g^{eff} \frac{\Delta C}{\delta - x_2}\right) = \frac{a_2}{\delta - x_2}, \qquad \text{Eq.2.2. 23a}$$

with a_2 given by

$$a_2(\theta, T) = -\frac{3}{r_p^3(\theta)} \frac{\nu_w(T)\alpha(\theta)}{\sigma_{gw}(T)} \cdot A_g^0 D_g^{eff}(T) \Delta C(T). \qquad \text{Eq.2.2.23b}$$

Equation 2.2.22a can be further modified as

$$\Delta m_w(x_2) = -a_0 \cdot x_2 + \frac{a_1}{a_2}(\delta - x_2)$$

$$= \frac{a_1}{a_2} \cdot \delta - \left(a_0 + \frac{a_1}{a_2}\right) \cdot x_2$$

$$= a_3 - a_4 \cdot x_2, \qquad \text{Eq.2.2. 24a}$$

with the θ and T dependent constants a_3 and a_4 given by

$$a_3(\theta, T) = \frac{a_1}{a_2}\delta, \qquad \text{Eq.2.2.24b}$$

$$a_4(\theta, T) = a_0 + \frac{a_1}{a_2}. \qquad \text{Eq.2.2.24c}$$

The x_2-derivation of $\Delta m_w(x_2)$ is

$$\frac{d\Delta m_w}{dx_2} = \frac{d\Delta m_w}{dt} \cdot \frac{dt}{dx_2} = \langle Q_{ev} \rangle \frac{dt}{dx_2} = -a_4. \qquad \text{Eq.2.2. 25}$$

Inserting the expression of $\langle Q_{ev} \rangle$ yields the ordinary differential equation for $x_2(t)$

$$-A_g^0 D_g^{eff} \frac{\Delta C}{\delta - x_2} \cdot \frac{dt}{dx_2} = -a_4,$$

$$\frac{dx_2}{dt} = \frac{A_g^0 D_g^{eff} \Delta C}{(\delta - x_2) a_4} = \frac{a_5}{a_4} \cdot \frac{1}{(x_2 - \delta)}$$

$$= \frac{1}{a_6} \cdot \frac{1}{(x_2 - \delta)}, \qquad \text{Eq.2.2. 26a}$$

with the θ and T dependent constants a_5 and a_6 given by

$$a_5(T) = -A_g^0 D_g^{eff} \Delta C, \qquad \text{Eq.2.2.26b}$$

$$a_6(\theta, T) = \frac{a_4}{a_5}. \qquad \text{Eq.2.2.26c}$$

Making integral of both sides of the equation $\frac{dt}{dx_2} = a_6 \cdot (x_2 - \delta)$ gives

$$t = \frac{1}{2} a_6 \cdot {x_2}^2 - a_6 \cdot \delta \cdot x_2,$$

$$(x_2 - \delta)^2 = \delta^2 + \frac{2t}{a_6},$$

$$|x_2 - \delta| = \sqrt{\delta^2 + \frac{2t}{a_6}}, \qquad \text{Eq.2.2. 27a}$$

as $x_2 < 0$ and $\delta > 0$, the evaporation front depth x_i is derived by

$$x_i(t) \equiv |x_2(t)| = \sqrt{\delta^2 + \frac{2t}{a_6}} - \delta = \delta \cdot \left(\sqrt{1 + \frac{2\Delta t}{a_6 \delta^2}} - 1 \right), \qquad \text{Eq.2.2.27b}$$

with $\Delta t = t - t_c$.

Applying the $|x_2(t)|$ and Eq.2.2.23a, the percolation front depth x_p is given by

$$x_p(t) \equiv |x_1(t)| = |x_2(t)| + \frac{1}{b} = |x_2(t)| + \frac{\delta - x_2}{a_2}$$

$$= \frac{\delta}{a_2} + (1 + \frac{1}{a_2}) x_i(t). \qquad \text{Eq.2.2. 28}$$

SSC-Model Workflow for Horizontal Case

The SSC-modeling is conducted in Wolfram Mathematica. Figure 2.8 displays the workflow for the horizontal case. In step 1, the input experimental detachment time t_c and percolation front depth x_p at t_c are derived by image processing (IP; detailed method see Chapter 3). The vapor concentrations in step 3 are calculated by the Eqs.2.2.12c & 2.2.12d. The imported physico-chemical parameters $P_{vapor}(T)$, $\mu_w(T)$, $\sigma_{gw}(T)$ and flow resistance $\beta(\theta)$ are empirical data from literatures (Appendix I, II). Since the x_p at t_c is temperature and contact angle dependent (Eq.2.2.18b), in step 6, with the "FindRoot" function in Mathematica, an analytical contact angle $\theta(x_p)$ can be deduced by applying the experimental $x_p(t_c)$. Similarly, an analytical contact angle $\theta(t_c)$ can be deduced in step 7 by applying the experimental t_c. The analytical mass loss curve considers stage 1 with a constant $\langle Q_{ev} \rangle$ and a linear mass loss curve. Eq. 2.2.24a gives the x_2-dependence of stage 2 mass loss Δm_w, while x_2 itself is time-dependent (Eq. 2.2.27b; $x_2 = -x_i$), which eventually gives the stage 2 mass loss curve versus evaporation time.

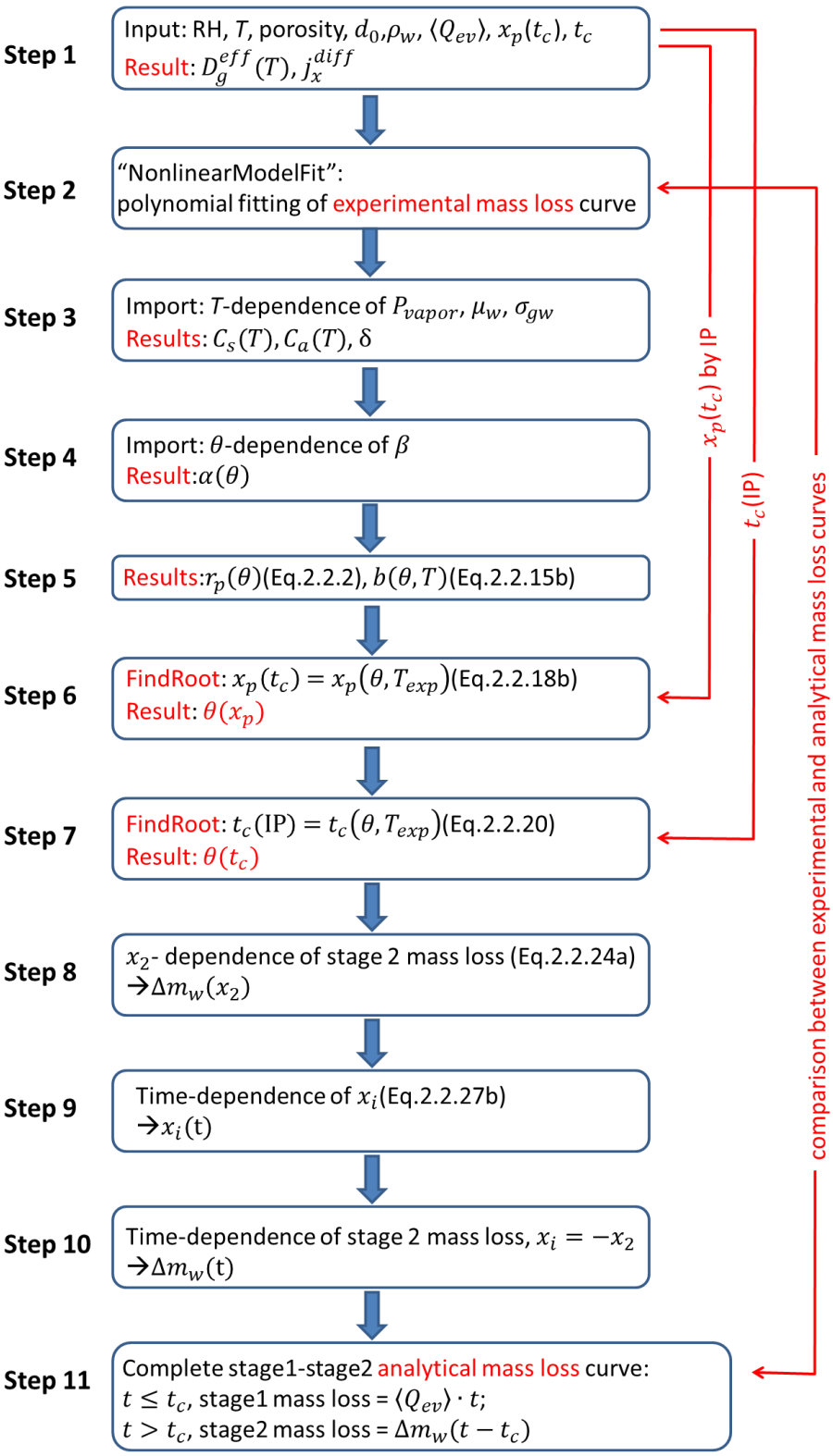

Figure 2. 8 SSC-model workflow for the horizontal case. Note that, P_{vapor} is the saturated vapor pressure, $\Delta x(T)$ gives experimental boundary layer thickness, T represents temperature and t represents time.

Vertical Case ($B_0 \neq 0$)

For vertical case, with the general solution of $\phi(x) = b(x_2 - x)$(Eq.2.2.16b), the variable $\xi(x) = \rho^3(x)$ can be represented by (Eq.2.2.13b)

$$\xi(x) = b \cdot (x_2 - x) + \frac{3B_0}{r_p} \cdot \int_x^{x_2} dx \rho^4(x)$$

$$= b \cdot (x_2 - x) + \varepsilon \cdot \int_x^{x_2} dx \cdot \xi(x)^{4/3}, \qquad \text{Eq.2.2. 29a}$$

with

$$\varepsilon = \frac{3B_0}{r_p}. \qquad \text{Eq.2.2.29b}$$

To solve this integral function, $\varepsilon \cdot \int_x^{x_2} dx \cdot \xi(x)^{4/3}$ is approximated by a power series expansion $\sum_{n=0}^{\infty} f_n \cdot x^n$,

$$\xi^n(x) \cong b(x_2 - x) + f_0 + f_1 \cdot x + f_2 \cdot x^2 + f_3 \cdot x^3 + \cdots + f_n \cdot x^n. \qquad \text{Eq.2.2. 30}$$

The $\xi^0(x)$ is given by the horizontal case where $\varepsilon = 0$,

$$\xi^0(x) = b(x_2 - x) = b\Delta x, f_0 = 0. \qquad \text{Eq.2.2. 31a}$$

The $\xi^1(x)$ is given by

$$\xi^1(x) \cong b(x_2 - x) + f_0 + f_1 \cdot x$$

$$= b(x_2 - x) + \varepsilon \cdot \int_x^{x_2} dx \, [\xi^0(x)]^{4/3}$$

$$= \xi^0(x) + \varepsilon \cdot b^{4/3} \cdot \int_x^{x_2} dx \, \Delta x^{4/3},$$

set $x_2 - x = \Delta x = \tilde{x}$, taking differentials of this equation gives $-dx = d\tilde{x}$, hence $\xi^1(x)$ can be reformulated by

$$\xi^1(x) = \xi^0(x) + \varepsilon \cdot b^{4/3} \cdot \int_0^{\Delta x} d\tilde{x} \cdot \tilde{x}^{4/3}$$

$$= \xi^0(x) + (b\Delta x)^{4/3} \cdot \frac{\varepsilon \cdot \Delta x}{\frac{7}{3}}, \qquad \text{Eq.2.2.31b}$$

with $f_1 \cdot x = (b\Delta x)^{4/3} \cdot \frac{\varepsilon \cdot \Delta x}{\frac{7}{3}}$.

For each grade of $\xi^{n+1}(x)$ expansion, there is a new term $f_{n+1} \cdot x^{n+1} = \varepsilon \cdot \int_x^{x_2} dx \cdot f_n \cdot x^n$. The $\xi^2(x)$ is given by

$$\xi^2(x) \cong b(x_2 - x) + f_0 + f_1 \cdot x + f_2 \cdot x^2$$

$$= \xi^1(x) + \varepsilon \cdot \int_x^{x_2} dx \cdot f_1 \cdot x$$

$$= \xi^1(x) + \varepsilon \cdot \int_0^{\Delta x} d\tilde{x} \cdot (b\Delta x)^{4/3} \cdot \frac{\varepsilon \cdot \Delta x}{\frac{7}{3}}$$

$$= \xi^1(x) + (b\Delta x)^{4/3} \cdot \frac{(\varepsilon \Delta x)^2}{\frac{7}{3}, \frac{10}{3}}, \qquad \text{Eq.2.2.31c}$$

with $f_2 \cdot x^2 = (b\Delta x)^{4/3} \cdot \frac{(\varepsilon \Delta x)^2}{\frac{7}{3}, \frac{10}{3}}$.

Similarly, $\xi^3(x)$ can be derived by

$$\xi^3(x) \cong b(x_2 - x) + f_0 + f_1 \cdot x + f_2 \cdot x^2 + f_3 \cdot x^3$$

$$= \xi^2(x) + \varepsilon \cdot \int_x^{x_2} dx \cdot f_2 \cdot x^2$$

$$= \xi^2(x) + \varepsilon \cdot \int_0^{\Delta x} d\tilde{x} \cdot (b\Delta x)^{4/3} \cdot \frac{(\varepsilon \Delta x)^2}{\frac{7}{3}, \frac{10}{3}}$$

$$= \xi^2(x) + (b\Delta x)^{4/3} \cdot \frac{(\varepsilon \Delta x)^3}{\frac{7}{3}, \frac{10}{3}, \frac{13}{3}}. \qquad \text{Eq.2.2.31d}$$

Therefore, the *n*-th approximation of $\xi(x)$ is given by

$$\xi^n(x) = b\Delta x \left\{1 + (b\Delta x)^{1/3} \sum_{k=1}^{n} \frac{(\varepsilon \Delta x)^k}{f_1 \cdots f_k}\right\}, \qquad \text{Eq.2.2. 32}$$

with $f_k = \frac{4}{3} + k$. The convergence of the power-series solution Eq.2.2.32 is proven for $n = 3$ ($B_0 \cong 10^{-3}$) by the percolation front depth as a function of the evaporation front, that is, $x_p(x_i)$ shown in in Fig. 2.9 (Geistlinger, et.al., 2019).

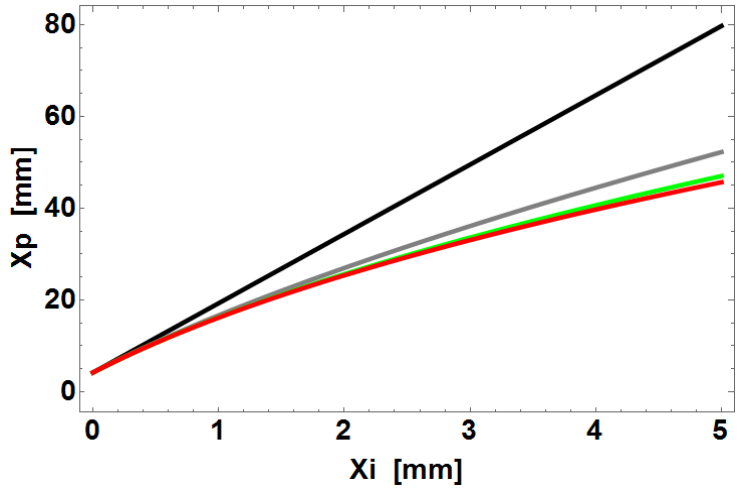

Figure 2. 9 The percolation front x_p versus the evaporation front x_i. Comparison of the solutions $\xi^{(n)}(x)$ (Eq. 2.2.32) for n = 0 (black curve, horizontal case), n = 1 (gray curve), n = 2 (green curve), and n = 3 (red curve).

To calculate the distance between the evaporation front (x_2) and percolation front (x_1) for vertical case, the implicit equation

$$\xi^{(n)}(x_1, x_2) = 1 \qquad \text{Eq.2.2. 33}$$

has to be solved.

Figure 2.10 displays the workflow of SSC-model for vertical case, where the first five steps are the same as the horizontal case. With the known experimental temperature, $\xi^{(n)}(x)$ is determined by x, x_i and θ. The analytical solution of $x_p(x_i, \theta)$ is derived by finding out the x when $\xi^{(n)}(x, x_i, \theta) = 1$, with the "FindRoot" function (step 6). In the next step, the SSC model runs iteration. With the $x_i = 0$ and the experimental $x_p(t_c)$ from IP, define

$$f(\theta) = x_p(x_i, \theta) - x_p(t_c), \qquad \text{Eq.2.2. 34a}$$

and

$$\theta_{i+1} = \theta_i - \frac{\theta_i - \theta_{i-1}}{f(\theta_i) - f(\theta_{i-1})} * f(\theta_i). \qquad \text{Eq.2.2.34b}$$

With two given initial values θ_1 and θ_2, when $|\theta_{i+1} - \theta_i| < 0.01$ is satisfied, the loop terminates and the deduced contact angle $\theta(x_p) = \theta_{i+1}$. Applying the deduced $\theta(x_p)$ value in the model gives the x_i-dependence of x_p (step 8).

The mass loss Δm_w is estimated as

$$\Delta m_w(x_i, \theta) = \rho_w x_p(x_i, \theta) {d_0}^2 - \rho_w C^*(\theta) r_p(\theta)^2 \int_0^{x_p(x_i,\theta)} \xi^{(3)}(x, x_i, \theta)^{2/3} dx, \qquad \text{Eq.2.2. 35a}$$

and the analytical detachment time is given by

$$t_c(\theta) = \frac{\Delta m_w(x_i,\theta)}{\langle Q_{ev} \rangle}, \ \ (x_i = 0). \qquad \text{Eq.2.2.35b}$$

Iteration is conducted again in step 9. With the experimental t_c derived from IP. Define

$$g(\theta) = t_c(\theta) - t_c(\text{IP}), \qquad \text{Eq.2.2. 36a}$$

and

$$\theta_{i+1} = \theta_i - \frac{\theta_i - \theta_{i-1}}{g(\theta_i) - g(\theta_{i-1})} * g(\theta_i), \qquad \text{Eq.2.2.36b}$$

when $|\theta_{i+1} - \theta_i| < 0.01$ is satisfied, the loop terminates and the deduced contact angle $\theta(t_c) = \theta_{i+1}$. Inputting the $\theta(t_c)$ value into the model derives the x_i-dependence of analytical mass loss Δm_w (step 10). Next, a polynomial fitting of $\Delta m_w(x_i)$ is achieved by

$$\Delta m_w(x_i) = \Delta m_w(0) + C_1 x_i + C_2 {x_i}^2 + C_3 {x_i}^3, \qquad \text{Eq.2.2. 37a}$$

with the best fitting parameters C_1, C_2 and C_3. As the evaporation rate can be represented by the differential of mass loss $\Delta m_w(x_i)$

$$\langle Q_{ev} \rangle = A_g D_g^{eff} \frac{|\Delta C|}{\Delta x} = \frac{d}{dt} \Delta m_w(x_i), \qquad \text{Eq.2.2.37b}$$

the x_i-dependence of evaporation time is given by

$$dt(x_i) = \frac{\Delta x}{A_g D_g^{eff} |\Delta C|} d\Delta m_w(x_i). \qquad \text{Eq.2.2.37c}$$

Inverting the X and Y coordinates of the $t(x_i)$ curve, the time-dependence of $x_i(t)$ and furtherly the time-dependency of mass loss $\Delta m_w(t)$ can be derived.

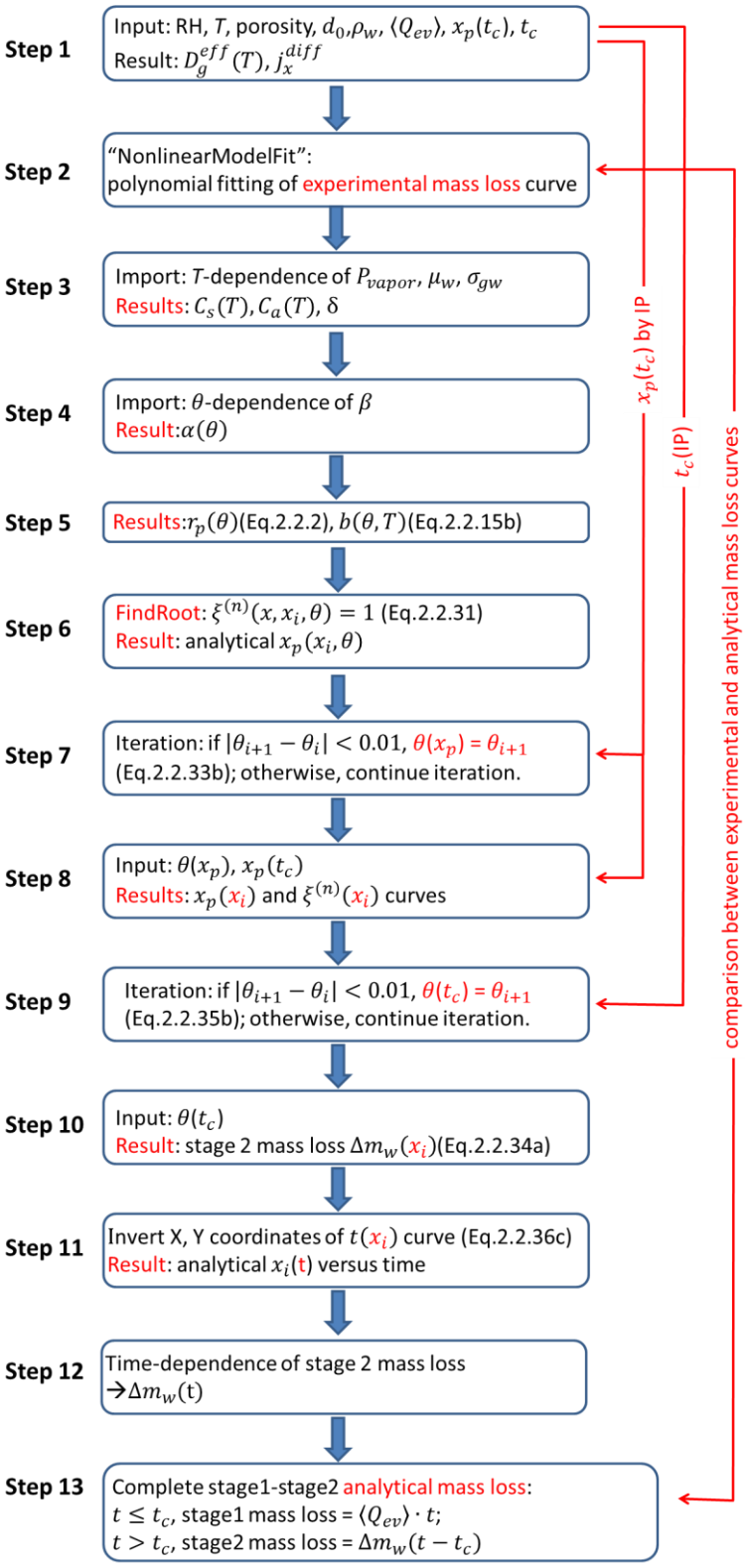

Figure 2. 10 SSC-model workflow for vertical case. Note that, P_{vapor} is the saturated vapor pressure, $\Delta x(T)$ is boundary layer thickness, T represents temperature and t represents time.

2.3 Corner Flow and Thick-Film Flow Mechanisms

2.3.1 Full Bulk Flow versus Corner Flow and Thick-Film flow

The IPE model assumes that evaporation starts at the large pore menisci and "capillary pumping" from these large pores to smaller pores determine the early-stage of evaporation (stage 1). The key parameter is the pore size distribution, or more specific the PSD of the hydraulic connected region. The PSD of the micromodels (Fig. 3.6) corresponds to that of coarse sand with a mean pore radius of approximately 100 - 200 μm (Geistlinger and Zulfiqar, 2020), which causes a high hydraulic conductivity. Hence, viscous forces can be neglected in case of low-demand evaporation rate (Ca ≈ 10^{-7}- 10^{-8}; see Fig. 1b in Shahraeeni et al., 2012), and the stage1-behaviour is controlled by water redistribution along the water pressure gradient from large to small pores. If the menisci have receded into the pores, water flow still exists within the pore corners and along the rough pore surfaces. Both water flows, which will be discussed next, are dependent on geometric properties and wettability of the inner pore-solid interface.

2.3.2 Corner Flow Dynamics

A cross-sectional schematic at the open boundary ($x = x_0$) of such an effective square capillary of SSC-model is shown in Fig. 2.11b. The vertical cross-sectional schematic along the ***diagonal cross-section*** of the capillary (red-dashed rectangle in Fig. 2.11a) is displayed in Fig. 2.11c, indicating the water-air interface movement from time t_0 to t_3. Before evaporation starts (t_0), the capillary is initially saturated with a meniscus Σ, some water remains in the sharp corners, and the water-air interface at the open boundary is marked by the solid black curves in Fig. 2.11b. During evaporation, the bulk flow (BF) recedes into the pore channel with a stable curvature, and the corner flow (CF) extends from the water meniscus to the open surface. Meanwhile, CF recedes into the corners with decreasing thickness and increasing curvatures (red arrow in Fig. 2.11b), until only the CF front tips are left at the open surface (e.g. t_2 in Fig. 2.11c). For CF, the curvature along the x-direction can be neglected compared to the curvature in the y-direction (perpendicular to the x-direction). Therefore, the capillary pressure at the CF root (transition zone from BF into CF; e.g.$x_1(t_1)$, $x_2(t_2)$, and $x_3(t_3)$ in Fig. 2.11c) equals the capillary pressure at the BF meniscus given by the Young-Laplace equation:

$$P_c(x_\Sigma) = P_c(x_1(t_1)) = P_c(x_2(t_2)) = P_c(x_3(t_3)) = \sigma_{gw} \cdot H\left(r_x, r_y\right) \cong \frac{\sigma_{gw}}{r_{y(-x_p)}}, \qquad \text{Eq.2.3. 1}$$

where the terms r_x and r_y are the curvature radii at the CF root ($x = -x_p$) in the principal directions x and y, respectively (Geistlinger et al., 2019).

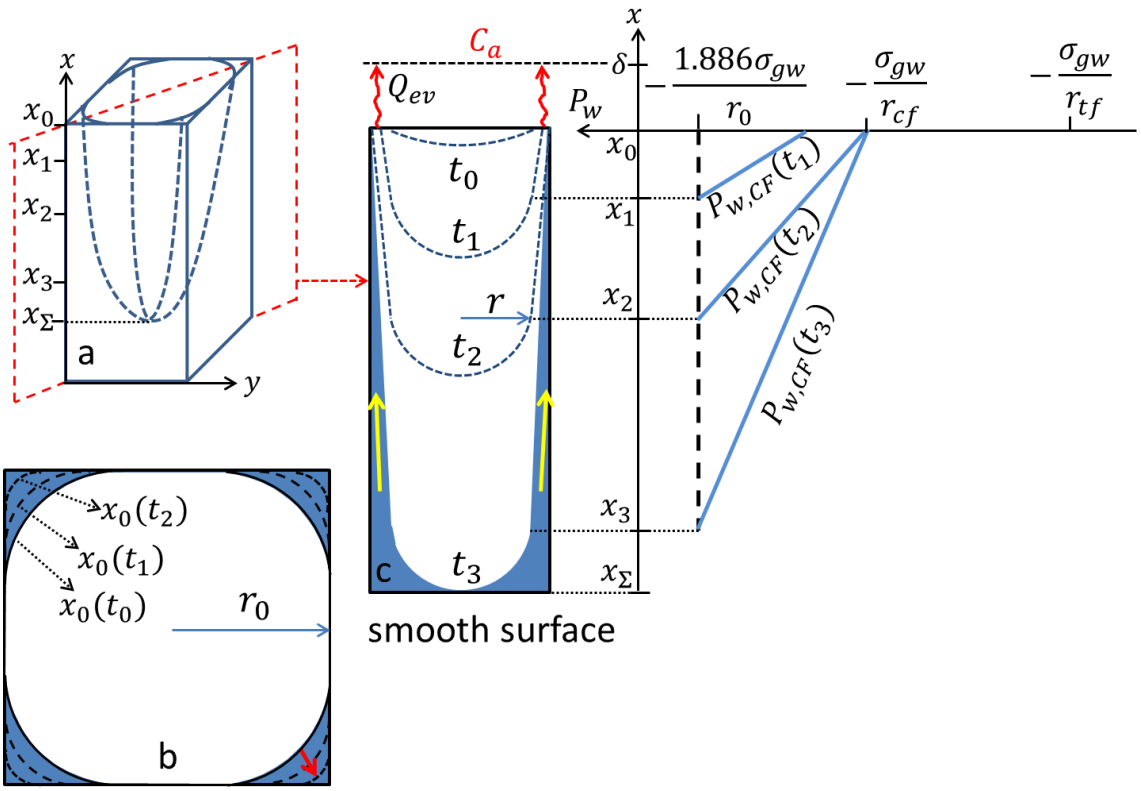

Figure 2. 11 Schematics of a square capillary with smooth surface (where corner flow occurs) and the water pressure distribution: (a) Perspective drawing of the square capillary; (b) horizontal cross-sectional schematic of the square capillary at the open surface with a marked water-air interface (black solid curves) and the corner flow phase (blue); (c) vertical cross-sectional schematic along the ***diagonal cross-section*** of the square capillary (red-dashed rectangle in Fig. 2.11a) with water-air interface movement from t_0 to t_3; the corner flow water pressure $P_{w,CF}$ decreases along the CF direction (yellow arrow). The r_0, r_{cf} and r_{tf} denote the mean capillary radius, curvature radii at CF and TFF front tips, respectively (Fig. 6; Ding & Geistlinger, 2021).

For a contact angle $\theta = 0°$, $F(0) = 1 + \frac{\sqrt{\pi}}{2} \approx 1.886$ (Eq.2.2.2b), the capillary pressure at the CF root is $P_c = \frac{1.886\sigma_{gw}}{r_0}$, and for a typical contact angle of the oxidized Si-surface with $\theta \cong 40°$ (Geistlinger et al., 2019), the capillary pressure is reduced by approximately 30%. Note that, *F(θ)* becomes undefined (= 0/0) at the critical contact angle of 45° and consequently, CF is not possible.

Equilibrium between capillary pressure P_c, air pressure P_g, and water pressure P_w is established at the water-air interface in steady state: $P_c = P_g - P_w$, which yields the water pressure $P_w = -P_c$ ($P_g \cong 0$). At the CF front tip, the water pressure is approximated by $P_{w,CF} = -\frac{\sigma_{gw}}{r_{cf}}$ with curvature radius r_{cf}. The water pressure gradient $\Delta P_w = \frac{\sigma_{gw}}{r_{cf}} - \frac{1.886\sigma_{gw}}{r_0}$ (Fig. 2.11c) drives the continuous transport of water from the BF towards the open surface through the four CF paths.

Owing to the exchange of water-air molecules along the entire water-air interface, the vapor concentration is nearly saturated within the CF region. When further water supply from BF was hindered (t_3 in Fig.2.11c), the CF front tip becomes dry, and the CF can no longer extend to the open surface, defined as the hydraulic detachment. Consequently, a completely dry region is formed above the CF front. The vapor concentration undergoes a decline from the saturated vapor concentration C_s in the CF region to the ambient vapor concentration C_a at the boundary layer $x = \delta$. The averaged evaporation rate can be described by the diffusion flux based on Fick's first law

$$\langle Q_{ev} \rangle = A_g \langle j_x^{diff} \rangle \cong -A_g D_g^{eff} \frac{\Delta C}{\Delta x} = -A_g D_g^{eff} \frac{C_a - C_s}{\delta + |x_i|}, \qquad \text{Eq.2.3. 2}$$

where A_g denotes the cross-sectional area of the gas phase, j_x^{diff} is the diffusion flux, D_g^{eff} is the effective gas-phase diffusion coefficient of the water molecules, and $|x_i|$ is the distance between the evaporation front and open surface. In stage 1, $|x_i| = 0$, the evaporation rate remains constant. After the CF detaches away from the open surface, the evaporation rate drops owing to the decreasing vapor concentration gradient, characterized as stage 2.

Physically, one expects that viscous forces/dissipation control the CF during stage2, because of the small effective cross section in the upper section near the evaporation front (Fig. 2.11). Besides the geometry of the pore channels, also the physico-chemical state of the pore-solid surface (wettability, contact angle) has a significant impact on the CF and implicitly on the evaporation rate. Since the measured contact angle on oxidized Si-surfaces is approximately 40° (Geistlinger et al., 2019), it will reduce CF significantly compared to complete wetting.

2.3.3 Thick-Film Flow Dynamics

In addition to corner flow, the capillary with rough inner surface also has the thick-film flow (TFF), which refers to the water retained in the surface cavities during evaporation. As a film carpeting the rough surface, TFF has a water-air interface at the film front with curvature radius r_{tf} along x-direction ($r_{tf} \ll r_0$); curvature along y-direction can be neglected. Water is transported from BF towards TFF under the water pressure gradient between the BF meniscus and TFF front tips according to the following equation:

$$\Delta P_w = \frac{\sigma_{gw}}{r_{tf}} - \frac{1.886\sigma_{gw}}{r_0}. \quad \text{Eq.2.3. 3}$$

From t_0 to t_3 (CF detachment time), the TFF carpets the entire rough surface of the partially wet pore (Fig. 2.12c). Instead of the four corners in Fig. 2.11b, the interconnected CF and TFF cover the entire perimeter of the open capillary surface as evaporation exits of the capillary with rough surface (Fig. 2.12b). CF (with flux Q_{wc}) and TFF (with flux Q_{wf}) directly contribute to the evaporation flux: $Q_{ev} = Q_{wc} + Q_{wf}$. The capillary inner surface area covered by BF and CF is gradually replaced by TFF during the CF shrinking and BF receding processes. Owing to the water pressure gradient: $P_{w,BF} > P_{w,CF} > P_{w,TFF}$, after water supply from BF vanishes (t_3), TFF can still be supplied by CF and maintains the hydraulic connection to the open surface, prolonging stage 1. Therefore, TFF detachment, not CF detachment from the open surface defines the end of stage 1 for porous media with rough inner surface.

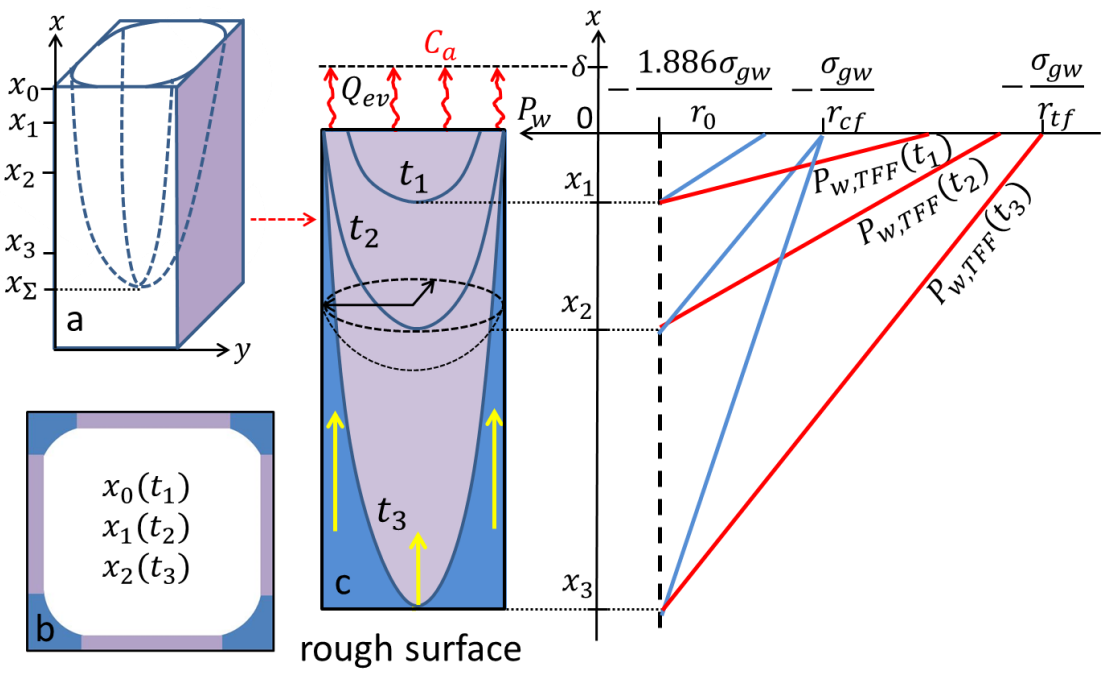

Figure 2. 12 Schematics of the square capillary with rough surface (where both corner flow and thick-film flow occur) and water pressure distribution: (a) Perspective drawing of the square capillary; (b) horizontal cross-sectional schematic of the partially wet pore region where corner flow (blue) and thick-film flow (lilac) coexist; and (c) vertical cross-sectional schematic of the square capillary ***side surface*** (colored lilac in Fig. 2.12a); the dark blue curves represent the interface between corner flow and thick-film flow on the capillary surface, and the bulk flow meniscus is indicated by black dashed lines; water pressures $P_{w,CF}$ (blue lines) and $P_{w,TFF}$ (red lines) of corner and thick-film flow, respectively, decrease along the CF and TFF directions (yellow arrows). The r_0, r_{cf} and r_{tf} denote the mean capillary radius, curvature radii at CF and TFF front tips, respectively (Fig. 7; Ding & Geistlinger, 2021).

3 Material and Methods

3.1 Micromodel Fabrication

Advanced imaging techniques, such as Focused Ion Beam Scanning Electron Microscopy (FIB-SEM) and X-ray microcomputed tomography (micro-CT), have been applied quite often in porous media research to obtain 2D or 3D high resolution static images. However, the long scanning time (on the order of minutes or even hours) makes it difficult to capture the real-time dynamics of flow (Anbari et al., 2018). As alternative method, micromodel is a transparent interconnected porous network which enables the direct visualization of the complex fluid structure and flow dynamics in pore scale. A 2D micromodel consists of single-layer microfluidic channels with arbitrary porous structure.

I applied four micromodels for the evaporation experiments. According to the different materials (silicon vs glass-ceramic) and pore structures (MM4 vs MM5), the micromodels were named by MM4-Si, MM4-glass, MM5-Si and MM5-glass respectively. All the micromodels were designed in identical size of 80 mm × 80 mm and with uniform inner channel depth of 300 μm.

3.1.1 Microstructure MM4 and MM5

Irregular Pore Structure MM4

The irregular pore structure MM4 (Fig. 3.1a) was derived based on a 3D-2D topological mapping algorithm, which used the horizontal and vertical chord length distribution (CLD) of grains and pores as mapping constraints. The chord length distributions can sensitively reflect the morphology and topology of pore space and the grain geometry (Brücher & Bottlinger, 2006). For example, a high fraction of long chords indicates strong connected pore systems while a high fraction of short chords is possessed of dense pore systems. A high peak in the grain-CLD represents a narrow particle size distribution, and a second weak peak in the grain-CLD indicates contact points between neighboring grains. Non-spherical grains show an asymmetry between horizontal and vertical chords. The CLDs of a 1mm-sand (details see Geistlinger et al., 2015) were used for the 3D-2D-mapping, the 2D structure MM4 maintains similar morphological, topological, and geometrical properties as the 3D sample. The porosity of structure MM4 is 0.42 and the mean pore radius is approximately 205 μm (given by the PSD analysis with the maximum-inscribed-sphere method; plugin “Local thickness” in ImageJ, Dougherty & Kunzelmann, 2007).

Regular Pore Structure MM5

The regular pore structure MM5 (Fig. 3.1b) is a quadratic lattice pore network containing 80 × 80 grain particles, the geometrical centers of the grain particles are equidistant and connected by lognormal

distributed throats with a throat width $d_{mean} = 400 \pm 62\mu m$ (generated by Matlab). The porosity of MM5 is 0.52. Note that, this microstructure is similar to that used by Lenormand et al. (1988) for deriving their famous phase diagram on fluid pattern formation, the mean throat width of 350 μm corresponds to the throat width of 400 μm of our MM5-microstructure.

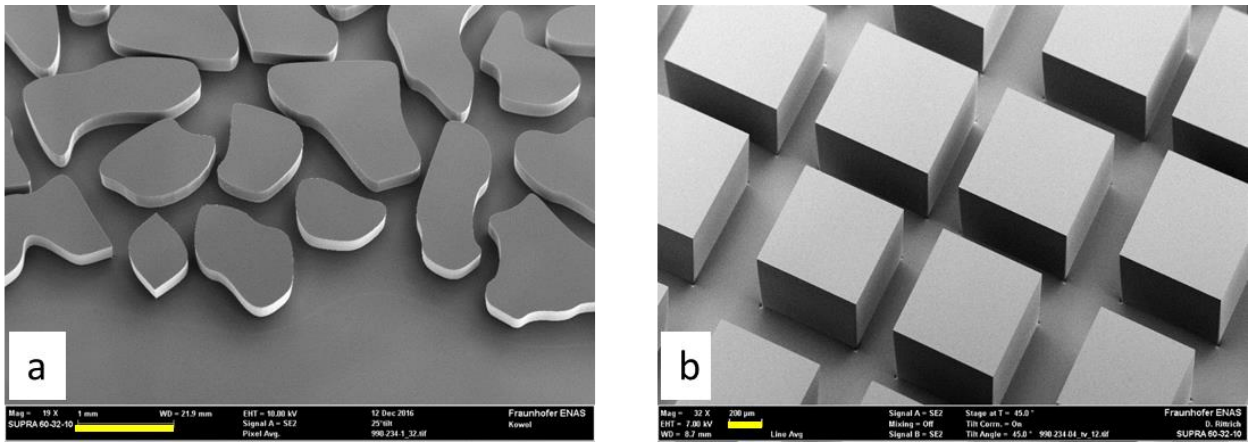

Figure 3. 1 SEM images of micromodels with different pore structures: (a) irregular pore structure MM4 (scalebar = 1 mm); (b) quadratic lattice pore structure MM5 (scalebar = 200 μm).

3.1.2 Silicon Micromodel Construction

The silicon micromodels were constructed by the inductively coupled plasma-deep reactive ion etching (ICP-DRIE) technology (Küchler et al., 2003; Zuo et al., 2013), which provides high edge steepness and absolute smoothness of the inner surface (Fig. 3.2a, 3.2b). This etching technic minimized the underetching to 1.2° deviation from the vertical line and maximal 10 μm deviation from the horizontal bottom line, which reduced the corner rounding effects to the largest extent compared to some other etching methods (Zuo et al., 2013; Vorhauer et al., 2015). A chromium-coated soda lime photomask of 7 in. size (based on the Matlab-generated mask) was patterned, a cleaned *p*-type silicon wafer with (100) orientation, 150 mm diameter and 675 μm thickness was coated by a 2-μm-thick oxide film by wet thermal oxidation, followed by 8-μm-thick resist (AZ9260) coverage. The mask pattern was transferred from the photomask onto the resist layer by contact lithography and then into the oxide layer by plasma etching on an SPTS DSi Rapier ICP etcher. Subsequently, the silicon trenches were etched to a depth of 300 μm by DRIE carried on the same DSi Rapier ICP tool. After DRIE, the remaining resist was removed by oxygen plasma ashing and the oxide layer by buffered oxide etching. A 50-nm-thin silicon oxide layer

was formed on the structured silicon wafer surface by dry oxidation to ensure a similar wetting behavior like siliceous surface. The structured wafer was then covered by a borosilicate glass wafer (Schott Borofloat 33, 1 mm thick) by anodic bonding (400°C, 600-800 V).

3.1.3 Glass-Ceramic Micromodel Construction

The glass-ceramic micromodels were constructed by a photolithographic etching method which provides the accuracy in the order of 10-μm considering the sharpness of the grain wall. The solid material, photosensitive glass-ceramic FOTURAN (Schott GmbH) has a rough surface with mean roughness of 1-3 μm (Fig. 3.2c) as provided by the producer (Invenios Europe GmbH). The estimated surface roughness parameters (ISO-standard, 1997; Voburger & Raja, 1990) are the mean surface height $R_a(= 1\mu m)$ and the wavelength parameter $D(= 2\mu m)$ which indicate the periodicity of the surface (Geistlinger et al., 2016). The chemically etched glass micromodels were covered with a plain glass plate by thermal diffusion bonding (500°C). After the micromodel construction, the etched structures were flushed with isopropanol and water in turn, and dried at 200°C.

Again, I emphasize that, the paired micromodels MM5-Si and MM5-glass, and, MM4-Si and MM4-glass, have the identical microstructure MM5 and MM4 respectively (shown in Fig.3.1), but different inner surface roughness. All the micromodels have three sides sealed and one side left as open surface.

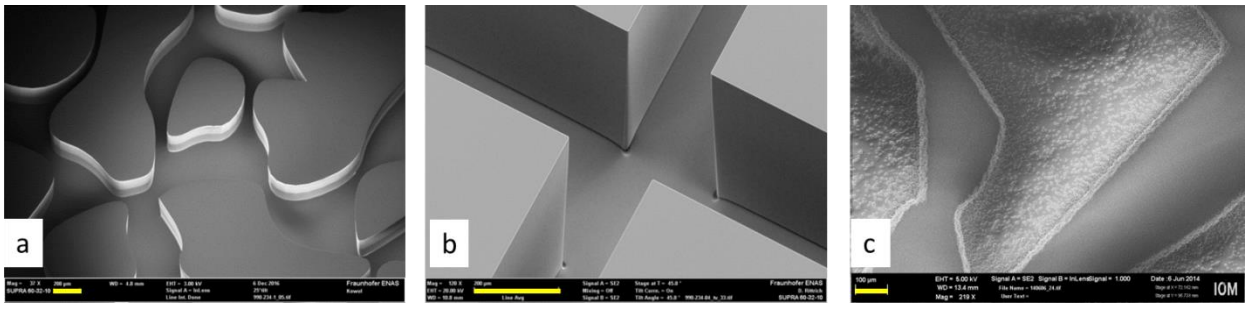

Figure 3. 2 SEM images of micromodels with different materials: absolute smooth surface and high edge steepness of (a) irregular micromodel MM4-Si (scalebar = 200 μm) and (b) quadratic lattice micromodel MM5-Si (scalebar = 200 μm); (c) rough surface of MM4-glass (scalebar = 100 μm).

3.2 Contact Angle Measurements of the Experimental Fluids

3.2.1 Contact Angle Measurement of Deionized Water

The main experimental fluid was deionized water. The corresponding temperature-dependent physico-chemical propeties, i.e vapor pressure, surface tension, kinematic viscosity are displayed in Appendix I. Contact angle measurement of deionized water on the Si-SiO_2 wafers (which holds the identical surface properties as the applied silicon micromodels) and borofloat cover glasses was conducted by the Drop Shape Analyzer Krüss DSA 100. All wafers were sealed by protection membranes before measurement to avoid contamination. Once the wafer was positioned horizontally, one deionized water droplet should be extruded manually out of the water storage vessel and fell onto the wafer. After adjustment for a sharp and horizontal view, a baseline was set manually as wafer-air interface. The DSA 100 Analyzer detected the droplet surface and fitted with a complete ellipse, consequently, the two tangent lines of the ellipse at the three phase interface gave a contact angle at each side (Fig. 3.3).

The contact angle measurement results are listed in Appendix III. As a result, the mean contact angle for Si-SiO2 wafer is 48 ± 2° and for Borofloat cover glass is 23 ± 2°, which yields the effective contact angle of the silicon micromodel by a simple arithmetic averaging: (Si-SiO_2-corner + glass-corner)/2 = 35.5°.

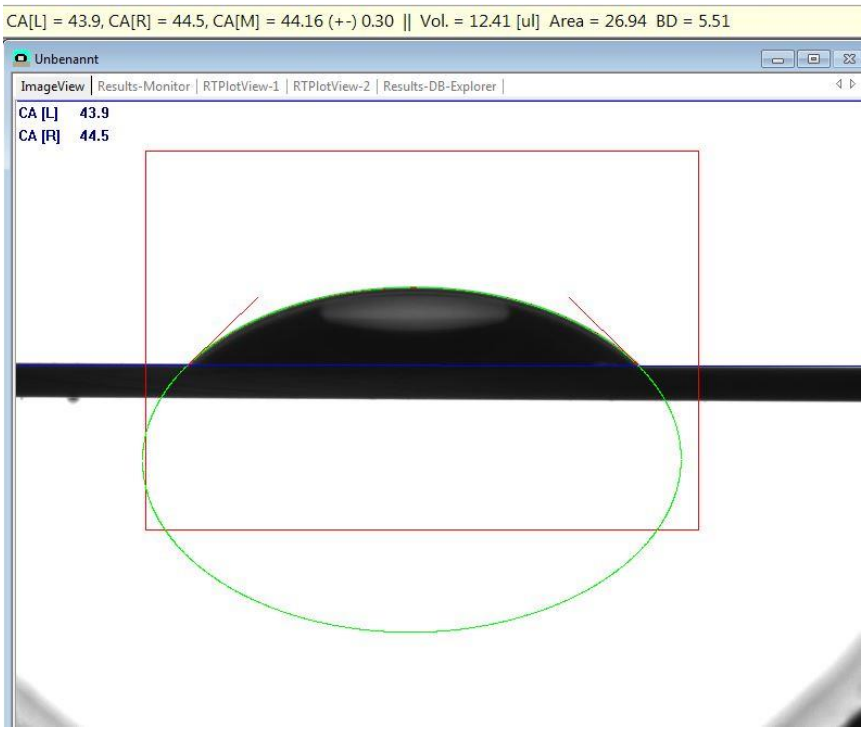

Figure 3. 3 The Drop Shape Analyzer measures the droplet surface and fits with a complete ellipse, the two tangent lines of the ellipse at the three phase interface give a contact angle at each side.

3.2.2 Contact Angle Measurement of Ethanol

I also applied ethanol in the room temperature experiments due to the volatility. The physico-chemical propeties of ethanol are displayed in Appendix I. Contact angle measurements with different ethanol concentrations (mixed with deionized water) were conducted. The images of the ethanol solution droplets on Si-SiO_2 wafers were analyzed by Fiji/ImageJ, where the plugin "contact angle" measures contact angle in the same principle of Drop Shape Analyzer Krüss DSA 100, that is, the droplet surface can be detected and fitted with a complete ellipse, then the tangent lines of the ellipse at the three phase interface give estimated contact angles. The measured contact angles have a nearly negative linear correlation to the ethanol concentration, pure ethanol is completely wetting on the untreated Si-SiO_2 wafers (Fig. 3.4). Note that, as the applied micromodels were performed for experiments with deionized water first, the water treatment has changed the wettability of Si-SiO_2 wafers for ethanol. The contact angle of pure ethanol on the water-treated Si-SiO_2 wafer is around 8.8° (Fig. A4 in Appendix III).

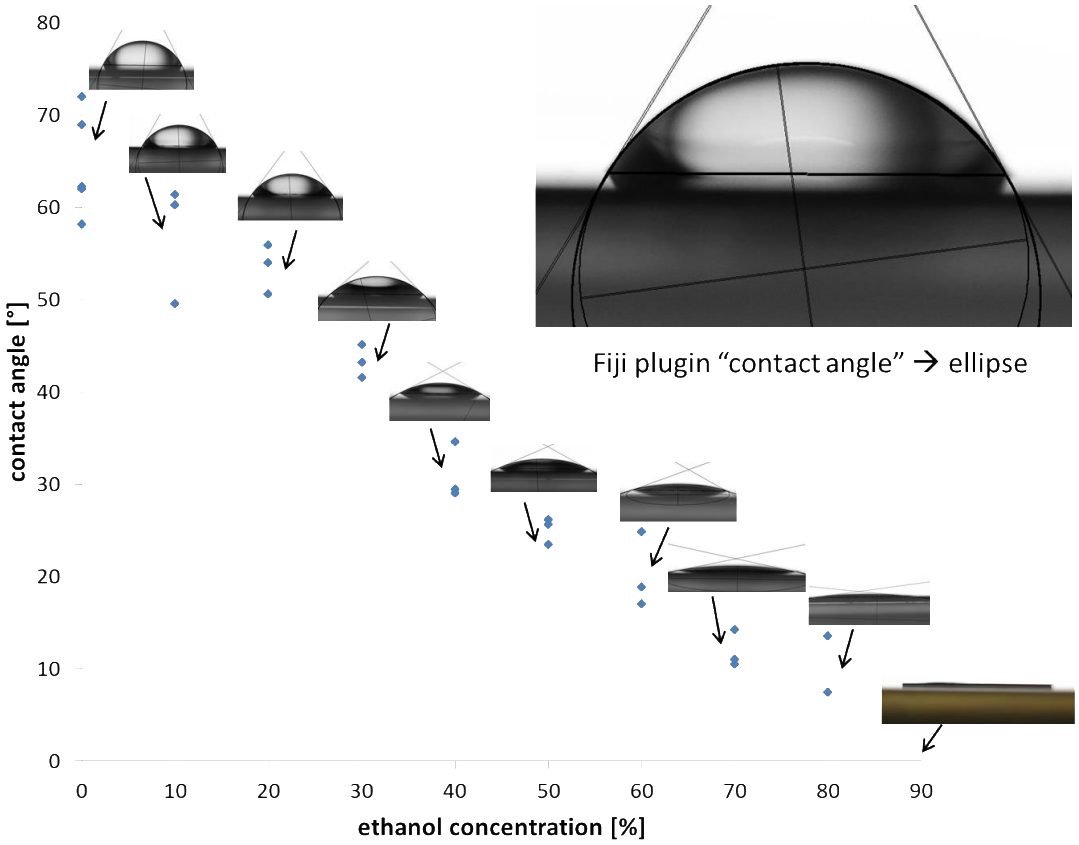

Figure 3. 4 The contact angle of ethanol on untreated Si-SiO_2 wafer has a nearly negative linear correlation to the ethanol concentration. Insert is the contact angle measurement by Fiji.

3.3 Methodology and Experimental Setup

3.3.1 Evaporation Experiment with Digital Balance and DSLR Camera

I conducted water evaporation experiments with all micromodels in the vertical direction (open surface on top; $B_0 > 0$) at three different temperatures: the room temperature (Experiment 1), 42°C (Experiment 2) and 61°C (Experiment 3). For the micromodels MM4-Si and MM5-Si, 1) additional water evaporation experiments were conducted in the horizontal direction ($B_0 = 0$; Experiment 4 in room temperature), 2) additional ethanol evaporation experiments were conducted in both vertical (Experiment 5) and horizontal (Experiment 6) directions (room temperature).

Prior to each experiment, the micromodels were saturated with deionized water/ethanol under vacuum for 2 hours with an evacuator. For the above-ambient temperature experiments, micromodels were mounted on a heating metal plate (meandering heaters at the backside) with a temperature controller attached to ensure a constant and uniform thermal field over the micromodel (Fig. 3.5). The supplied voltage to the heating plate and the micromodel surface temperature display a linear relation, so that a voltage supply of 7.8 v for experiment 2 and 11.8 v for experiment 3 (calibration see Appendix IV) were applied. The next, the surface temperatures at the top, down, left, right and center section of micromodel were measured respectively to obtain a mean surface temperature. As a result of 10 times measurements, the mean micromodel surface temperatures of experiment 2 and experiment 3 were determined as 42°C and 61°C respectively (Appendix IV). The evaporation process was continuously monitored by a high resolution digital single-lens reflex camera (Canon 5D Mark IV, lens: Canon EF 100mm F2.8L Marco IS USM) with a resolution of 6720 x 4480 pixels at time interval of 1 minute for early period (first 90 min) and 5min for later stage (till 4h). The total mass of the micromodel plus heating plate was continously measured by a high-precision digital balance (Sartorius Secura 1103-1S, $x \pm 0.001g$) and automatically recorded every 10 seconds by DasyLab software (version DasyLab 2016). The surface temperature was measured by an infrared-beam-device (Trotec BP25). The lab relative humidity and ambient temperature were recorded every 5-10 minutes by a data logger (dataTaker DT80 series2). To enhance the contrast of different fluidic phases, a circular cold lighting source was applied in front of the micromodel. Besides, a mini photographic studio was used to strengthen the illumination and to prevent air convection around micromodel.

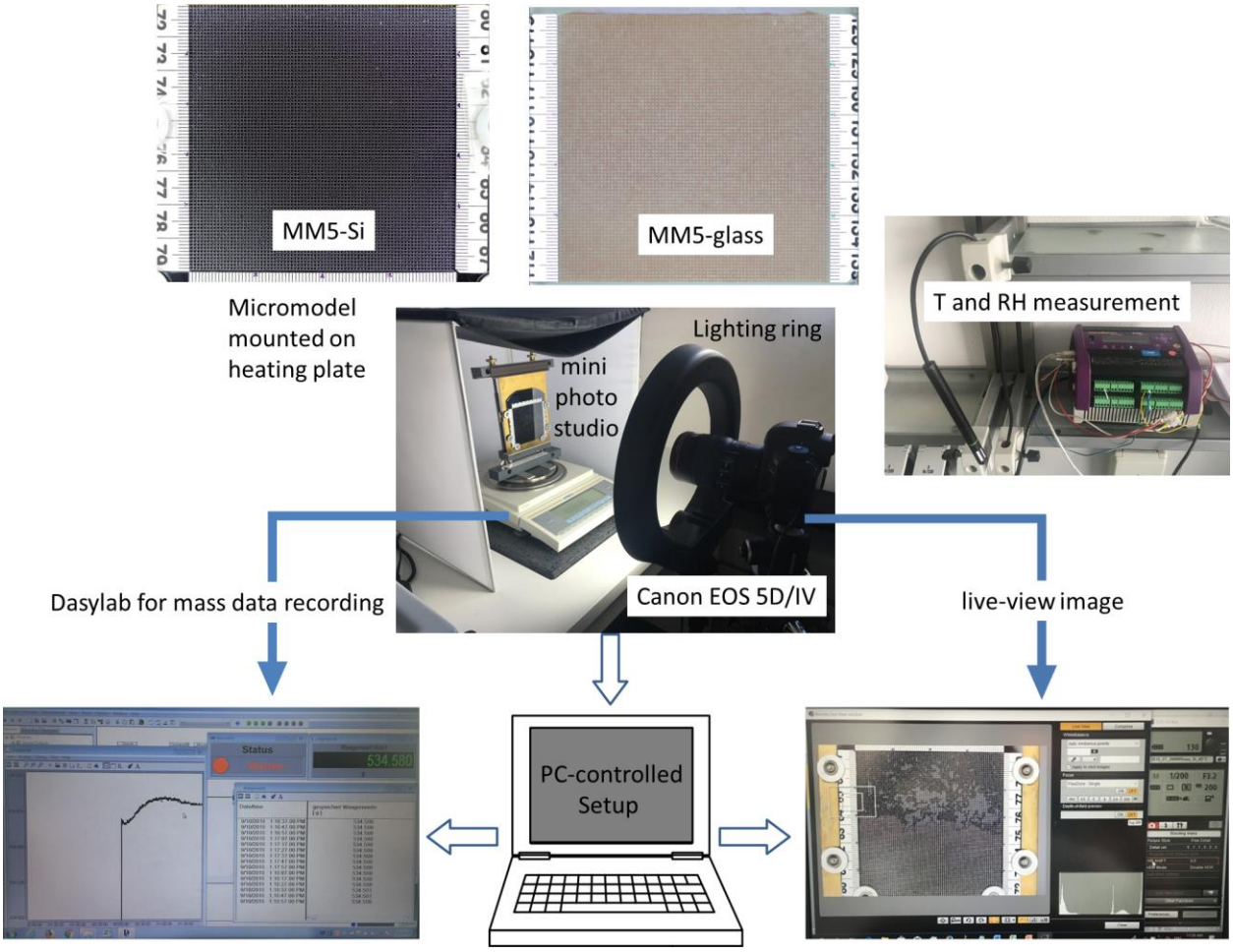

Figure 3. 5 Experiment setup with camera, digital balance, heating plate, temperature controller, miniphotographic studio, DasyLab Notebook data recording, and the data logger for relative humidity (RH) and temperature (T) measurements. The photos of micromodels MM5-Si and MM5-glass are displayed (Fig. 4; Ding & Geistlinger, 2021).

3.3.2 Evaporation Experiment with Fluorescence Microscopy

To better visualize the capillary flows during evaporation, horizontal experiments were conducted under a fluorescence microscope for each micromodel. I used Microscope Leica Leitz DMRB with objective lens of Nikon CFI Plan Apochromat Lambda 2X and 5X. Uranine was introduced as the fluorescent dye for water phase, that micromodels were saturated with 10% Uranine solution before experiments. A SLR camera (Canon EOS 7D, spatial resolution: 5184 x 3456 pixels) with a 100 mm Marco lens (Canon EF 100mm F2.8 USM Marco lens) and the LM Digital SLR adapter (LMscope C-Mount) were used for

visualization. After each experiment, micromodels were flushed with water for 10 times to remove the residual uranine dried at 60 °C for one week to obtain a reproducible initial condition.

3.4 Image Processing

The pore size distribution (PSD), gas-liquid phase segmentation and quantitative analysis were performed with Fiji/ImageJ (Schindelin et al., 2012).

3.4.1 Micromodel Pore Size Distribution

The PSD results were derived by the Fiji plugin "Local Thickness" (Dougherty & Kunzelmann, 2007), which inserts maximum-inscribed spheres (representing the pore size) into the pores. The PSD of MM4 is mainly in the range from 20 to 300 μm. The best fit curve for PSD of MM4 (normal distribution, blue curve in Fig. 3.6a) yields a mean pore radius of 205 μm with a standard deviation of 53 μm. The PSD of MM5 is mainly ranging from 100 to 300 μm. The best fit curve for PSD of MM5 (lognormal distribution, red curve in Fig. 3.6c) yields a mean pore radius of 197 μm with a standard deviation of 55 μm. The two pore structures have similar mean pore size while the irregular structure MM4 exhibits a broader PSD, especially, MM4 has a small peak in the small pore size zone (below 100 μm) because of the tiny pore throats (marked by white circles in Fig.3.6b).

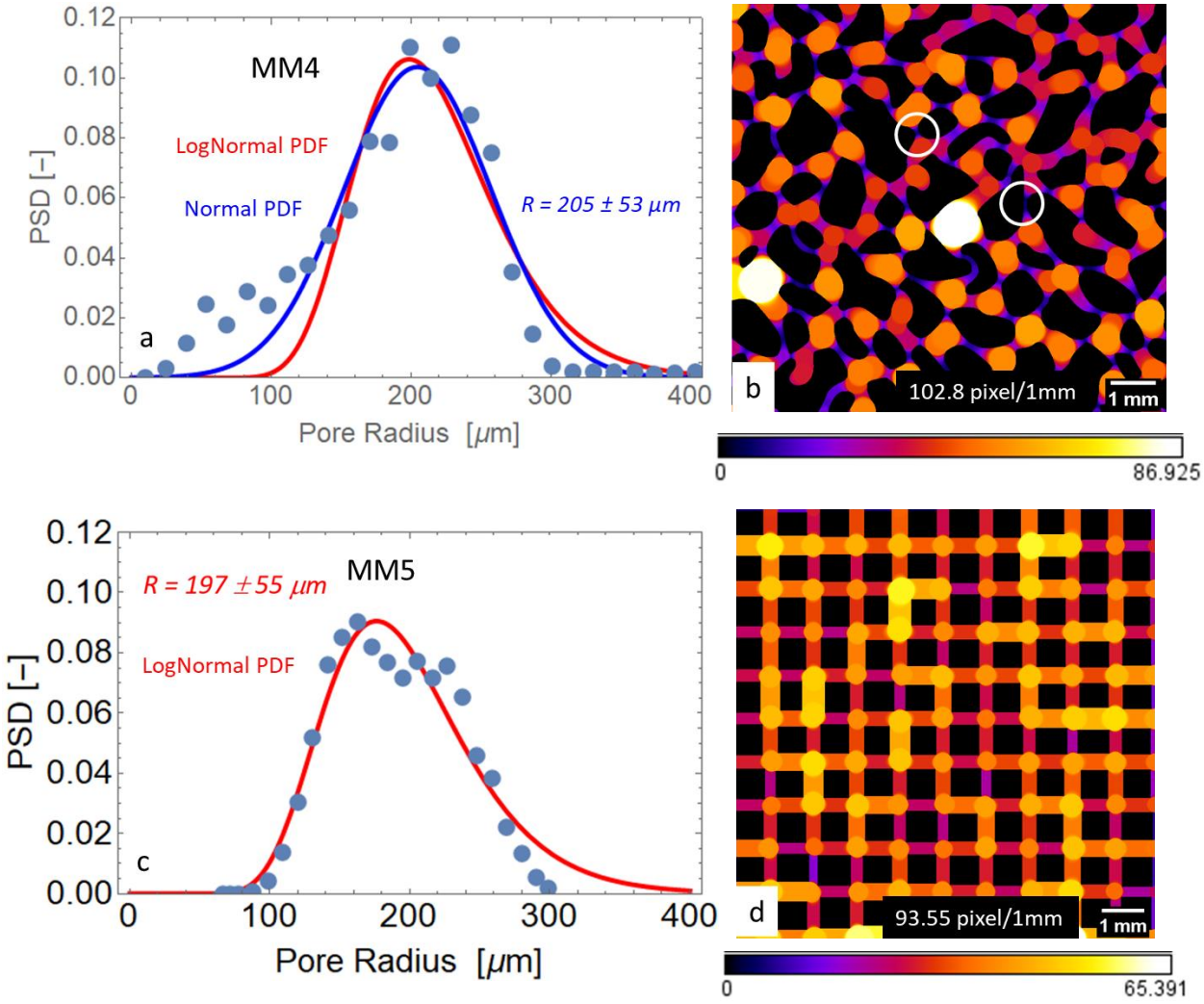

Figure 3. 6 (a) PSD of MM4 (blue dots) and the best fit (red curve is lognormal distribution; blue curve is normal distribution). (b) A spatial PSD for a partial section of MM4 derived by the "Local Thickness" method, the lookup tabel (LUT) shows the pore size in pixels, examples of tiny pore throats are marked by white circles. (c) PSD of MM5 (blue dots) and the best fit (red curve, lognormal distribution). (d) A spatial PSD for a 10 × 10 lattice section of MM5 derived by "Local Thickness" method (the LUT shows the pore sizes in pixels).

3.4.2 Gas-Liquid Phase Segmentation

Note that, all the processed images display the liquid filled pores in black, gas invaded pores and grain particles in white. Note that, the italic names in quotes in the following descriptions about IP workflow are the plugin or filter names in ImagJ.

Grain Mask Image Registration

As preprocessing, the grain mask image (applied in micromodel etching) must be registered onto the raw fluid pattern image. I performed semi-manual registration instead of using the plugins for automatic registration, because our micromodels have numerous microchannels and the similar pore structures at different sections can cause misplaced registration. The plugin "Big Warp" (Bogovic et al., 2016) was applied, where arbitrary landmarks can be selected on the mask image and fluid pattern image for deformable image alignment.

Liquid-Gas Segmentation for Silicon Micromodels

For the images of silicon micromodels, completely dry pores and liquid saturated pores are characterized by the bright edges of grain particles, because the lights irradiating at grain edges reflect back along the same way. While in the partially wet pores, the slope of corner flow eliminates this light artifact and presents dark edge. Thus, the grain perimeters' high gray value (black 0, white 255) are essential parameters for segmentation. The main steps in the workflow are introduced as below.

1. ***Small target windows selection*.** The fluid pattern image exhibites a radial illumination drift caused by the circular lighting source, it is difficult to choose a unique threshold value which applies to the whole image. Instead, I chose a certain section of the image which vertically includes the dry, saturated and the whole film regions, and horizontally covers the whole width of micromodel (see the yellow windows in the IP workflow below). I omitted the very bottom (saturated) and the very top (dry) section, where only a unique phase exists and no dynamic change is happening. The chosen section was further divided into five small windows so that each window can run a thresholding dependent on the local illumination condition. The image analysis eventually gives results of the whole micromodel.
2. ***Thresholding.*** The grey value thresholding was conducted with the green channel image after spliting the RGB channels. The purpose of thresholding is to largely reserve the complete grain edges in dry and liquid-saturated regions, while keeping the content of film region at minimum level. The initial

threshold value was generally set as 150 (gray value), which should be adjusted accordingly (in the range of $\pm$ 20) when any window doesn't show promising result.

3. ***Tubeness and second thresholding.*** A bubble phenonenon (see Appendix V) occurred during water evaporation experiments, that in the corner flow (CF) region some water accumulated as small bubbles and displayed bright reflections. The plugin "*Tubeness*" (Sato et al., 1998) produces a score for how "tube-like" each point in the image is, the straight grain edges are very like tube shape while the bubbles are less tube-like. After a second thresholding (gray value of 125) of the "*Tubeness*" image, the grain edges and very few discontinuous bubble edges can be extracted. Afterwards, the five windows were stitched back together and the remaining unwished bubble edges were eliminated by the filter "*Median*" and followed by the operation "*Area openin**g***" (to remove the tiny elements).
4. ***Maximum, Fill Holes and Minimum.*** The "*Maximum*" filter was applied to connect the discontinous boundaries of liquid clusters and liquid zone. After the "*Fill Holes*" and "*Minimum*" operations (scale to origional size), the liquid sections including internal grain area can be obtained.
5. ***Image Calculator, Multiply by the previous liquid zone image.*** By multiplying the previous binary image of liquid zone (gray values of liquid phase is 255, of dry phase and grain area are 0), the grains area and wrong liquid clusters were eliminated, forming a new liquid zone image which displayed only the liquid-filled pore channels. As a loop, this liquid zone image will be used for the image calculation of the next image.

Since MM4-Si has non-straight grain edges, the "*Tubeness*" detection is not sensitive. After thresholding (150) of the the green channel image (small window), the "*Median*" filter was able to eliminate the weak bubble edges and the rest part of the bubble circles were removed by size selection in the "*Area opening*" operation.

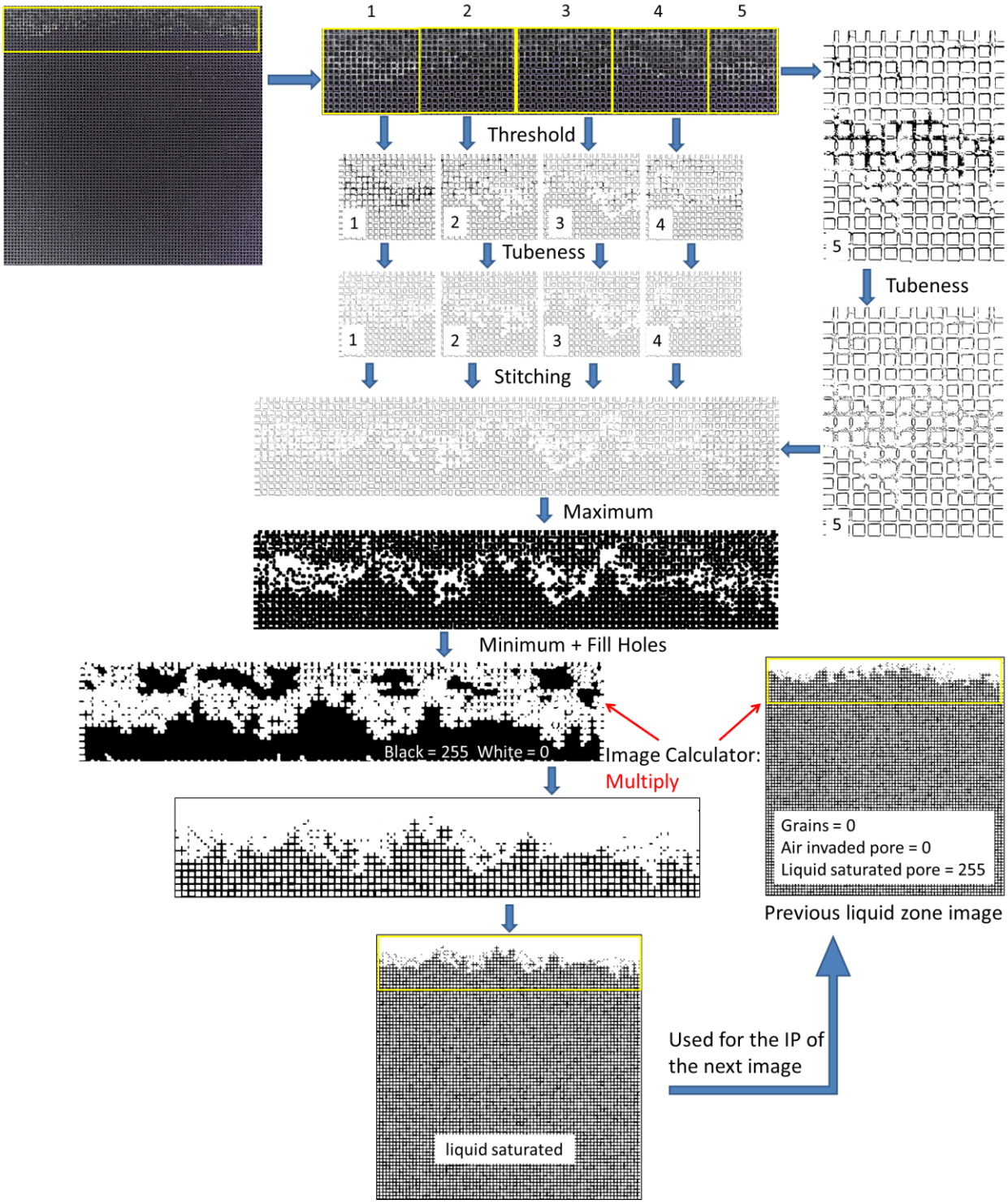

Figure 3. 7 Image processing workflow of MM5-Si (Fig. S8; Ding & Geistlinger, 2021).

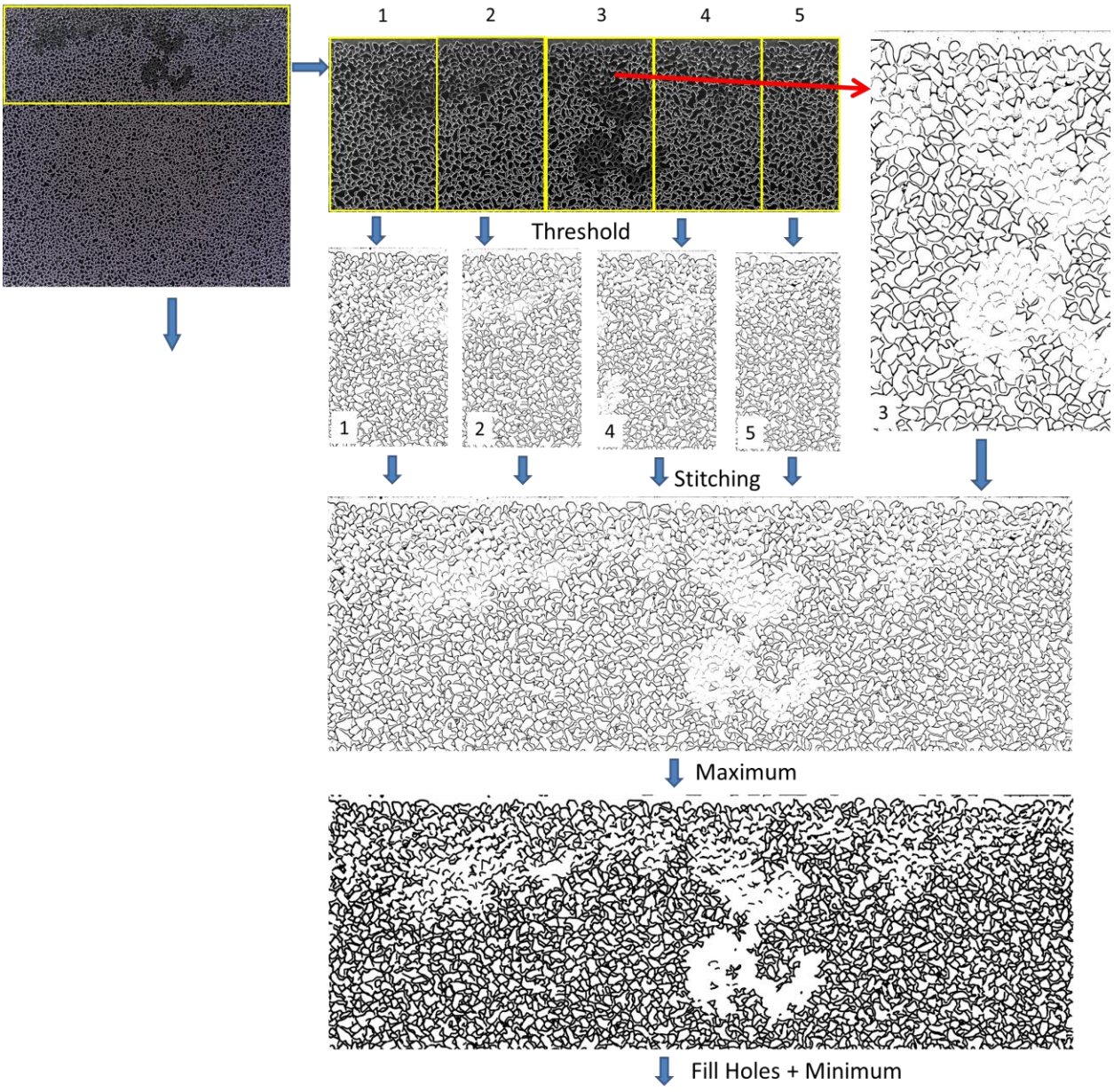

Figure 3. 8 Image processing workflow of MM4-Si (followed by next page).

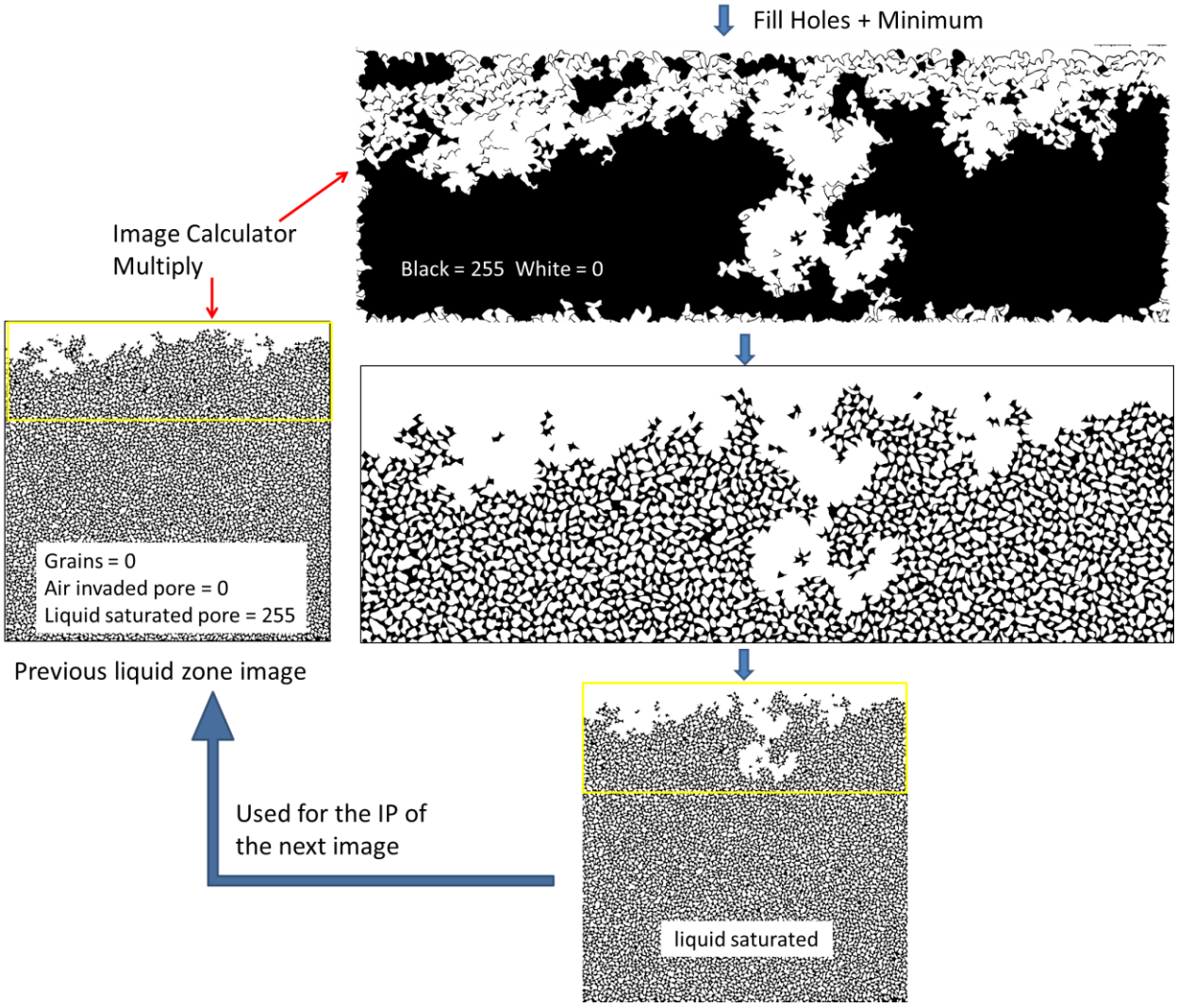
Fill Holes + Minimum
Black = 255 White = 0
Image Calculator
Multiply
Grains = 0
Air invaded pore = 0
Liquid saturated pore = 255
Previous liquid zone image
Used for the IP of
the next image
liquid saturated

Liquid-Gas Segmentation for Glass-Ceramic Micromodels

Due to the material property of the glass-ceramic micromodels, the completely dry pores present bluish background while the wet pores present brownish, white stripes were observed in the partial wet pores where corner flow and thick-film flow exist. The blue channel image was used for image processing. The main steps include:

1. ***Small target windows selection*.**
2. ***Thresholding.*** The initial thresholding gray value was generally set as 150, which should be adjusted accordingly (in the range of $\pm$ 20). The thresholding gave the gas-phase image including the completely dry pores (solid black), and the partial wet pores (which have inhomogeneous gray value distributions, only the white stripes were captured).
3. ***Maximum and Subtract noise.*** The white stripes were connected by filter "*Maximum*", the rest isolated tiny spots were considered as noise. By "*Analyze Particles*" operation with "*Exclude on edges*", the noise spots were extracted and further subtracted from the gas-phase image.
4. ***Invert, Multiple by previous liquid zone image.*** "*Invert*" the gas-phase binary image, air-invaded pores were given by 0 and white area was in 255. By multiplying the previous liquid zone image, the new air-invaded pores got mostly removed from the liquid region (see the red circle area in Fig. 3.9).
5. ***Minimum, Area Opening, Maximum.*** Disconnected and eliminated the residual parts of the new air-invaded pores by the "*Minimum*" and "*Area Opeing*" operations. Then resume the liquid saturated pores to initial size by the filter "*Maximum*" with the same radius as the previous "*Minimum*" operation.

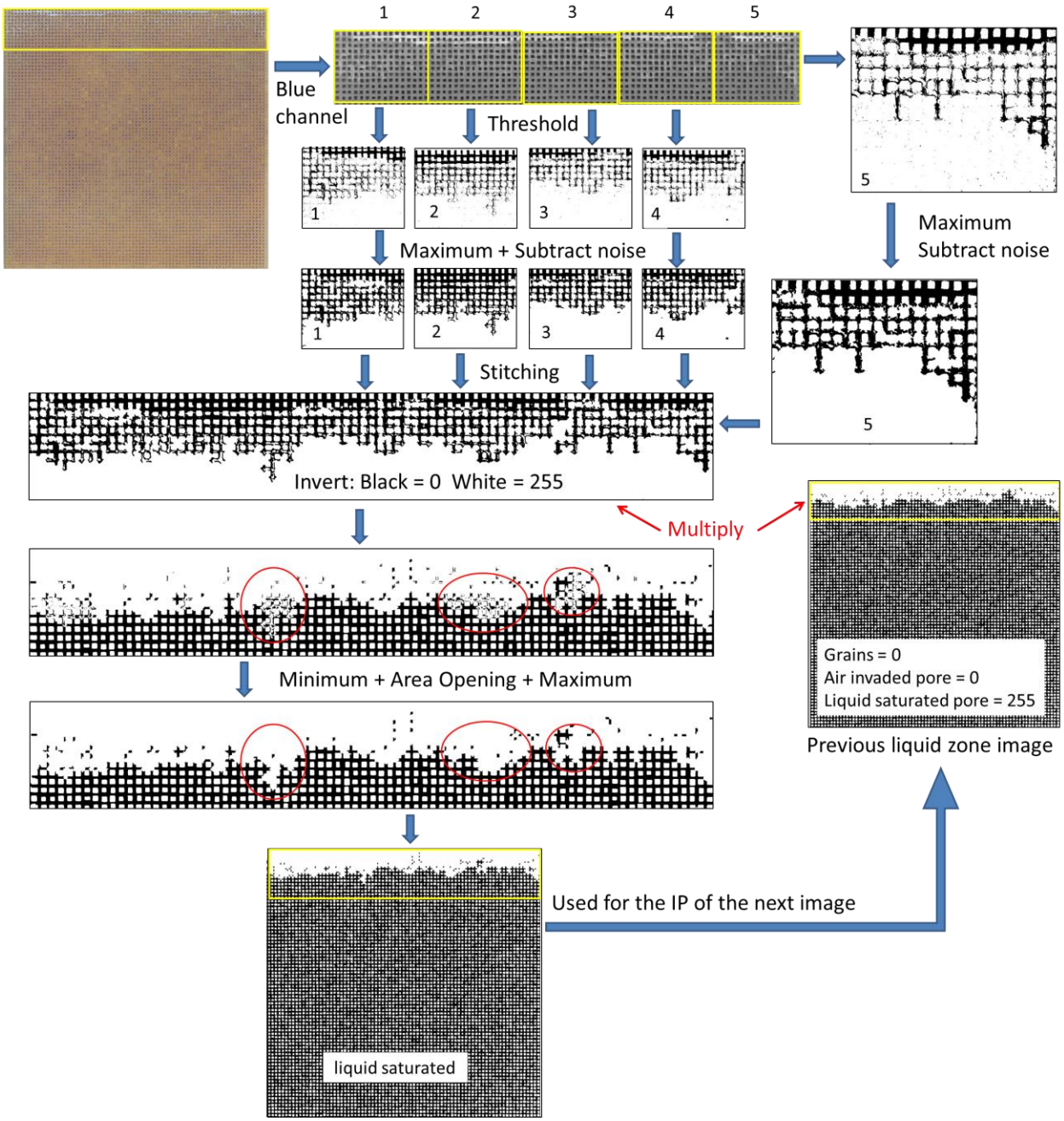

Figure 3. 9 Image processing workflow of MM5-glass (Fig. S9; Ding & Geistlinger, 2021).

3.4.3 Quantitative Analysis

Liquid Saturation

The residual water saturation S_w was derived by calculating the ratio: the total pixels of water-saturated phase (from the processed image) over the total pore space pixels (from the mask image). The evaporative mass loss Δm can be derived by

$$\Delta m = M_0 * (1 - S_w),$$

where M_0 is the total water capacity of micromodel.

Evaporation and Percolation Front Depth

The evaporation front is given by the upper boundary of the whole wet region (including the saturated region and CF/TFF region), the percolation front is given by the upper boundary of the saturated region. Knowing the Y coordinate of each pixel on the evaporation/percolation front, the mean evaporation (x_i) /percolation (x_p) front depth can be derived (Fig. 3.10d). The CF/TFF extension *w(t)* (green line in Fig. 3.10d) is given by the distance between the two averaged fronts.

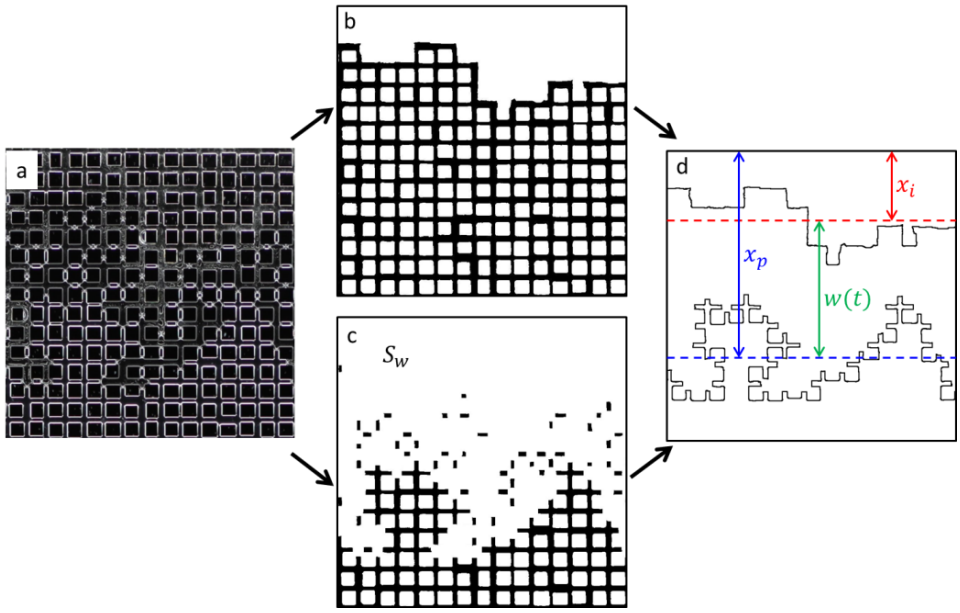

Figure 3. 10 The processed image gives the evaporation (x_i) / percolation (x_p) front depth. (a) A 15 x 15 lattice section of the raw image of MM5-Si water evaporation experiment (61°C, t=240 min). (b) The

processed image of the whole wet region of Fig. 3.10a including bulk flow and corner flow sections. (c) The processed image of the saturated region of Fig. 3.10a. (d) The averaging evaporation (x_i) and percolation (x_p) fronts give the corner flow extension *w(t)*.

Detachment Determination

When the evaporation front drops below the first layer of grains, no more hydraulic connectivity reaches the open surface through corner or thick-film flow, this liquid detachment is defined as the end of stage 1. The particle heights of the first layer of grains (marked in green in Fig. 3.11a and b) can be derived by the "*Analyze Particles*" with "*Bounding Rectangle*" analysis in ImageJ. Stage 2 starts when the evaporation front drops below the mean height of the first layer grains h_0 (yellow dashed lines in Fig. 3.11a and b), and the corresponding time is given as the detachment time t_c. MM4 was constructed with an artificial boundary layer (BL) above the porous media, where evaporation in this section is given as the pre-drying Stage 0. Due to the highest capillary pressure resistance at the pore throats, the equivalent initial water table of Stage 1 is at the pore throats of the first layer grains (white curve in Fig. 3.11b), with an averaged depth of h_{BL}. Therefore, the measured evaporation and percolation front depths need to be subtracted by h_{BL} to achieve the realistic data.

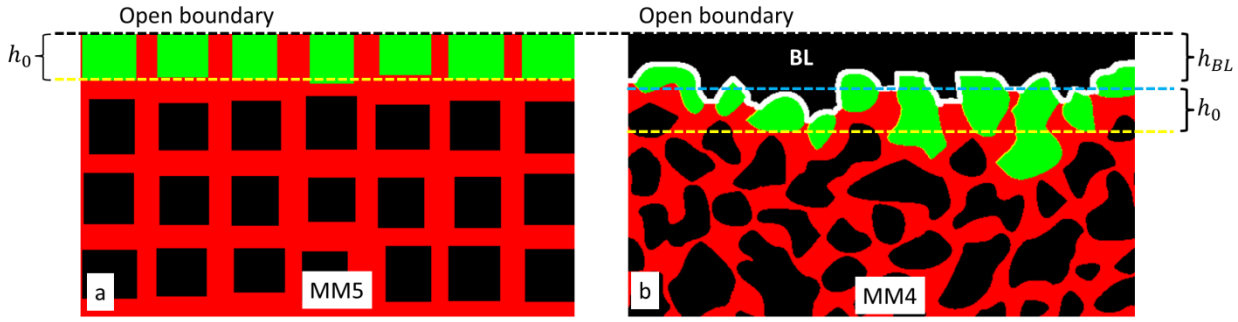

Figure 3. 11 Stage 2 starts when the evaporation front drops below the mean height of the first layer grains h_0 (yellow dashed lines). (a) The average height h_0 of the first layer grains in MM5 (marked in green). (b)The equivalent initial water table (white line) of Stage 1 in MM4 with an averaged depth of h_{BL}.

4 Experimental Results and Discussion

4.1 Corner and Thick-film Flow Visualization in a Pore Channel during Evaporation

The time-sequence images in Fig. 4.1 a-d show the CF development in a MM5-Si pore channel during experiment 3 (61°C). The water phase seeded with uranine is shown in green, while the dry pore and solid grain particles are dark. The fluorescence intensity directly reflects the water thickness. During evaporation, the pore with largest radius and least capillary resistance is first invaded by air. The bulk flow (BF) meniscus recedes into pore channel with a stable curvature. Some water is retained in the grains corners (CF) with thickness gradually decreasing from BF meniscus to the pore channel end (see Movie S1 in Ding & Geistlinger, 2021). The water pressure gradient: $P_{w,BF} > P_{w,CF}$ drives water transport from BF towards the dry region through CF. The white arrows in Fig. 4.1 b-d display CF extending longer during evaporation (as shown in Fig. 2.11c). Similarly, the time sequence images in Fig. 4.1 e-h show the same CF development in the pore channel of MM5-glass (experiment 3; 61°C), whereas the pore space invaded by air shows a light green film (TFF) instead of dark as in MM5-Si (see Movie S2 in Ding & Geistlinger, 2021).

Due to the water pressure gradient: $P_{w,BF} > P_{w,CF} > P_{w,TFF}$, the disappearance order of "bulk flow – corner flow – thick-film flow" was captured in the time sequence images in Fig. 4.1 i-l (see Movie S3 in Ding & Geistlinger, 2021). Water-filled pores are not invaded by air layer by layer, because of the random pore sizes. Hence, bypass air invasion often occurs, and air invades the pore channel from both sides until a liquid bridge (LB) is left, connecting the neighboring grains. In this case, CF and TFF at both sides flow away from the liquid bridge (Fig. 4.1j). BF dried first, leaving the last water as a liquid bridge (Fig. 4.1j). In Fig. 4.1k, TFF and weak CF are still visible after liquid bridge disappears; CF and TFF must flow towards the left, where the open surface is located. The flow direction is implied by the thickness gradient of the CF and the TFF uranine intensity difference. In Fig. 4.1l, the CF at the lower grain particle has already dried out, but a weak TFF can still be seen. Eventually, the pore dried out and became dark.

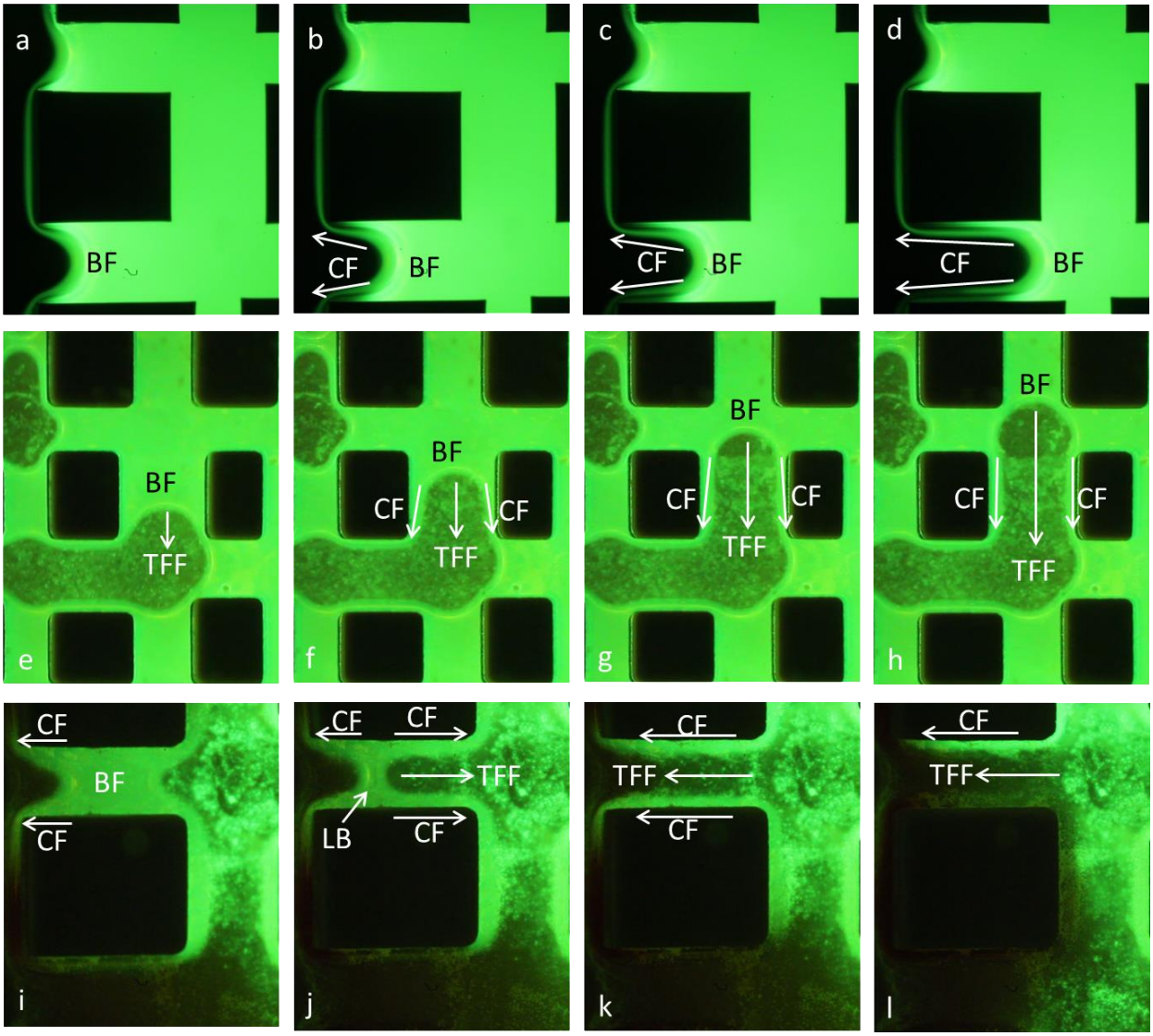

Figure 4. 1 (a) – (d) Time sequence images of corner flow (CF) development in MM5-Si (uranine tracer, fluorescence microscopy); (e) – (h) time sequence images of corner flow and thick-film flow (TFF) development in MM5-glass; (i) – (l) time sequence images of the disappearance order "bulk flow – corner flow – thick-film flow" in MM5-glass (Fig. 8; Ding & Geistlinger, 2021).

4.2 Spatial Patterns of the Corner/Thick-film Flow in Micromodels

MM5-Si

Figure 4.2a shows a typical spatial pattern of the CF region bounded by the evaporation (yellow) and percolation (cyan) fronts in MM5-Si during stage 2 (t = 240 min, 61 °C). In Fig. 4.2b (enlarged red window in Fig. 4.2a), the completely dry region and water-saturated BF region can be recognized by the bright rings circling grain particles. These rings occur because light irradiating at the grain edges reflects back along the initial direction, which is the same for the isolated water cluster with small bright ring in the CF region (red arrow in Fig. 4.2b). In the partial wet pores, the CF slope eliminates this light artifact, presenting a dark edge. Figure 4.2c shows the same section as Fig. 4.2b after image processing with a more straightforward segmentation; the BF region and isolated clusters are marked in blue, the dry region is marked in yellow, and the partial wet pores are marked in green, with CF and liquid bridge marked in red. The isolated single-channel or multichannel water clusters force CF to flow along a highly tortuous path from the percolation front towards the evaporation front (dashed blue line in Fig. 4.2d) until the water clusters dry up and only a liquid bridge remains. The liquid bridge allows the CF to pass from one grain particle to the neighboring particle.

MM5-glass

Figure 4.3a shows a typical spatial pattern of the film region of MM5-glass during stage 2 (t = 239 min, 61 °C). The film region, including both CF and TFF, is bounded by the evaporation (yellow) and percolation (cyan) fronts. The film region in MM5-glass displays a larger extension than the CF region in MM5-Si. In Fig. 4.3b (magnified red window in Fig. 4.3a), the completely dry region can be recognized by bluish pore channels, while the pore channel displays a brownish color when the inner surface is wet. As TFF flow has a smaller curvature radius than CF, BF can supply a TFF path longer than the CF length. Therefore, CF close to the evaporation front (TFF front) is rather weak and no longer directly connected with BF, but is maintained in the form of a liquid ring (LR) surrounding the grain particles (Fig. 4.3d). Liquid rings are indicated by white circles in the original experimental image in Fig. 4.3b and marked in red in the processed image in Fig. 4.3c. The liquid ring can be either isolated or connected with few neighboring grain particles by liquid bridges; eventually, the liquid-ring water is transported from the corners towards TFF as evaporation supply.

The film region presents a whitish color caused by light reflection (see Fig. 4.3e). The processed image in Fig. 4.3f shows that the corner flow near the percolation front is mostly connected with bulk flow or isolated water clusters. With sufficient water supply from the bulk flow and isolated water clusters, the corner flow near the percolation front is thicker (Fig. 4.3g) compared to the retained liquid rings near the evaporation front which have no water supply (Fig. 4.3d).

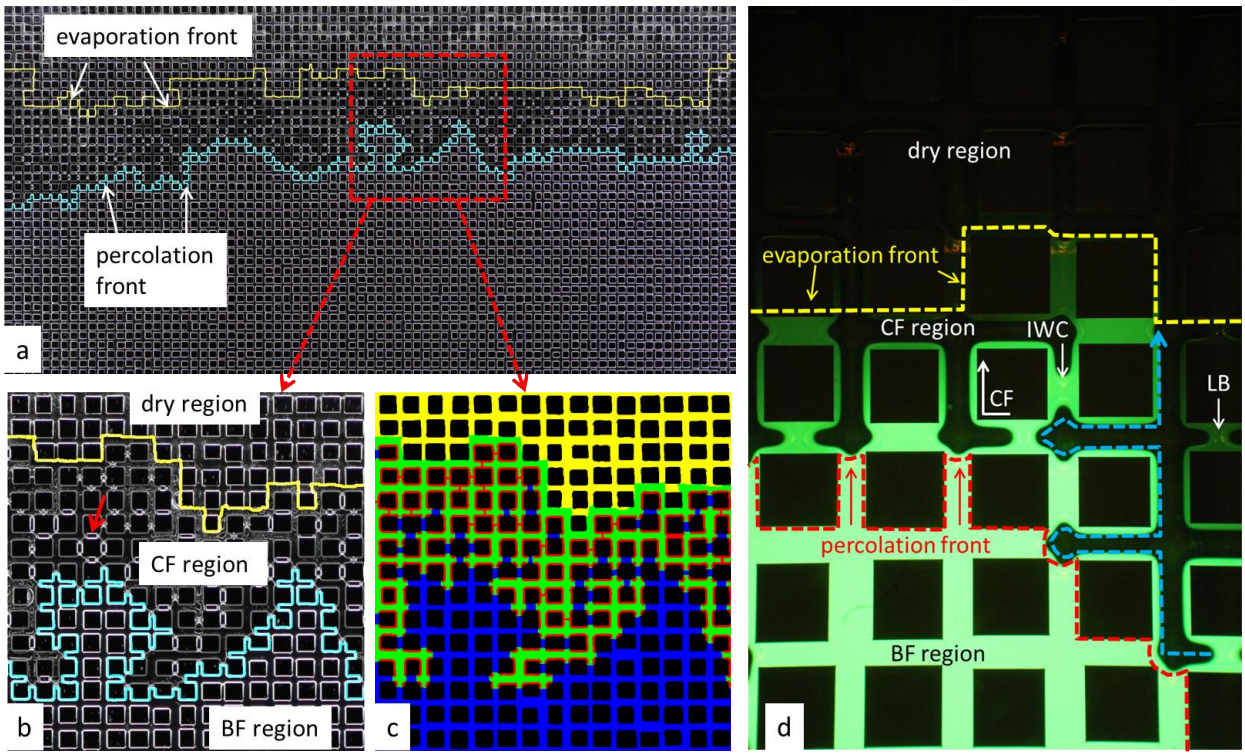

Figure 4. 2 (a) Spatial stochastic pattern of the corner flow (CF) region bounded by the evaporation (yellow) and percolation (cyan) fronts in MM5-Si during stage 2 (t = 240 min; 61 °C); (b) magnified red window of Fig. 4.2a; (c) window of Fig. 4.2b after image processing, where the bulk flow (BF) region and isolated water clusters are marked in blue, the dry region is marked in yellow, the corner flow region is marked in green, and corner flow and liquid bridges are specifically marked in red; and (d) fluorescence microscopy image of MM5-Si during stage 2 (61 °C) showing all three regions, the isolated water clusters (IWC) and a highly tortuous corner flow path (dashed blue line; Fig. 9 in Ding & Geistlinger, 2021).

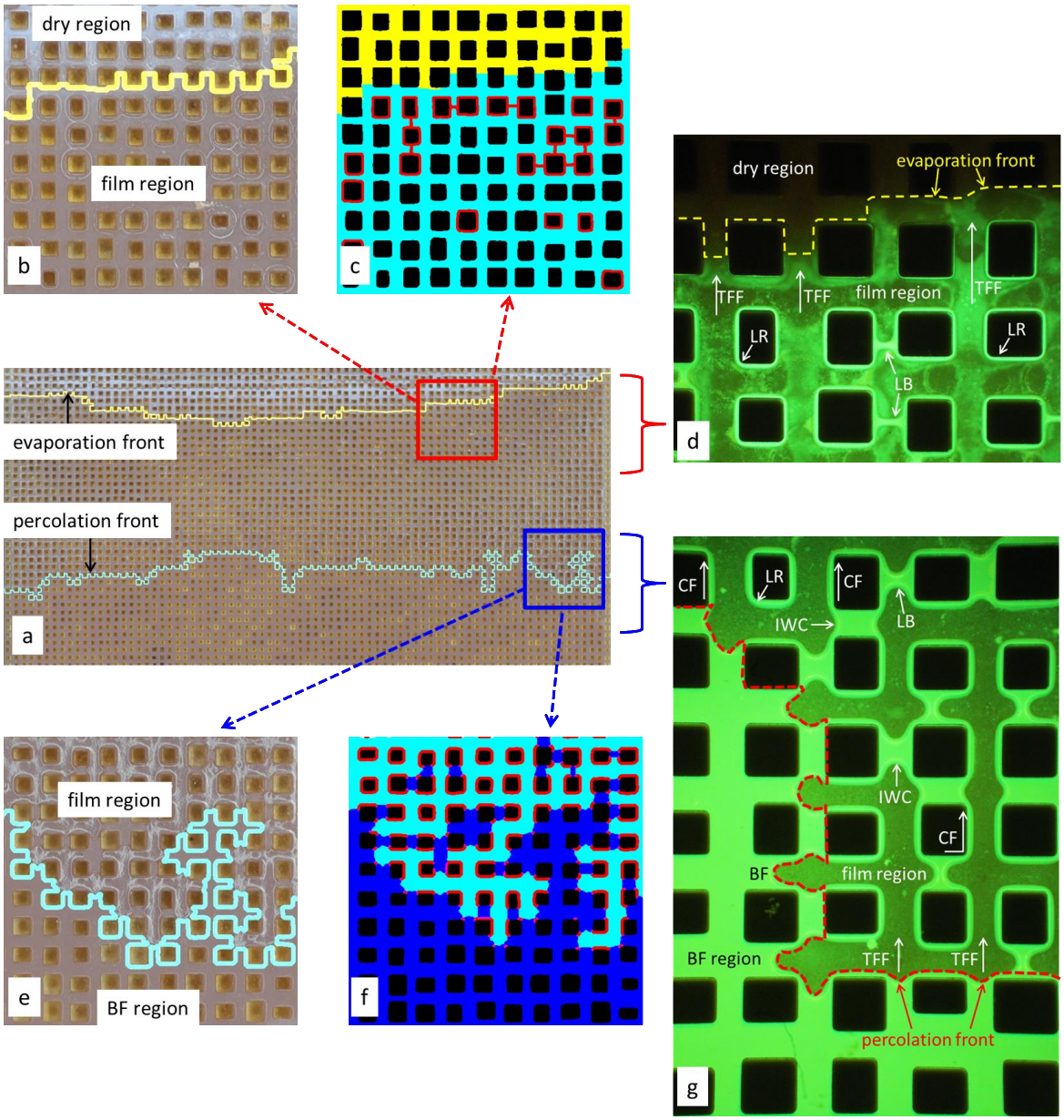

Figure 4. 3 (a) Spatial stochastic pattern of the film region bounded by the evaporation front (yellow) and percolation (cyan) fronts in MM5-glass during stage 2 (t = 239 min; 61 °C); (b) magnified red window of Fig. 4.3a; (c) window of Fig. 4.3b after image processing, where the dry region is marked in yellow, the film region is marked in cyan, and corner flow and liquid bridge are marked in red; (d) fluorescence microscopy image of MM5-glass (61 °C) during stage 2 showing the dry region and film region; (e) magnified blue window of Fig. 4.3a; (f) window of Fig. 4.3e after image processing, where the bulk flow (BF) region and isolated water clusters are marked in blue, and corner flow is marked in red; and (g) fluorescence microscopy image of MM5-glass (61 °C) during stage 2 showing the film and bulk flow regions and isolated water cluster (IWC; Fig. 10 in Ding & Geistlinger, 2021).

MM4-Si

Figure 4.4a shows a typical spatial pattern of the CF region bounded by the evaporation (yellow) and percolation (cyan) fronts in MM4-Si during stage 2 (t = 240 min; 61 °C). Similar to MM5-Si, the completely dry region and liquid-saturated BF region are characterized by the bright rings which circle the grain particles, the partial wet pores with CF present dark edges (Fig. 4.4b). Due to the irregular pore structure, MM4-Si displays more fluctuated and heterogeneous evaporation and percolation fronts than MM5-Si. The straight pore channels in MM5 do not exist in MM4. Instead, every two neighboring grains in MM4 form a pore throat (PT) in between (Fig. 4.4d). In Fig. 3.6a, the PSD of MM4 shows a small peak at around 50 μm, which indicates the peak of pore throat size distribution. As the tiny pore throat has high capillary resistance, water is always retained in the throat as liquid bridge (LB; Fig. 4.4d). The widely and abundantly distributed liquid bridges in pore throats form strong corner flow connectivity and promote the water transport. The isolated water cluster in MM4-Si can be relatively large composed of multiple pores (red arrow in Fig. 4.4b).

MM4-glass

Figure 4.5a shows a typical spatial pattern of the film region of MM4-glass during stage 2 (t = 241 min; 61 °C). The film region, including both CF and TFF, is bounded by the evaporation (yellow) and percolation (cyan) fronts. MM4-glass presents a highly fractal and heterogeneous percolation front, but a rather flat evaporation front because of the long extended TFF. Due to the large capillary resistance at pore throats, water can be kept in some pores near the evaporation front (the isolated water clusters marked by red arrow in Fig. 4.5c). This explains why water in the micropores in real soil profile is held tightly by capillary suction and hardly available for plants, while the macropores promote aeration, gas exchange, free water flow (which can transport dissolved nutrients and agrochemicals) and evaporation (Easton & Bock, 2016).

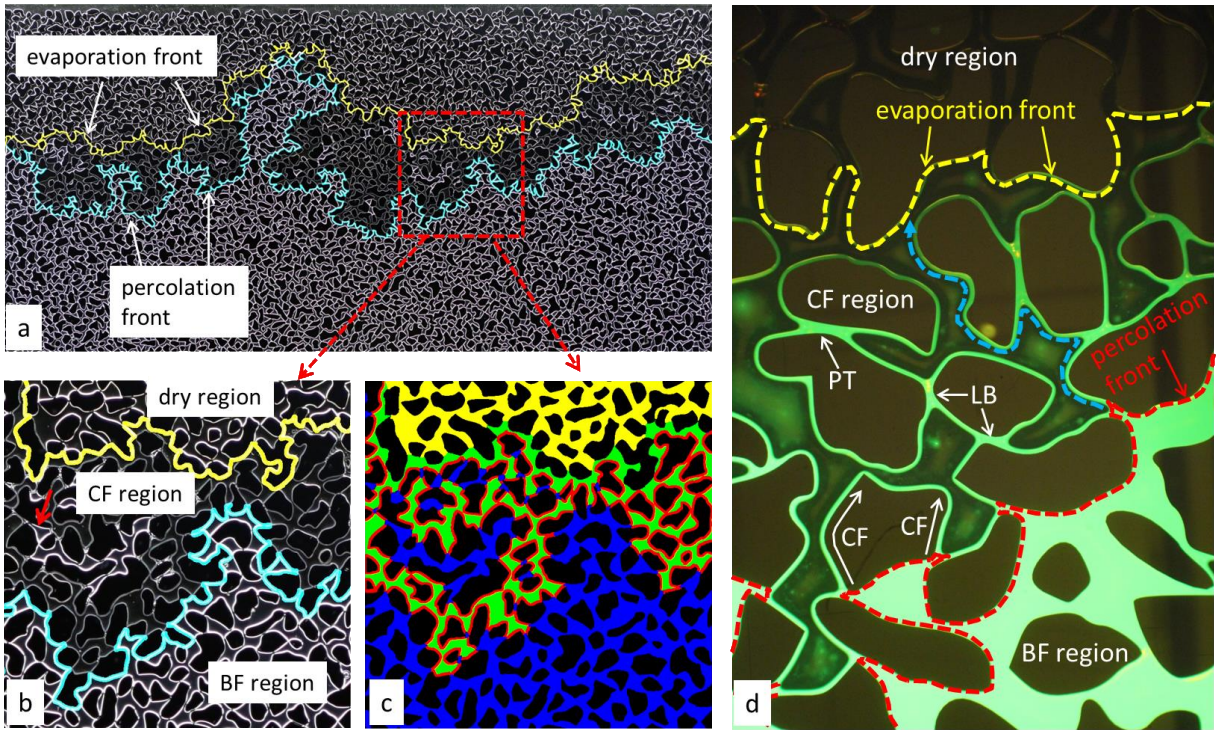

Figure 4. 4 (a) Spatial stochastic pattern of the corner flow (CF) region bounded by the evaporation (yellow) and percolation (cyan) fronts in MM4-Si during stage 2 (t = 240 min; 61 °C); (b) magnified red window of Fig. 4.4a; (c) window of Fig. 4.4b after image processing, where the bulk flow (BF) region and isolated water clusters are marked in blue, the dry region is marked in yellow, the corner flow (CF) region is marked in green, and corner flow and liquid bridge are specifically marked in red; and (d) fluorescence microscopy image of MM4-Si during stage 2 (61 °C) showing all three regions and a tortuous corner flow path (dashed blue line).

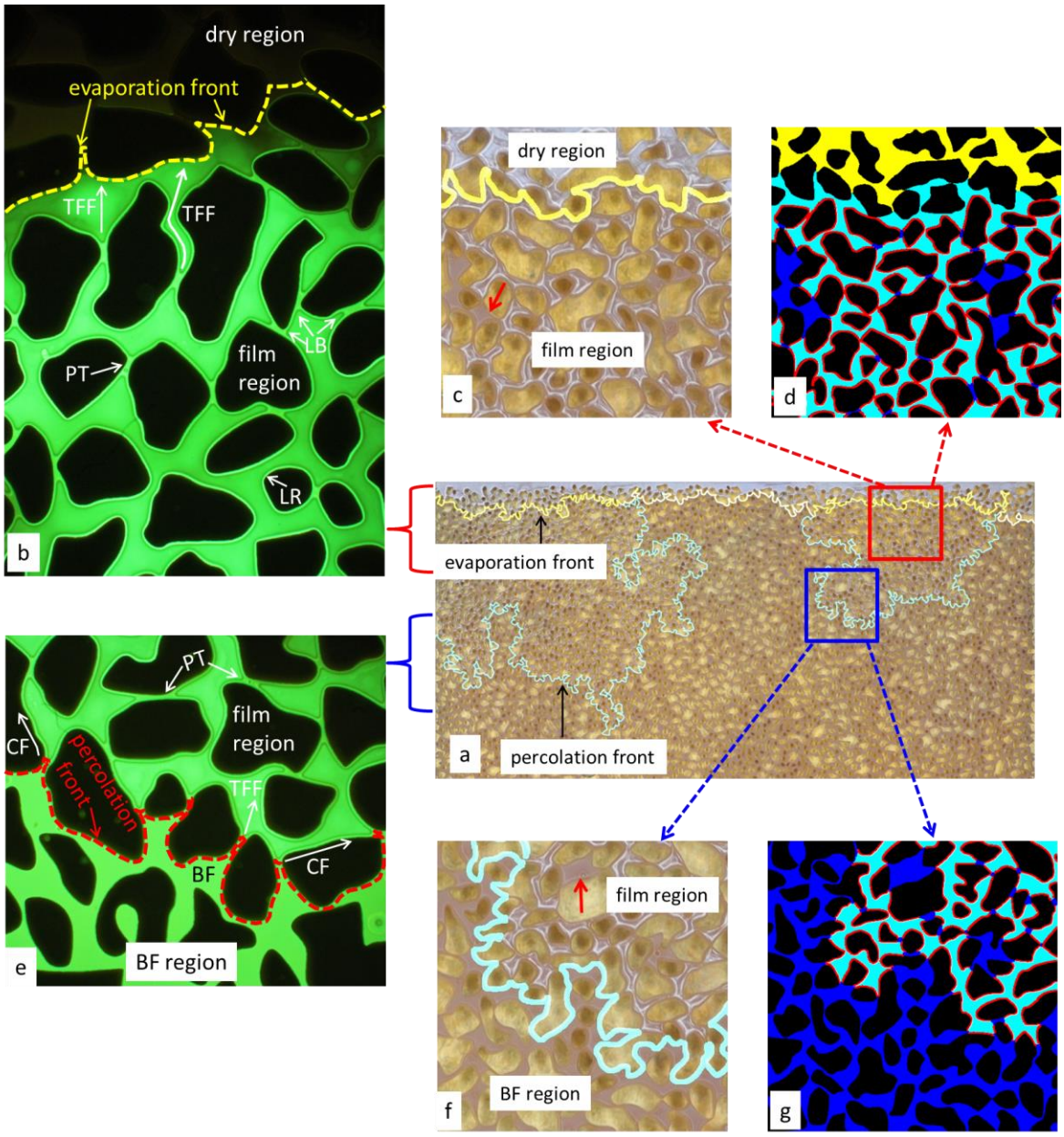

Figure 4. 5 (a) Spatial stochastic pattern of the film region bounded by the evaporation front (yellow) and percolation (cyan) fronts in MM4-glass during stage 2 (t = 241 min; 61 °C); (b) fluorescence microscopy image of MM4-glass (61 °C) during stage 2 showing the dry and film regions; (c) magnified red window of Fig. 4.5a; (d) window of Fig. 4.5c after image processing, where the dry region is marked in yellow, the film region is marked in cyan, isolated water clusters are marked in blue, corner flow and liquid bridge are marked in red; (e) fluorescence microscopy image of MM4-glass (61 °C) during stage 2 showing the film and bulk flow (BF) regions; (f) magnified blue window of Fig. 4.5a; (g) window of Fig. 4.5f after image processing, where the bulk flow region and isolated water cluster are marked in blue, corner flow is marked in red.

In summary, during the evaporation process, a pore channel may hold isolated water cluster after the neighboring pore channels are air-invaded, but the water cluster is still hydraulically connected to the BF region through corner flow. When the isolated-water-cluster pore is also invaded by air, the water cluster shrinks, and water is transported through CF (and TFF) until only a liquid bridge is left. The liquid bridge connects the neighboring grain particles and allows the CF supply from the BF region or other isolated water clusters to continue. In silicon micromodels, once a liquid bridge is broken, the residual CF becomes isolated as a liquid ring. The liquid ring dries out quickly without water supply, dragging the evaporation front away from the open surface. The extension of CF region is described by the viscous length L_{visc} (viscous dissipation), which will be discussed in the latter chapter. In glass micromodels, because of the water pressure gradient $P_{w,BF} > P_{w,CF} > P_{w,TFF}$, BF should supply a longer TFF path than CF. But the more essential reason why the TFF region displays such a large extension and sustains the evaporation front close to open surface, is the complete wetting caused by surface roughness, which will be discussed in the latter chapter.

Based on the visualizations, it is clear that the answer of the problem 6 listed in the Chapter 1 is, besides the capillary flow through pore ducts (bulk flow), corner flow and thick-film flow play an important role in the evaporation process, as they sustain the liquid flow above the bulk flow water tables (percolation front) and maintain a longer hydraulic continuity closer to open surface.

4.3 Impact of Surface Roughness on Evaporation Efficiency

Mass Loss and Evaporation Rate Curves of MM5-Si and MM5-glass

The water mass loss curves of MM5-Si and MM5-glass at three temperatures are shown in Fig. 4.6 with inserted experimental RH and ambient temperature figures. The experimental data are renormalized as the ratio of the real mass loss to the micromodel's total water capacity. Meanwhile, experimental data given by the digital balance are smoothed by the "moving average" method (Hyndman, 2011) with a block size of 9. We tested the accuracy by comparing the mass-loss datasets derived from digital balance and image processing (IP) for each experiment. The two data sets concurred, with relative errors between 1% and 11% (Table 4.1).

As the kinetic energy of a molecule is proportional to its temperature, with an increase in temperature, the surface molecules tend to move rapidly until some molecules escape into the atmosphere. Therefore, the evaporation flux is enhanced by higher temperatures (Fig. 4.6 a–c), and water flux is adapted to match the

increased evaporation rate. The detachment time t_c (end of stage 1) is defined when the averaged evaporation front recedes below the first layer of grains so that no CF climbs to the open surface along the grain edges (Fig. 3.11). The duration of stage 1 (t_c) decreases with increasing temperature as the evaporation rate Q_{ev} of stage 1 is larger in higher temperature and results in faster hydraulic detachment. The water transport in the micromodel cannot meet the significant demand of Q_{ev} at high temperatures (42 °C and 61 °C), causing a dramatic transition in the mass loss curves between stages 1 and 2. Figure 4.6d shows an example of the linear fit of the mass loss curve for stage 1 (green line), and the slope determines the Q_{ev} of stage 1 (as stage 1 is characterized by a constant Q_{ev}). The Q_{ev} of stage 2 can be derived from the slope of the time-dependent tangent line of the mass loss curve (Fig. 4.7; Appendix VI). Evaporation is dominated by water redistribution through "capillary pumping" in stage 1; therefore, the mass loss curves of the two micromodels overlap significantly in stage 1(Fig. 4.6).

Evaporation is enhanced by the TFF for two reasons. First, at the same temperature, after CF detaches from the open surface, TFF can still reach the open surface in MM5-glass, maintaining a constant evaporation rate Q_{ev} and prolonging stage 1 (Fig. 4.7). Meanwhile, MM5-Si enters stage 2 with a sharp decrease of the evaporation rate. Figure 4.8 shows the evaporation rate as function of cumulative mass loss (in the form of evaporative depth; evaporated mass divided by micromodel cross section). The transitions from stage 1 to stage 2 in MM5-Si occur consistently at different temperatures with the onsets of stage 2 at around 5mm depth (Fig. 4.8a). While the onsets of stage 2 in MM5-glass occur at a later stage, i.e. at the evaporation depth around 7 mm for RT and 61°C and 10 mm for 42°C (Fig. 4.8b). Stage 1 was prolonged the most in the room temperature experiment, where the TFF transport was sufficient to compensate for the CF transport loss for evaporation.

The second reason is that, in stage 2, the evaporation front in MM5-glass is close to the open surface (before BF is dried out), while the evaporation front in MM5-Si continually recedes from the open surface. Further explanations on evaporation front depth x_i in both micromodels are discussed in the next section. With a certain boundary layer thickness δ, the smaller x_i in MM5-glass causes a larger vapor concentration gradient for diffusion and, consequently, a higher evaporation rate Q_{ev} (Eqs. 2.2.11 & 2.2.12). Therefore, in stage 2, the Q_{ev} of MM5-glass is always greater than that of MM5-Si (Fig. 4.7), and the mass loss difference between the two micromodels increases with time. At 4 h, the mass loss was nearly doubled by the TFF in the 42 °C and 61 °C experiments.

Table 4. 1 Detachment time t_c, constant evaporation rate Q_{ev} of stage 1, and the relative error between the gravimetrical and IP-derived mass loss for the experiments of MM5-Si and MM5-glass.

	t_c $[min]$			Q_{ev} $[mg/min]$			relative error [%]		
	Exp.1 (RT)	Exp.2 (42° C)	Exp.3 (61° C)	Exp.1 (RT)	Exp.2 (42° C)	Exp.3 (61° C)	Exp.1 (RT)	Exp.2 (42° C)	Exp.3 (61° C)
MM5-Si	40	12	6	0.7	2.5	6.4	1	11	3
MM5-glass	60	25	7	0.7	2.6	7.5	9	6	9

Lower relative humidity can enhance evaporation through a higher vapor concentration gradient (Eq. 2.2.12); this influence is insignificant in high-temperature experiments (42 °C and 61 °C) but can be crucial in room temperature experiments. The two temperature curves in experiments 1 are similar, while the relative humidity (RH) curves diverge after 100 min (Fig. 4.6a), indicating that the enlarging RH gap of up to 7% is sensitive enough to increase Q_{ev} in MM5-Si and compensates for the mass loss difference between the two micromodels in stage 2.

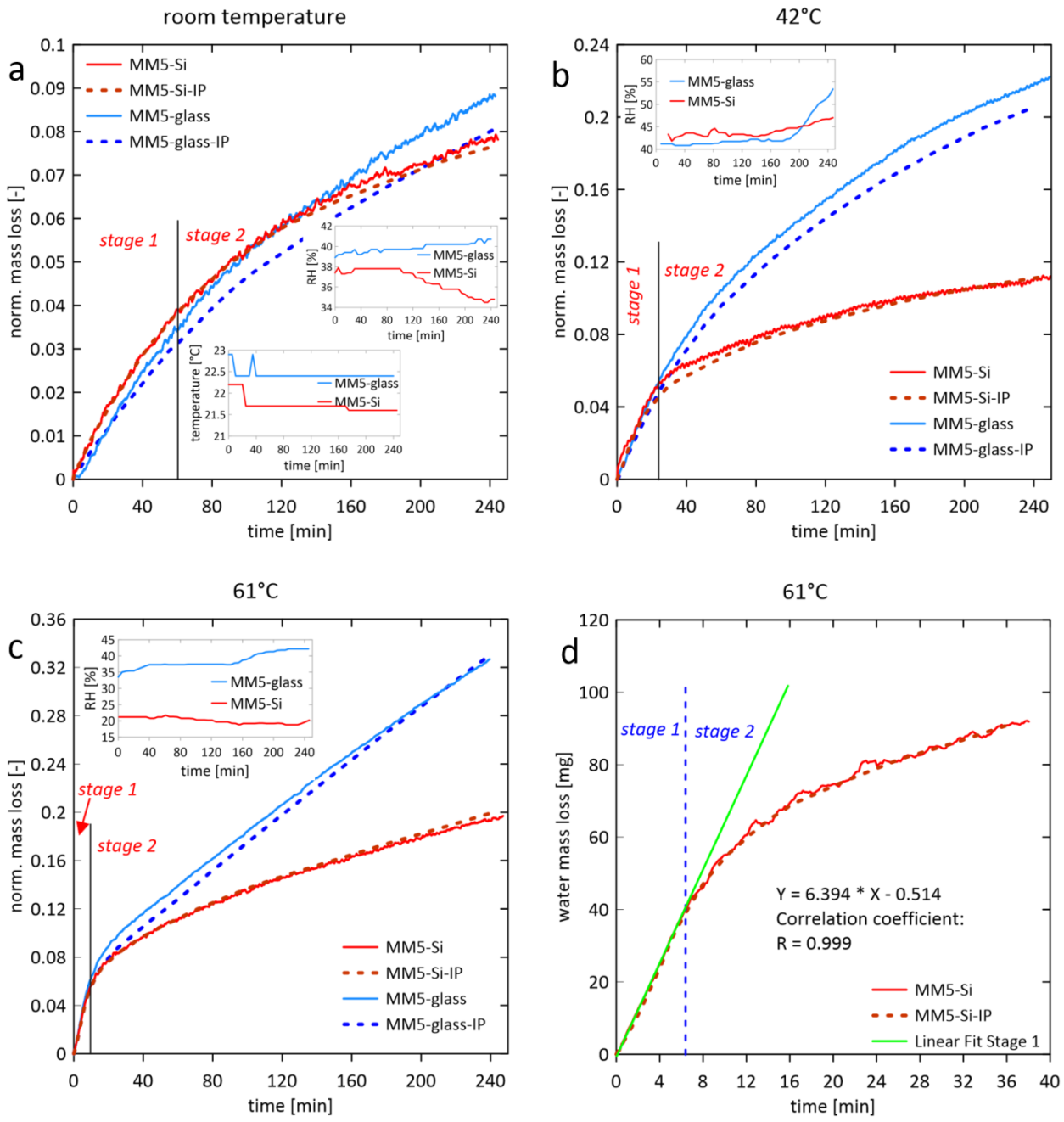

Figure 4. 6 Normalized time-dependent mass loss curves of MM5-Si and MM5-glass in (a) room temperature, (b) 42 °C, and (c) 61 °C. Mass loss data derived from digital balance measurements and image processing (IP) are indicated by solid and dashed colored lines, respectively. The insets show the ambient temperature (a) and relative humidity (RH, a - c) during the experiments. (d) Stage 1–stage 2 transition of experiment 3 (61°C), where stage 1 and stage 2 are divided by a dashed blue line. The equation describes the best linear fit curve (green line) for stage 1 (Fig. 11; Ding & Geistlinger, 2021).

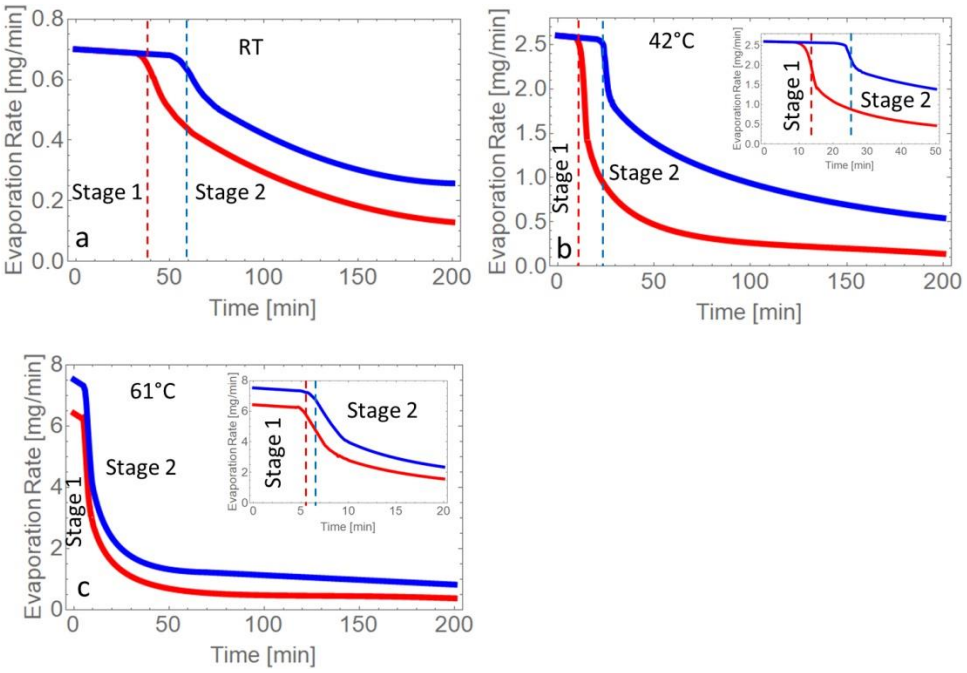

Figure 4. 7 Time-dependent evaporation rate curves of MM5-Si and MM5-glass at (a) RT, (b) 42 °C, and (c) 61 °C. The blue curves represent Q_{ev} of MM5-glass with the detachment time t_c marked by blue dashed lines. The red curves represent Q_{ev} of MM5-Si with t_c marked by red dashed lines. The insets show stage 1–stage 2 transitions (Fig. 12; Ding & Geistlinger, 2021).

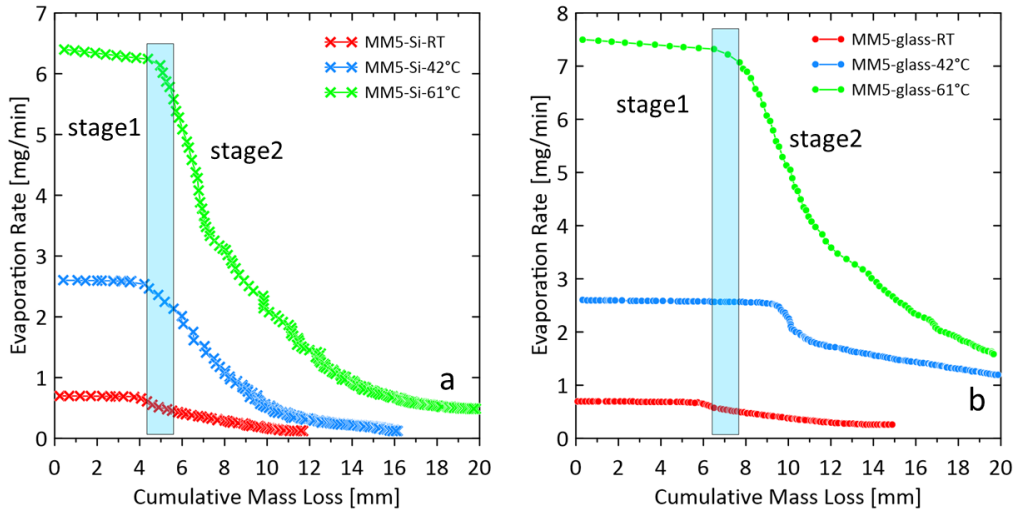

Figure 4. 8 Experimental evaporation rate of (a) MM5-Si and (b) MM5-glass as a function of cumulative mass loss (in the form of evaporative depth [mm]) under three temperatures (Figs. S1c & S2c; Ding & Geistlinger, 2021).

Geometric characteristics of the evaporation process

The percolation front depth x_p was derived by the geometric averaging of the front (Fig. 3.10). The x_p versus time (Fig. 4.9b) shows the same trend as the corresponding mass loss curve (Fig. 4.6): TFF in MM5-glass enhances evaporation, resulting in a larger x_p in MM5-glass than MM5-Si (at the same temperature).

In the pore network, a single pore channel is created by the grain walls and has a limited length based on the grain lengths. After BF in a pore channel vanishes, the water supply for longer CF is cut off from this pore channel, and CF is maintained by the BF from the adjacent or further pore channels by the liquid bridge. The liquid bridges near the evaporation front are vulnerable and can easily disappear owing to intensive evaporation. In MM5-Si, once the liquid bridge is broken, CF near the evaporation front loses hydraulic supply and will dry out instantly; thus, the evaporation front continues to recede along with the percolation front (Fig. 4.9a), and the CF region is maintained with a *relatively stable extension in stage 2* (Fig. 4.9c). In MM5-glass, TFF spontaneously carpets the rough inner surface and is independent of the liquid bridges. Before the BF dries out, no restrictions, such as the absence of a liquid bridge, stop the TFF from growing. BF can maintain a long TFF, but only a limited CF extension; the liquid ring near the evaporation front is isolated in stage 2 (Figs. 4.3c & d), and TFF becomes the dominant water transport mechanism for evaporation. After an initial, short receding, the evaporation front in MM5-glass *remains close to the open boundary due to the continuously extended TFF region*, while the evaporation front in MM5-Si recedes continuously, resulting in a higher evaporation rate in MM5-glass than MM5-Si.

Figure 4.10 shows the extensions of CF and TFF regions as function of cumulative mass loss [mm]. Figure 4.10a shows a similar transision at 5-6 mm as Fig. 4.8a, where the extension of CF region terminates the steep increase and enters a moderate increase period. The consistant transitions in Fig. 4.10a and Fig. 4.8a indicate a *temperature-independent characteristic evaporation depth*, at which, the growth of CF extension is surpressed under the impacts of viscous and gravitational forces, eventually causes the hydraulic detachment and leads to the abrupt evaporation rate falling.

The linear growth of the TFF region extension in Fig. 4.10b strongly indicates the complete wetting and spontaneity of TFF caused by surface roughness, which will be discussed in the latter chapter.

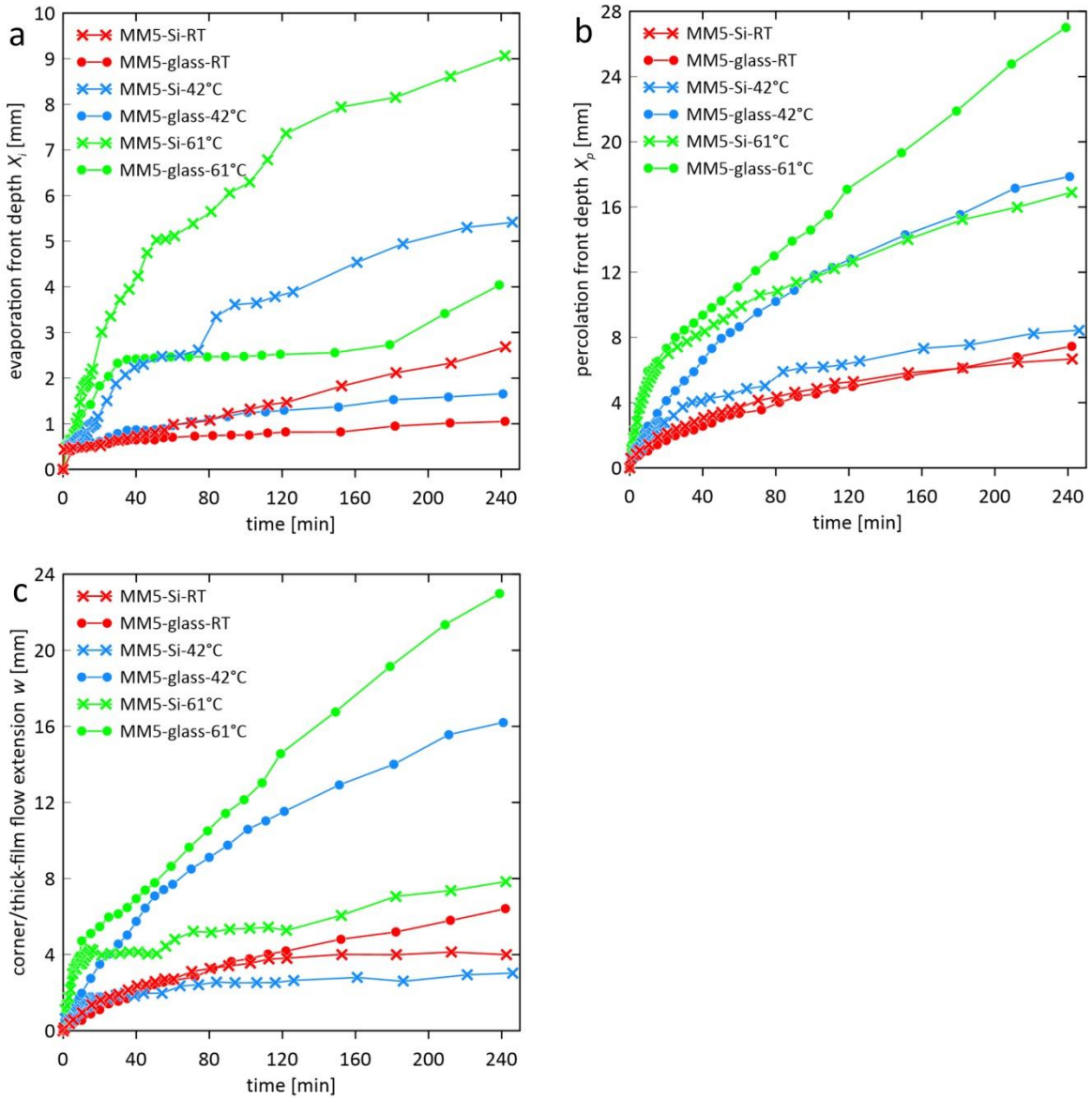

Figure 4. 9 (a) Mean evaporation front depth x_i (distance between the open boundary and averaged evaporation front) versus time for MM5-Si and MM5-glass; (b) mean percolation front depth x_p (distance between the open boundary and averaged percolation front) versus time for MM5-Si and MM5-glass; and (c) CF/TFF region extension w (distance between the averaged evaporation and percolation front) versus time for MM5-Si and MM5-glass (Fig. 13; Ding & Geistlinger, 2021).

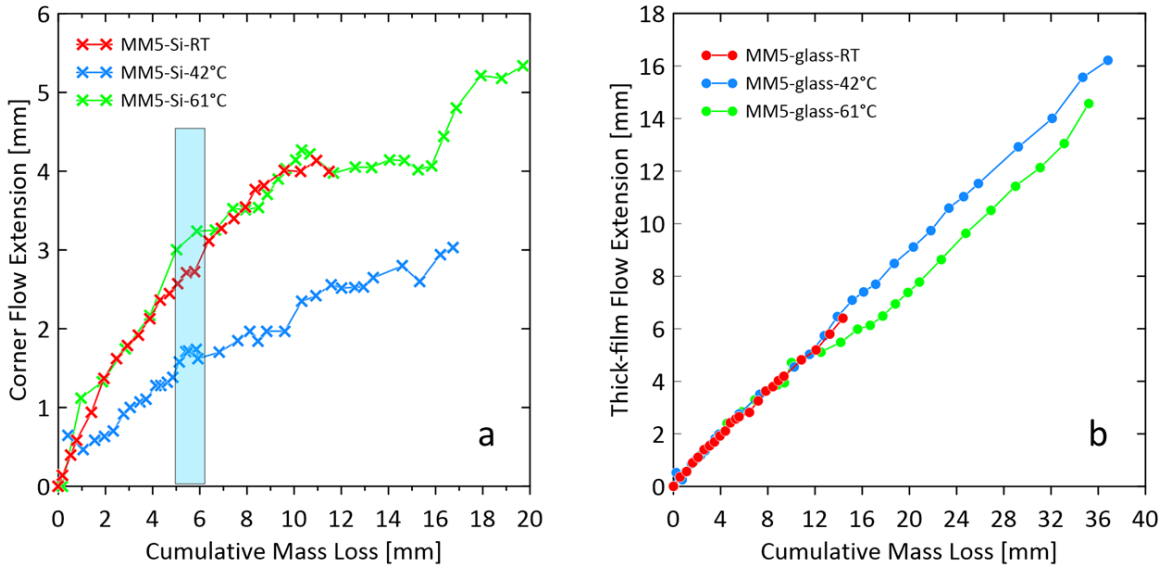

Figure 4. 10 (a) The extension of corner flow region in MM5-Si and (b) extension of thick-film flow region in MM5-glass as a function of cumulative mass loss (in the form of evaporative depth) under three temperatures (Figs. S1d & S2d; Ding & Geistlinger, 2021).

4.4 Viscous Length Scale Analysis

Physically, the extension of the CF- and TFF region during *stage2* is described by the time- and temperature dependence of the *viscous length*

$$L_{visc}(t,T) = k \cdot A \cdot \Delta P_w / [\mu(T) \cdot Q_w(t,T)], \qquad \text{Eq.4.4. 1}$$

where k is the permeability [m^2], A the cross section [m^2], μ the dynamic viscosity [Pa·s], ΔP_w the driving water pressure difference [Pa], and Q_w the internal water flow (CF or TFF) [m^3/s]. The internal water flow must satisfy the boundary condition at the evaporation front, i.e. is controlled by the time t- and temperature T-dependence of the evaporation rate $Q_{ev}(t,T)$. A steady state is maintained between water flow and evaporation, because the balancing diffusion process within the gas phase is always faster than the slow internal water flow. To discuss the T-dependence, we have to discuss two competing processes. First, the significant decrease of the water viscosity, i.e. $\mu(60°) \approx 0.5\ \mu(\text{RT})$, which causes an increasing L_{visc}. Second, the increase of the evaporation rate (higher diffusion coefficient), which causes a decreasing L_{visc}. Obviously, the viscosity effect dominates, as Fig. 4.9c impressively demonstrates and as we have shown for CF (Geistlinger et al., 2019). Hence, L_{visc} will increase with temperature.

We think that the inverse behavior of the CF region, the extension at higher temperature (42°; blue curve with crosses in Fig. 4.9c) is smaller compared to that at lower temperature (RT; red curve with crosses), is caused by averaging the fractal evaporation front. The higher fractality of the evaporation front at 42° yields the expected higher mass loss. The fractality impact will be discussed in the next section.

Let us then discuss the time dependence. From Eq. 4.4.1 it follows that L_{visc} will increase with time, because $Q_{ev}(t,T)$ and hence Q_w will decrease with time (decreasing vapor concentration gradient). The t-dependences of the viscous length (= $w(t)$; extension of the CF- or TFF region), the cumulative mass loss (= $m_{loss}(t) \propto \rho_w.w(t) \cdot A$; see the proportional relation between $m_{loss}(t)$ and $w(t)$ in Fig. 4.10), and the evaporation rate (= $Q_{ev}(t) = dm_{loss}(t)/dt$) must strongly correlate (see Fig. 4.11 c, d, e).

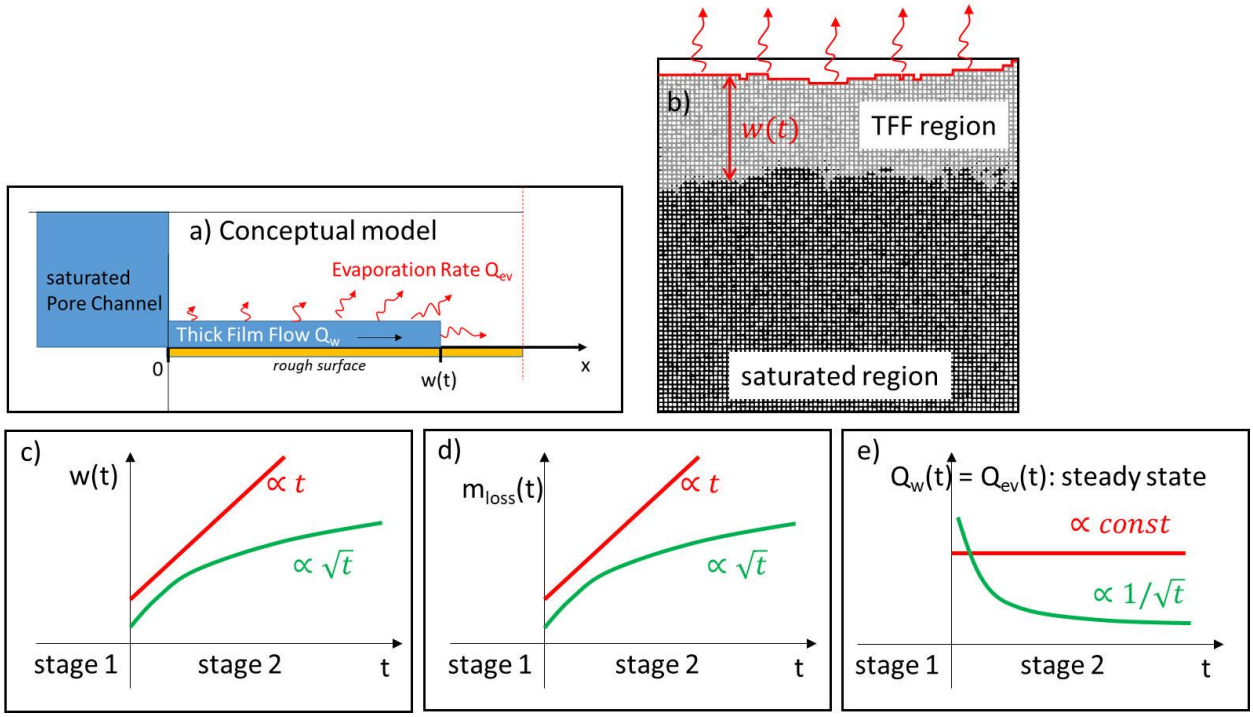

Figure 4. 11 (a) Conceptual model of thick-film flow on a rough surface. (b) Large film surface in MM5-glass (61°C; 240min), thick-film flow region and saturated region are displayed by the gray and black area, respectively, evaporation front is displayed by the red line. Figures (c) to (e) show the temporal correlations of the viscous length $L_{visc}(t)$ (= $w(t)$), the cumulative mass loss, and the evaporation rate (green curves: $\sqrt{t}$-behavior, red curves: linear t-behavior) during stage 2 (Fig. 14; Ding & Geistlinger, 2021).

If viscous forces dominate the internal water flow, the viscous length and the mass loss are described by a diffusion-like $\sqrt{t}$-behavior (Brutsaert and Chen, 1995), which was observed for soils (Geistlinger and Leuther, 2018); for CF in silicon micromodels (Geistlinger et al., 2019), and for TFF in glass-ceramic micromodels (Geistlinger et al., 2016).

In this study, Figure 4.12 shows the best fits (red lines) to the stage 2 time behavior of the mass loss, which indicates that the 2D micromodels can be good representatives of soil. For experiments 1 (RT) and 2 (42°C) a $\sqrt{t}$-behaviour with high statistical significance was observed (regression coefficients near 1; Fig. 4.12 a, b, d, e). For higher temperatures (61°C, experiment 3) there is a transition to a linear time behavior again with high statistical significance (Figs. 4.12 c and f). This time-behavior correlates with the time behavior of the extension of the CF- and TFF-region with high statistical significance (Fig. 4.13).

Although both micromodels exhibit a similar $\sqrt{t}$-behavior, the *t*-dependent increase of the TFF-region is stronger compared to that of the CF-region; e.g. the TFF-region is 5 times larger than the CF-region at 100 min for experiment 2 (42°) (compare the blue curves in Fig. 4.9c and Figs. 4.13 b and e) and the slope of the TFF-curve is about 10 times larger. This indicates that the driving "force" (water pressure difference ΔP_w in Eq. 4.4.1) is larger for TFF than that for CF. For CF the water pressure difference is given by the curvature at the top and that at the root of the CF (see Fig. 2.11). Taking into account that the critical contact angle within a rectangular geometry is 45° (Zulfiqar et al., 2020) and that the contact angle of the silicon-micromodel is about 35.5°, there is a weak curvature at the CF-top, which causes a weak driving "force". Hence, the weak hydrophilic wettability of the smooth Si-surface is responsible for this weak driving "force".

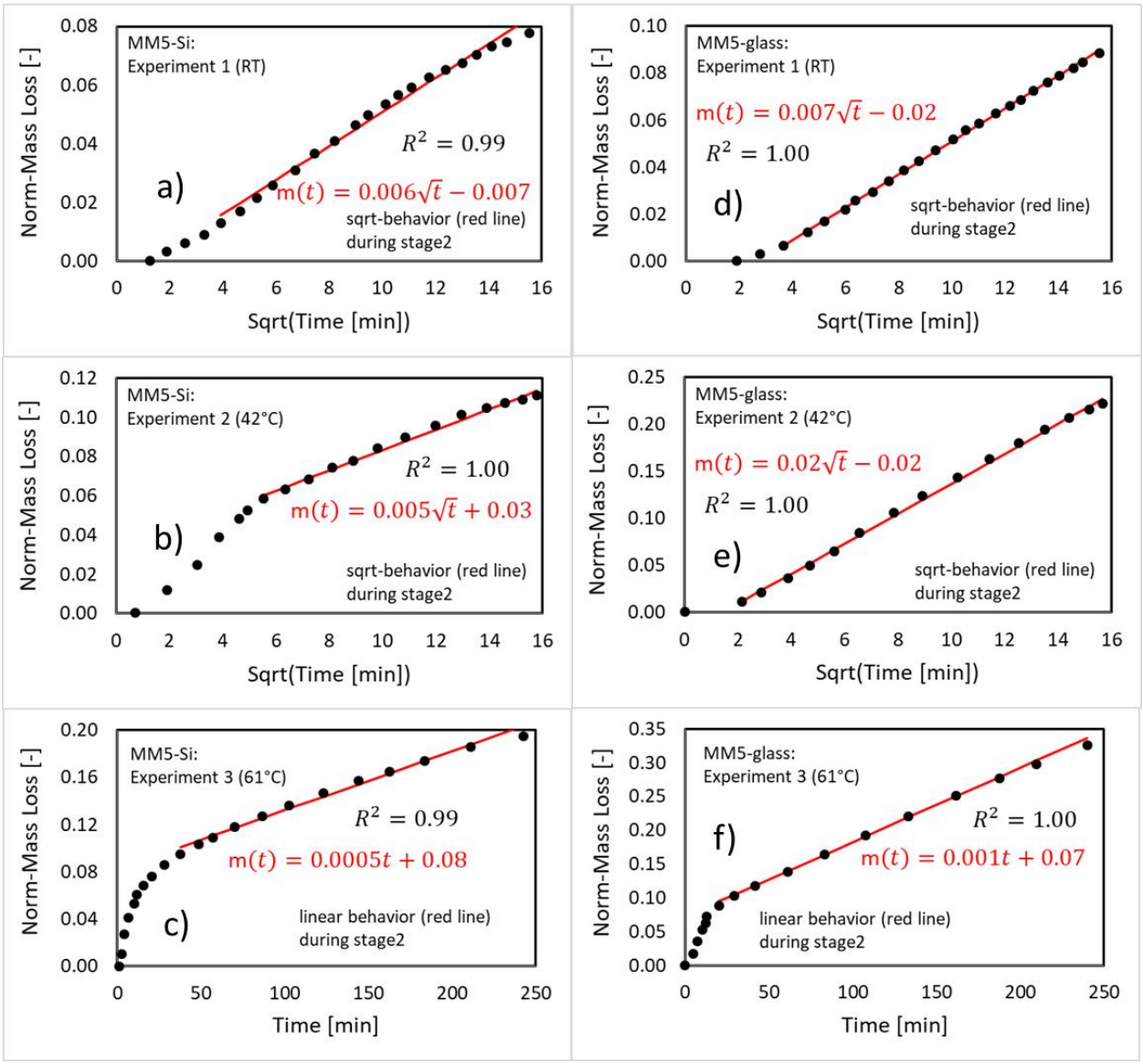

Figure 4. 12 Normalized mass loss versus time (black dots): a), b), d), and e) versus $\sqrt{t}$; c) and f) versus t. The red lines show the best fits (red formulas) to the experimental data during stage 2. The regression coefficient R^2 is approximately 1for all fits (Fig. S3; Ding & Geistlinger, 2021).

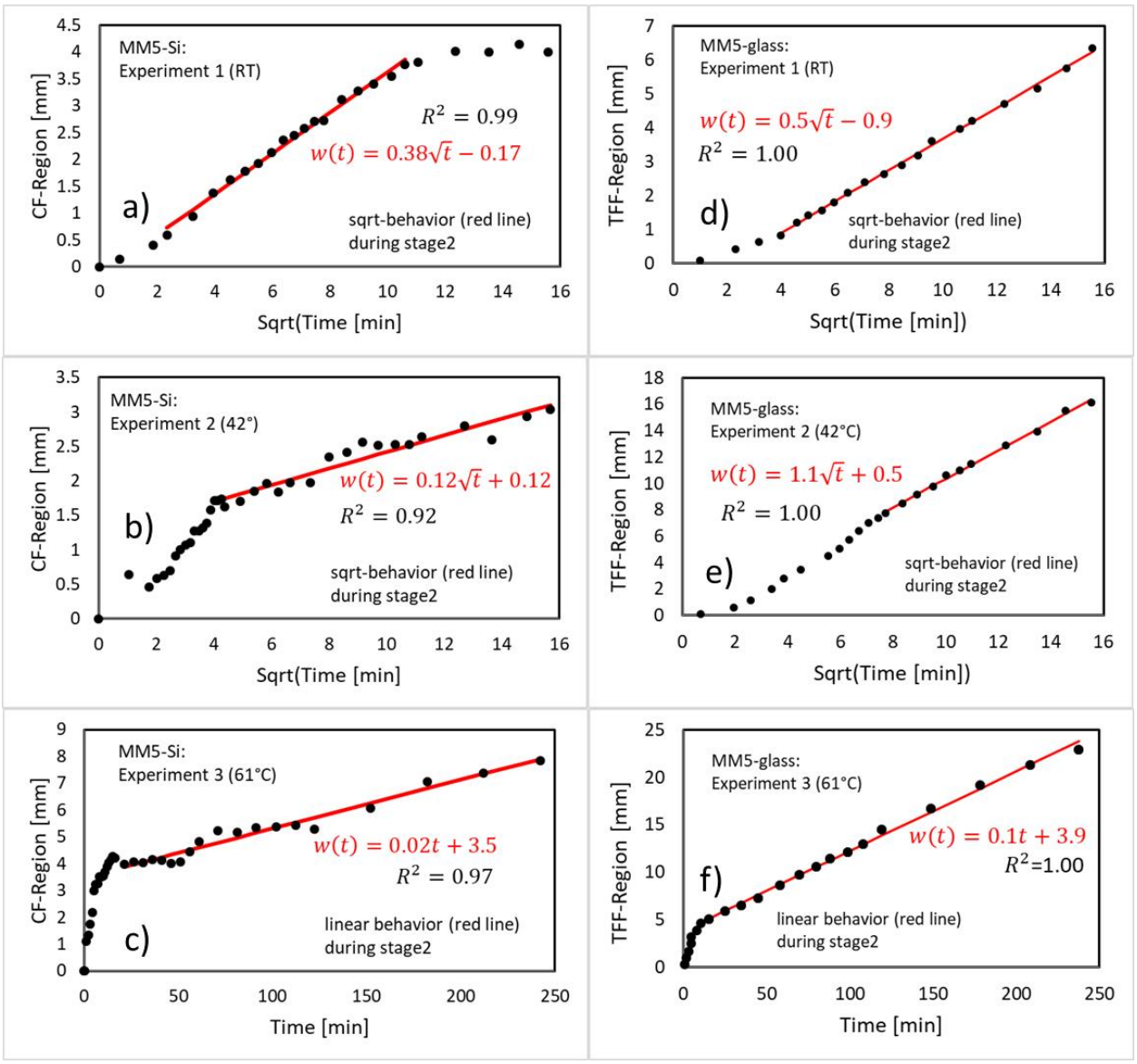

Figure 4. 13 Extension of the CF- and TFF-region *w(t)* versus time (black dots): a), b), d), and e) versus $\sqrt{t}$; c) and f) versus *t*. The red lines show the best fits (red formulas) to the experimental data during stage 2 (Fig. S4; Ding & Geistlinger, 2021).

4.5 Complete Wetting and Spontaneous Thick-film Flow Caused by Surface Roughness

Naively, we would think that thick-film flow on a rough glass surface with an intrinsic contact angle of about 30° will also cause a weak driving "force". However, the wettability of rough surfaces is controlled by the degree of roughness, r_F (= ratio of rough surface area to flat surface area; Wenzel, 1936; Levinson et al., 1988; Bico et al., 2001; Zulfiqar et al., 2020), i.e. surface roughness may cause complete wetting. This was demonstrated experimentally glass-ceramic micromodels in Geistlinger et al. (2016) and Zulfiqar et al. (2020). How can complete wetting occur on a surface with a contact angle of about 30°? The answer is given by Wenzel's argument (Wenzel, 1938): *Surface roughness amplifies both hydrophilicity and hydrophobicity*. For contact angles smaller than 90°, a high degree of surface roughness can lead to *complete* wetting. Physically, it means that the *Free Energy* of the 3-phase-system is lowered, if the water film wets the rough surface (see Fig. 4.11a). According to a realistic wetting model derived by modifying Wenzel's model, the *complete-wetting* condition (Zulfiqar et al., 2020, Sect. 4.1.1.) is given by:

$$\theta_0 < \theta_c, \qquad \text{with } \theta_c = arccos\left(\frac{1-\phi_s}{r_F-\phi_s}\right), \qquad \text{Eq.4.5. 1}$$

where θ_0 is the equilibrium contact angle of the liquid on an ideal flat surface of the same chemical composition (i.e., the intrinsic contact angle) and ϕ_s is the dry part of the surface area. If water flows only along the valleys of the grooves, the hills define ϕ_s. The physical meaning of Eq. 4.5.1 is that for all $\theta_0 < \theta_c$ the thick film flow (TFF) advances as long as the entire surface is covered by a water film. The range of the critical contact angle θ_c is determined by the degree of surface roughness r_F (the ratio of rough surface area to flat surface area). Assuming that the cross sections of the grooves (= tiny cavities in Fig. 1.3b) can be approximated by equilateral triangles, the rough surface area is twice the flat area (Fig. 4.14). Inserting r_F = 2 into Eq. 4.5.1 and assuming that the grooves are completely covered by a thick film flow (ϕ_s = 0), we obtain θ_c = 60°. This means that for all intrinsic contact angles smaller than this critical value *complete wetting* or *spontaneous* thick-film flow occurs. The linear growth of TFF extension versus cumulative mass loss [mm] strongly proves the complete wetting and spontaneity (Fig. 4.10b). This qualitative change from *partial* wetting ($\theta \approx 30°$) to *complete* wetting by surface roughness causes the strong driving "force" of TFF.

However, for the flat surface of Si micromodels (r_F = 1), complete wetting and spontaneous film is only possible when θ_0 = 0, which explains the bubble phenomenon in silicon micromodels (Appendix V).

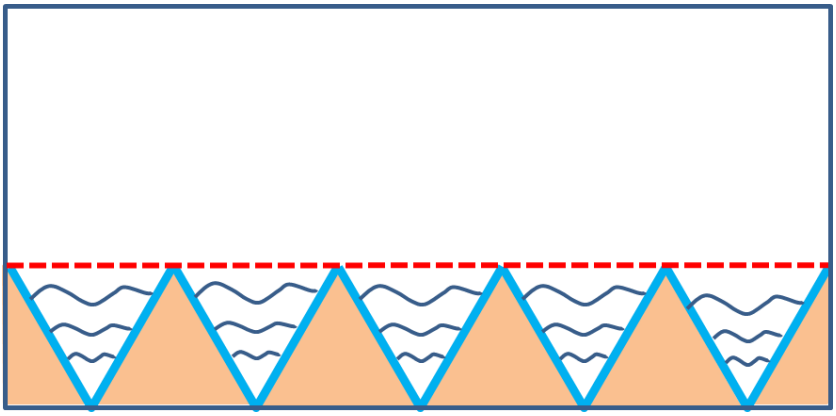

Figure 4. 14 Illustration of rough surface degree r_F of 2. The grooves are equilateral triangles, the rough surface and flat surface area are represented by the blue solid line and red dashed line, respectively.

Based on the experimental results and explanations, the answer of problem 8 listed in Chapter 1 is obvious, that, the two geometric properties of soil system, the angularity of pore space and grain surface roughness, enable the presences of corner and thick-film flow which have stronger capillary suction than the bulk flow. Eventually, evaporation is enhanced due to the stronger hydraulic continuity sustained by corner and thick-film flow. Especially the surface roughness may lead to complete wetting and largely enlarge the hydraulic connection region, which deserve more considerations in evaporation studies. In real soil, the more hydrophilic soil was observed to enhance evaporation. Letey et al. (1962a) conducted sand treatment with NH_4OH extract of chaparral litter to alter the contact angle from the range of 43° to 52° (the untreated sand) to the range of 81° to 84°. As a result, evaporation was reduced to approximately half by the NH_4OH-treatment relative to the untreated sand evaporation (Letey et al., 1962b). As the water at the soil surface evaporated, the capillary action in the sand with higher contact angle was weaker and lead to a lower capillary rise, and eventually a thicker dry layer below the soil surface which reduces the evaporation (Letey, 1962b).

As we mentioned in the Chapter 4.4, that, increasing the temperature up to 61° (experiment 3) we discover an interesting transition from $\sqrt{t}$- to linear t-behavior both for the mass-loss and the extension of CF/TFF-region. This means a transition from $1/\sqrt{t}$- to constant evaporation rate (Fig. 4.11) and that at late stage 2 the steady-state vapor-concentration gradient becomes very weak and tends to be constant.

Again, the strong increase of the TFF-region extension compared to that of the CF-region is surprising. This implies that with increasing temperature evaporation from the large gas-water interface (= film surface; see Fig. 4.11 a, b) leads to a thinning effect. Hence, attractive long-range interaction become more dominant in thinner films, which allows the thick-film to flow faster (linear *t*-behavior) and longer (larger TFF-region). A rough estimate of the film thickness verifies this physical picture. For the increasing temperature from RT to 61°, a decreasing film thickness from 34 µm to 13 µm was obtained (150min; Fig. 4.15).

The film thickness was estimated by the mass difference of the gravitational measurements and the IP-measurement, because the IP counts only the water mass within the saturated region, whereas the gravitational measurement measures the total water mass. Therefore, the m_{loss} obtained by IP is always smaller than the gravitational m_{loss} obtained by weighing, and the mass difference must be the mass of the thick water film. Note that, the m_{loss}-data and the *w*-data are obtained by two independent measurements (= two IP-routines): 1) m_{loss} is obtained by summing over all dry duct channels (region above the percolation front) neglecting the small retained water mass of TFF, and 2) the CF-/TFF-region extension *w* is obtained by the geometric averaging of the evaporation- and percolation front. The film thickness d_{FT} is estimated by $d_{FT} = \frac{m_{loss}}{w * L_m * \emptyset * \rho_w}$, where ρ_w denotes the water density, $\emptyset$ and L_m denote the micromodel porosity and width (= 80mm), respectively.

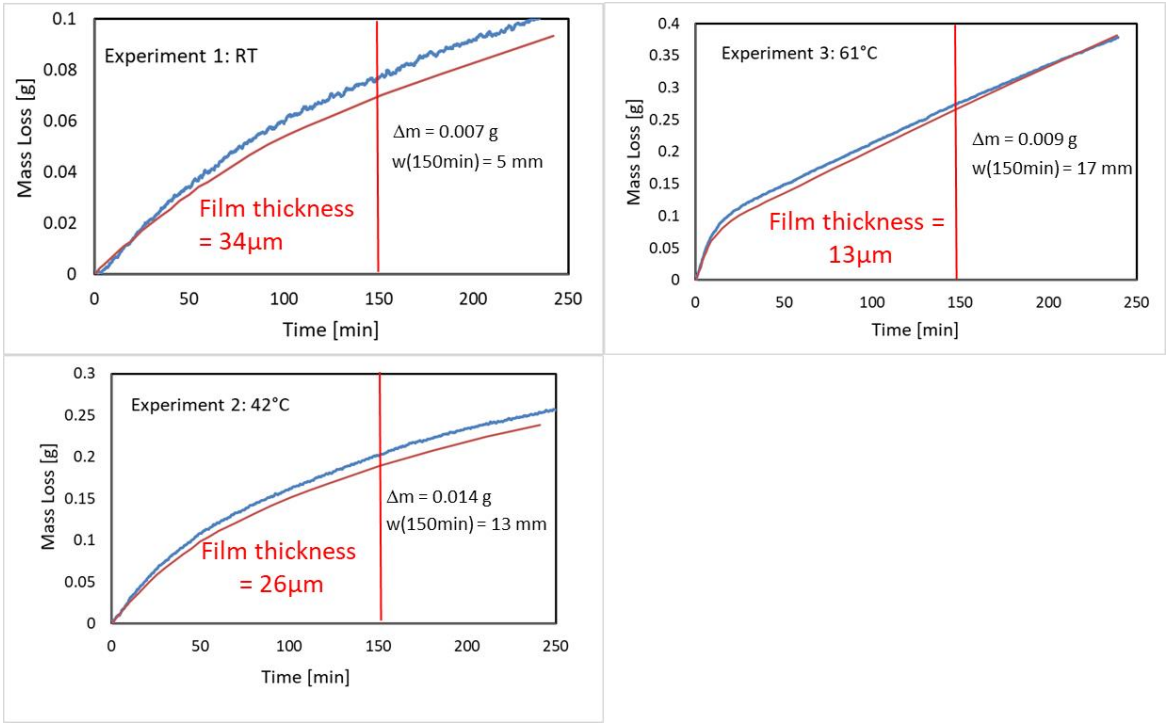

Figure 4. 15 Film thickness estimation of MM5-glass, red curves are IP-measurements, blue curves are gravitational measurements (Fig. S5; Ding & Geistlinger, 2021).

4.6 Fractal Evaporation and Percolation Fronts

Figure 4.17 displays the fluid pattern images after image processing of all micromodels at four experimental times. The saturated BF regions are displayed in black and the partial wet CF/film regions are displayed in grey. The two glass micromodels display large extensions of film regions and the evaporation fronts stay closely to open surface, while the evaporation fronts of the two silicon micromodels recede into the porous media.

Evaporation has clear similarities to a drainage process, as is a fluid displaced by a lighter and less viscous fluid, and the pore invasion is determined by the pore size distribution. The probability of pore invasion is random in space because of the randomly distributed pore sizes, therefore, the evaporation pore invasion resembles invasion percolation, and the percolation and evaporation fronts hold the same fractal characteristic as drainage front (Shaw 1987; Prat, 1995; Yiotis et al., 2010). An example of the fluctuating and fractal behavior of the percolation and evaporation fronts observed in MM5-Si is displayed in Fig. 4.16.

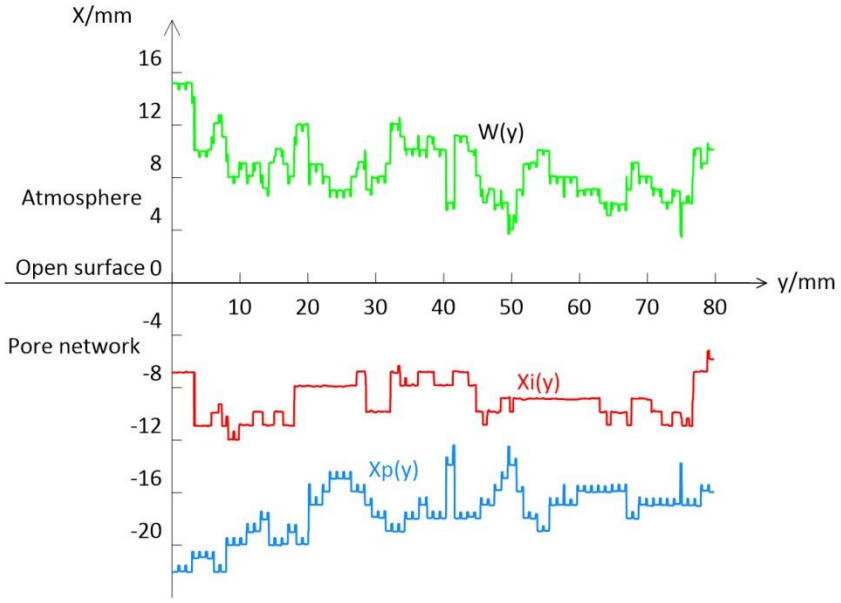

Figure 4. 16 Plot of the coordinates of each pixel on percolation front $x_p(y)$, evaporation front $x_i(y)$ and the CF extension *w(y)* of MM5-Si for experiment 3 (61°C) at t = 240min (Fig. 15; Ding & Geistlinger, 2021).

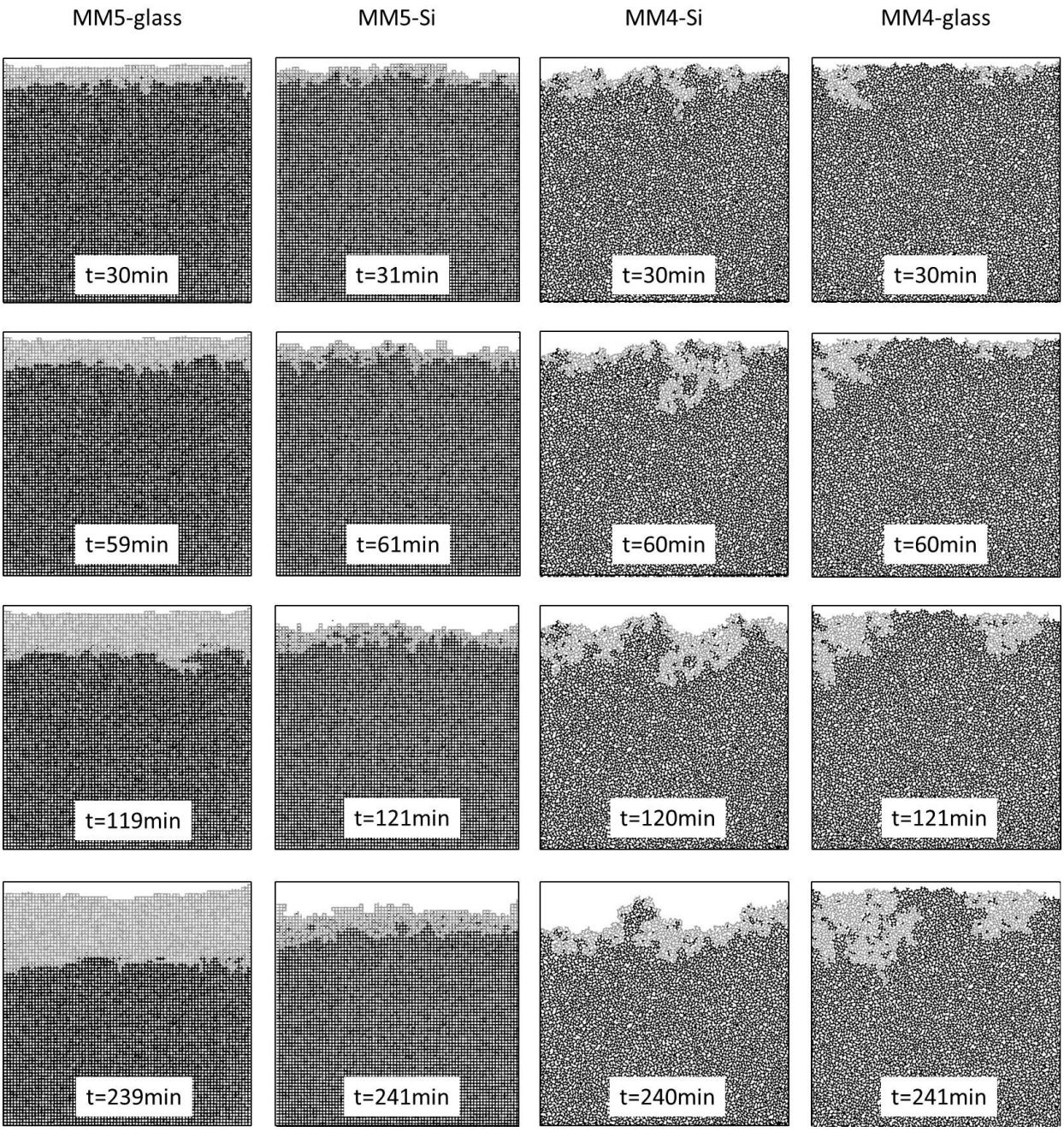

Figure 4. 17 Fluid pattern images of all micromodels at four experimental times. The saturated bulk flow regions are displayed in black and partial wet corner flow/film regions are displayed in grey.

To analyze the degrees of fractality and fluctuation of all fronts, the front width and fractal dimension D_f were investigated (Fig. 4.18). The front width is defined as the largest deviation of front in vertical direction, which is given by the difference of the maximum and minimum y-coordinates on the front. The fractal dimension is achieved by the "box counting" method (Smith et.al., 1996) in ImageJ, that, sets of square boxes are used to cover the whole boarder (front) and each set is characterized by a box size. The method counts the number of boxes *N* of a given size ε_0 needed to cover a one-pixel-wide binary front, D_f is defined as:

$$D_f = \lim_{\varepsilon_0 \to 0} \frac{\log N(\varepsilon_0)}{\log(1/\varepsilon_0)}. \qquad \text{Eq.4.6. 1}$$

The algorithm of the plugin "FracLac" repeats the box counting with different box size ε_0, as a result, the plot of $\log N(\varepsilon_0)$ and $\log \varepsilon_0$ data generates a linear-fitted line, with the slope $S = -D_f$ (Fig. 4.19).

In general, the percolation fronts (light yellow section in Fig. 4.18) are more fractal than the evaporation fronts, the different pore structures cause no dramatic difference regarding the D_f of percolation fronts. While, for the evaporation fronts, the irregular structure MM4 (pink section in Fig.4.18) leads to higher D_f than the regular structure MM5 (light blue section in Fig.4.18). The TFF displays significant impact on the front width of evaporation fronts. I expect the irregular structure MM4 would lead to a more heterogeneous front and larger front width than the regular structure MM5, as verified by the comparison between MM4-Si (green circle) and MM5-Si (red circle), that, MM4-Si has double front width of MM5-Si. However, the TFF flattens the evaporation fronts and reduces the front widths of MM5-glass (blue circle) and MM4-glass (black circle) to the same level, which furtherly indicates the expansion of TFF is spontaneous and independent of the pore structure.

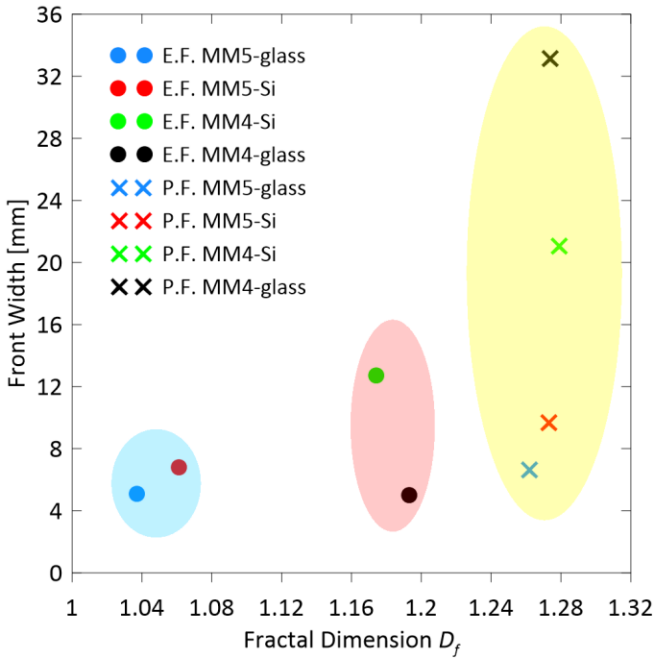

Figure 4. 18 The front widths and fractal dimensions of evaporation and percolation fronts of all micromodels (t = 240 min; 61°C). The circles represent the evaporation front (E.F.) and the crosses represent the percolation fronts (P.F.).

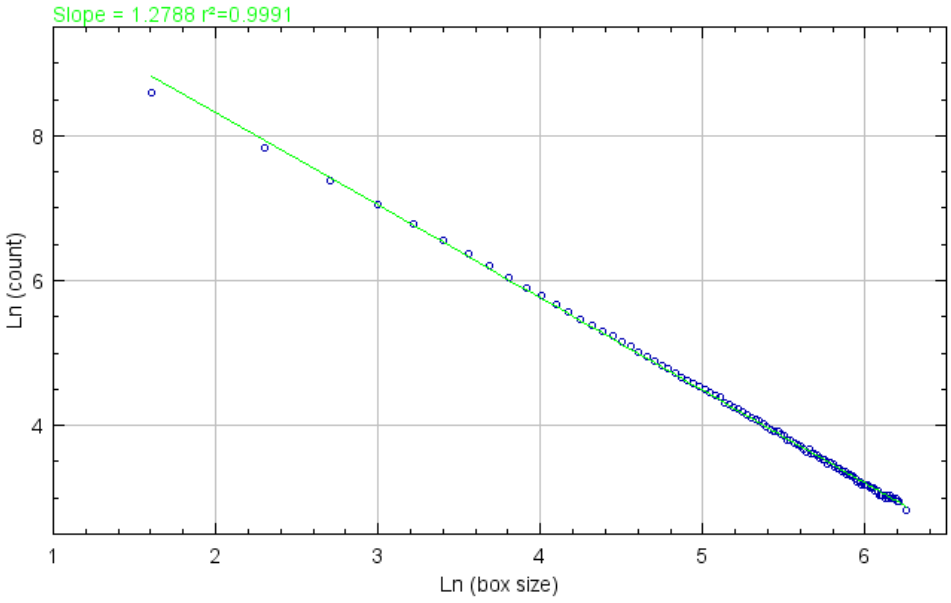

Figure 4. 19 An example of the determination of fractal dimension D_f with "box-counting" method in ImageJ. The plotted data is from the percolation front of MM4-Si (t = 240min; 61°C).

Knowing the IP-derived $x_i(t)$-values we can calculate the evaporation flux based on Fick's first law (more details see Eq. 2.2.11 & 2.2.12)

$$\langle Q_{ev} \rangle = A_g \langle j_x^{diff} \rangle \cong -A_g D_g^{eff} \frac{\Delta C}{\Delta x} = -A_g D_g^{eff} \frac{C_a - C_s}{\delta + |x_i|}, \quad \text{Eq.4.6. 2}$$

where D_g^{eff} denotes the effective vapor diffusion coefficient and A_g the cross-sectional area for gas diffusion. A_g is given by the total cross-sectional area of, the pores at open surface in MM5, or the pore throats of the first layer grains in MM4 (see Fig. 3.11b). The Millington-Quirk tortuosity model (Millington & Quirk, 1961) was applied for the D_g^{eff}, i.e.

$$D_g^{eff} = D_g^0 \tau, \quad \text{Eq.4.6. 3a}$$

with the tortuosity τ and the temperature-dependent gas phase diffusion coefficient $D_g^0(T)$ ($\mathrm{m^2/s}$, Shahraeeni et al., 2012),

$$D_g^0(T) = 2.31 \times 10^{-5} \left(\frac{T}{T_0}\right)^{1.81} \text{(T in K)} \quad \text{Eq.4.6.3b}$$

$$\tau = (\phi)^{1/3} \quad (\phi \text{ - porosity}). \quad \text{Eq.4.6.3c}$$

According to the ideal gas law, C_s can be derived by

$$C_s(molar) = \frac{n}{V} = \frac{P_{vapor}(T)}{RT},$$

$$\rightarrow C_s = M_{H_2O} * C_s(molar) \quad \text{Eq.4.6. 4}$$

where R is the ideal gas constant, $P_{vapor}(T)$ is the temperature-dependent saturated vapor pressure, M_{H_2O} is the water molar mass (≈18 *g/mol*). Based on the experimental relative humidity (RH; %), the ambient vapor concentration C_a is given by

$$C_a = C_s * RH. \quad \text{Eq.4.6. 5}$$

With the measured $\langle Q_{ev} \rangle$ of stage 1 (experiment 3; 61°C), the boundary layer thickness δ was derived ($x_i = 0$), i.e. $0.121mm$ for MM5-glass, $0.171mm$ for MM5-Si, 0.274mm for MM4-Si and 0.176mm for MM4-glass. The boundary layer thickness remains constant during the evaporation.

With a set of the x_i-values of stage 2 (e.g. Fig. 4.9a), we can calculate the $\langle Q_{ev} \rangle$ and find the best fitting function for the $\langle Q_{ev} \rangle$curve versus time, the corresponding mass loss m_{loss} can be obtained via the integration of the evaporation flux function. The best fitting function of $\langle Q_{ev} \rangle$ for MM5-Si and MM5-glass is formulated by

$$\langle Q_{ev} \rangle = q_1 + q_2 \frac{1}{t} + \frac{q_3}{2\sqrt{t}}, \qquad \text{Eq.4.6. 6}$$

and the best fit function for m_{loss} is

$$m_{loss}(t) = q_1 t + q_2 \ln(t) + q_3 \sqrt{t}. \qquad \text{Eq.4.6. 7}$$

For MM4-Si, the best fitting function of $\langle Q_{ev} \rangle$ is formulated by

$$\langle Q_{ev} \rangle = q_1 + 2q_2 t + \frac{q_3}{2\sqrt{t}}, \qquad \text{Eq.4.6. 8}$$

and the best fit function for m_{loss} is

$$m_{loss}(t) = q_1 t + q_2 t^2 + q_3 \sqrt{t}. \qquad \text{Eq.4.6. 9}$$

I applied the x_i-values at t = 10, 20, 30, 60, 120, 180 and 240 min, the calculated evaporation rates (red dots in Fig. 4.20) with the best fittings (red curves in Fig. 4.20), and the corresponding mass loss curves via integration (red curves in Fig. 4.21), are too low compared to the experimental data (black dots and curves in Fig. 4.20 and 4.21). This is caused by the oversimplified assumption that the evaporation process can be described by an effective single-square capillary (SSC-model), i.e. by a *flat averaged* evaporation front, which causes a fundamental inconsistency with the real physical fractal behavior of the evaporation front in a porous medium.

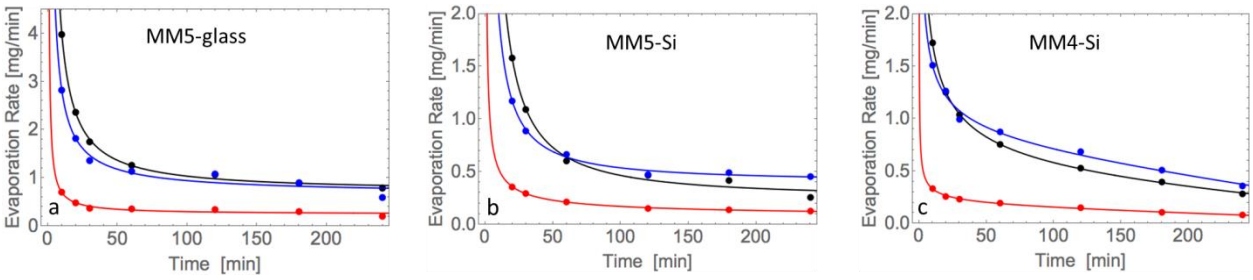

Figure 4. 20 Evaporation rate versus time for (a) MM5-glass, (b) MM5-Si and (c) MM4-Si (61°C): The black dots show the experimental data with the best fitting curves in black. The red dots are calculated values based on a flat evaporation front with the best fitting curves in red, and the blue dots are calculated values based on a fractal evaporation front with the best fitting curves in blue.

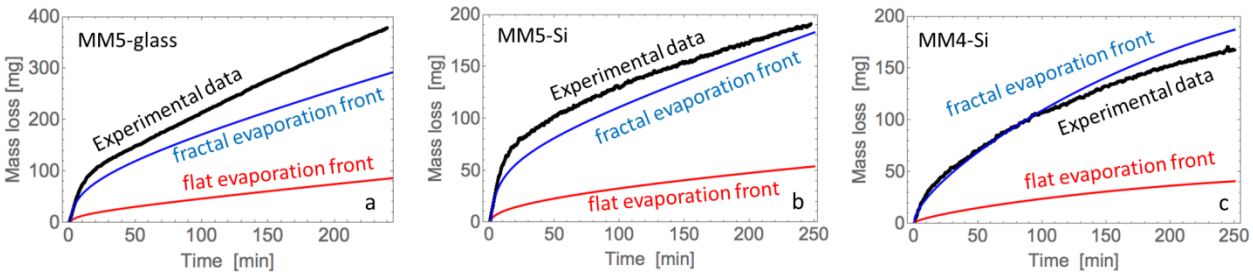

Figure 4. 21 Mass loss versus time for (a) MM5-glass, (b) MM5-Si and (c) MM4-Si (61°C): The black curves show the experimental data. The red curves are calculated data based on a flat evaporation front, and the blue curves are calculated data based on a fractal evaporation front.

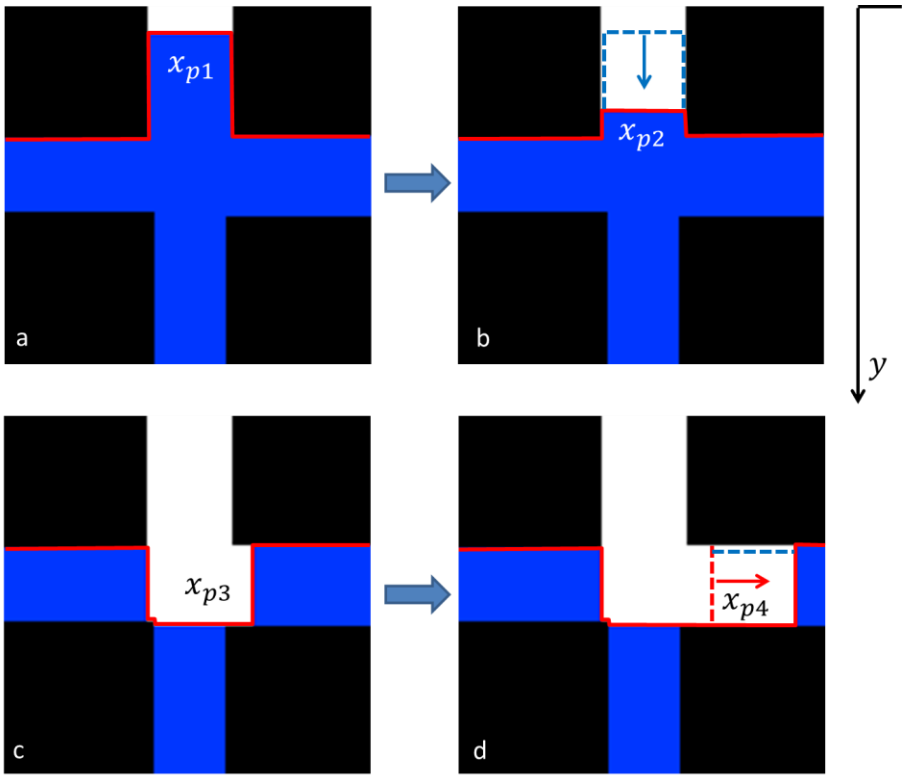

Figure 4. 22 Examples of the percolation front movements when water recedes in the vertical (a to b) and horizontal (c to d) direction.

The IP-derived $x_i(t)$ and $x_p(t)$-values (see the geometric averaging in Fig. 3.10) describe the front movement in the vertical direction (y-direction; Fig. 4.22 a to b), but cannot truly map the front movement in the horizontal direction (Fig. 4.22 c to d). When water recedes vertically, the increased y-coordinates of the moved front section (the blue dashed line in Fig. 4.22b) directly results an increased x_p value. While, when water recedes horizontally, a large part of the y-coordinates in the moved front section stays constant (the red dashed line in Fig. 4.22d). Therefore, the IP-derived x_p underestimates the evaporation in horizontal direction.

The x_p values are plotted as function of the evaporative depth (the weighing cumulative mass loss m_{loss} divided by A_g) in Figure 4.23. We would expect the IP-derived percolation front depth (x_p) to be equal to the weighing-derived evaporative depth. However, the weighing-derived evaporative depth only considers mass loss being contributed by the vertical evaporation ($= m_{loss}/A_g$; Fig. 4.24b), while the IP-derived x_p measures the depth as a consequence of actual evaporation in both horizontal and vertical directions (Fig. 4.24a). As a result, the linear-correlations of the two independent depths show slopes of 0.45, 0.55 and 0.73 for MM5-glass, MM5-Si and MM4-Si, respectively. The fractal fronts in MM4 cause inaccuracies for the geometric averaging, where some deviation can be seen in the Fig. 4.23c. Since MM4-glass has highly fractal and fluctuated percolation front (Figs.4.17 and 4.18), the geometric averaging of x_p in MM4-glass is not representative and not displayed.

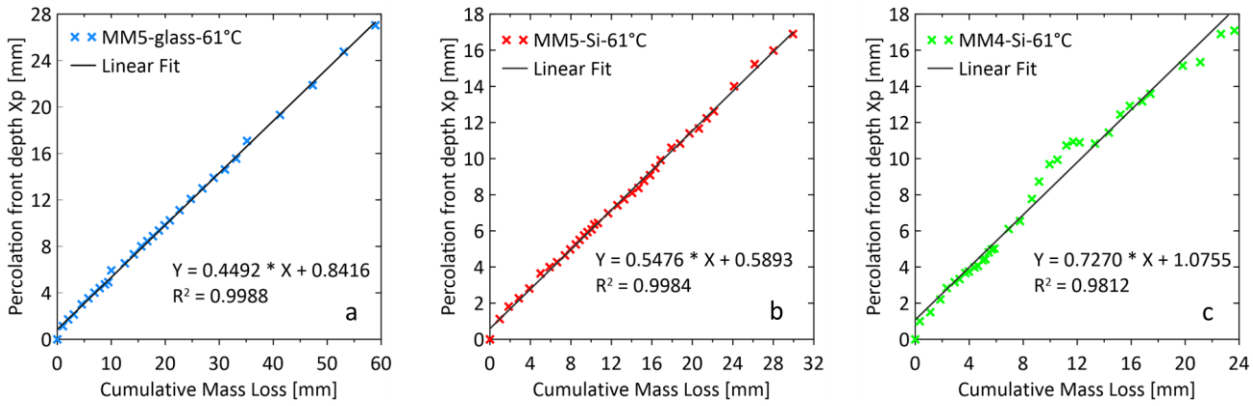

Figure 4. 23 The percolation front depth x_p in (a) MM5-glass, (b) MM5-Si and (c) MM4-Si as function of the cumulative mass loss (in the form of evaporation depth; 61°C). The IP-derived x_p values are linear-correlated to the weighing-derived evaporation depth.

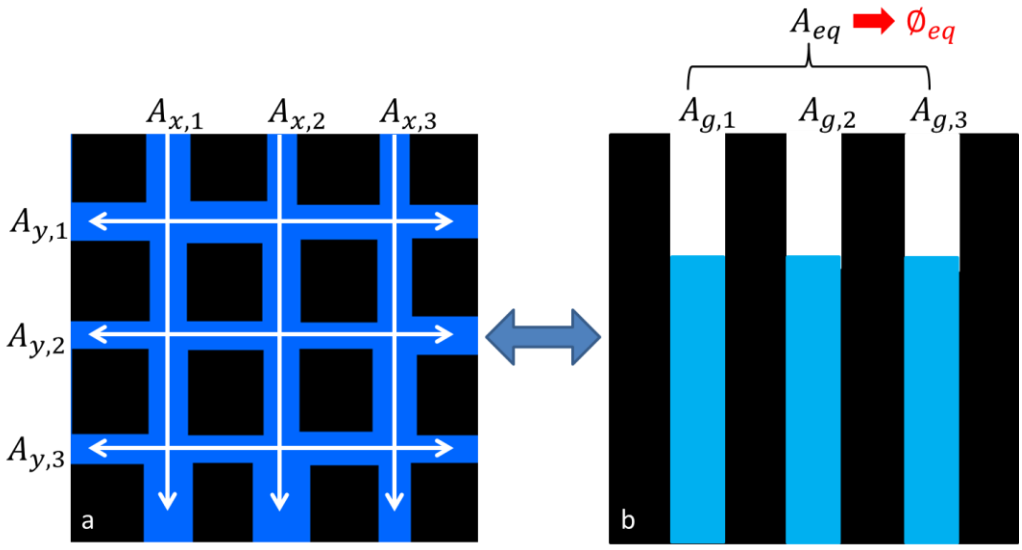

Figure 4. 24 The actual evaporation in both horizontal and vertical directions (a) is mapped into one-direction (b) by an equivalent cross sectional area A_{eq} and front porosity $\emptyset_{eq}$.

Apparently, if we compare Fig. 4.24a and b, the different inner pore structures will lead to different diffusion efficiencies, which cannot just simply explained by the pore network porosity (Eq. 4.6.3). As x_p is a vital parameter to represent the evaporation efficiency, the most appropriate picture to match the diffusion-based model (Eq. 4.6.2) is shown as Fig. 4.24b, where the vertical parameter x_p describes evaporation only happening in the vertical direction. Therefore, we can map the two-direction evaporation in micromodels into one-direction by introducing an equivalent cross sectional area A_{eq} (Fig. 4.24b), which can contribute the equal evaporation amount as the experimental data, and gives an equivalent evaporation front porosity $\emptyset_{eq}$. With the A_{eq}, the weighing-derived evaporative depth ($= m_{loss}/A_{eq}$) should be equal to the IP-derived x_p (Fig. 4.25).

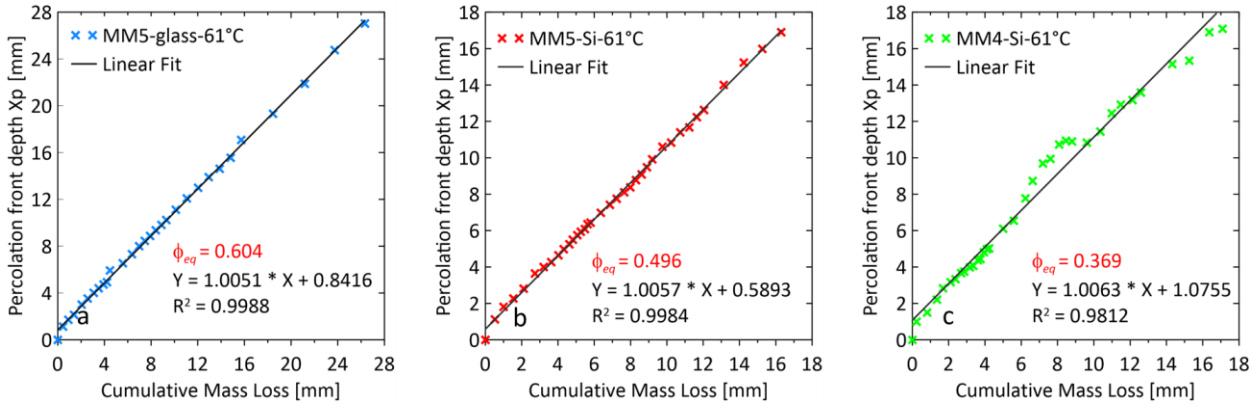

Figure 4. 25 The percolation front depth x_p in (a) MM5-glass, (b) MM5-Si and (c) MM4-Si as function of evaporation depth (cumulative mass loss divided by the equivalent cross sectional area A_{eq}; 61°C). The equivalent evaporation front porosity $\emptyset_{eq}$ are derived by the A_{eq}.

Taking into account the fractality of the evaporation front in stage 2, the flat A_g (Eq. 4.6.2) was replaced by the fractal interface $\boldsymbol{A_{gw}^{fractal} = d \cdot L_e \cdot \emptyset_{eq}}$, ($d$ - micromodel depth, L_e - length of the fractal evaporation front, see Fig. 4.26). As a result, good agreement to the experimental data was achieved for the silicon micromodels (blue curves in Fig.4.20b, c and 4.21b, c). Therefore, the problem 9 listed in Chapter 1 is explained clearly, that, the evaporation front is fractal and not smooth as approximated in the IPE model (Chap.2.1; Shahraeeni et al., 2012; Geistlinger & Leuther, 2018), the SSC model (Chap. 2.2; Yiotis et al, 2012; Geistlinger et al., 2019), or many other evaporation models (Or and Lehmann, 2019; Balugani et al., 2018; Lehmann et al., 2018; Wang et al., 2019). For a consistent description of the time-dependent mass loss and the geometry of the corner/thick-film flow region, the fractality of the evaporation front must be taken into account.

The diffusion-based model underestimates evaporation in MM5-glass (Fig. 4.21a), because the model only considers evaporation from the film front, while evaporation should also occur from the large gas-water interface (= film surface; see Fig. 4.11a).

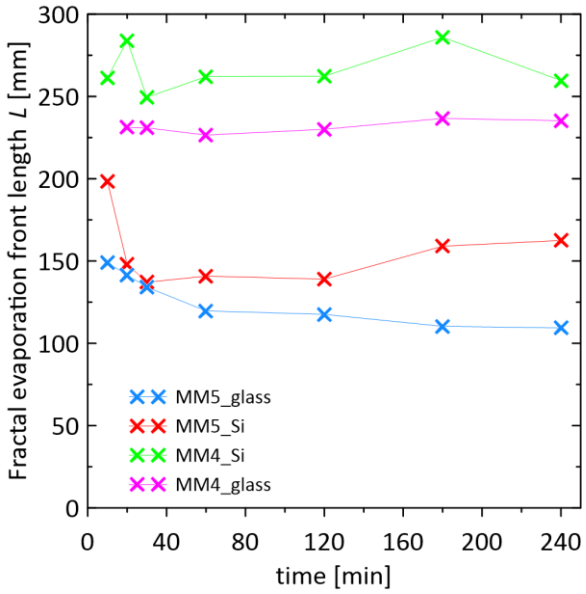

Figure 4. 26 The lengths of the fractal evaporation fronts at t=10, 20, 30, 60, 120, 180 and 240 min (Experiment 3; 61°C).

4.7 Impact of Pore Structure on Evaporation Efficiency

Mass Loss and Evaporation Rate Curves of MM5-Si and MM4-Si

The mass loss and evaporation rate curves of MM4-Si and MM5-Si at three temperatures are displayed in Fig. 4.27 and Fig. 4.28, respectively. The curves (or the tendency) show that MM5-Si leads to more efficient evaporation in the early stage, then exceeded by MM4-Si in the later stage. As stage1 is controlled by the water redistribution (capillary pumping) from large pores to small pores, the pore throats of MM4-Si cause higher capillary resistances for air invasion, and lead to a weaker stage1 evaporation than MM5-Si. In stage2, corner flow becomes the dominant evaporation mechanism for silicon micromodels, it transports water from the saturated region to a position closer to open surface and supply for evaporation. Corner flow is initiated from the bulk flow meniscus, where the pore channel/throat width directly determines the corner flow geometry (Fig. 2.4). MM4 maintains thinner corner flow than MM5 because of the small pore throat widths, and leads to a stronger corner flow connectivity, as indicated in Fig. 4.27d, that, MM4-Si has larger CF region extension than MM5-Si in stage 2. Besides, the irregular structure MM4 leads to more fractal evaporation fronts (Fig. 4.18) and hence larger front lengths than MM5 (Fig. 4.26), which also plays a role to enhance evaporation with a larger $A_{gw}^{fractal}$.

Based on the tendency of the mass loss curves in Fig. 4.27a, we expect that the mass loss of MM4-Si will eventually exceed MM5-Si in a longer term in room temperature as well.

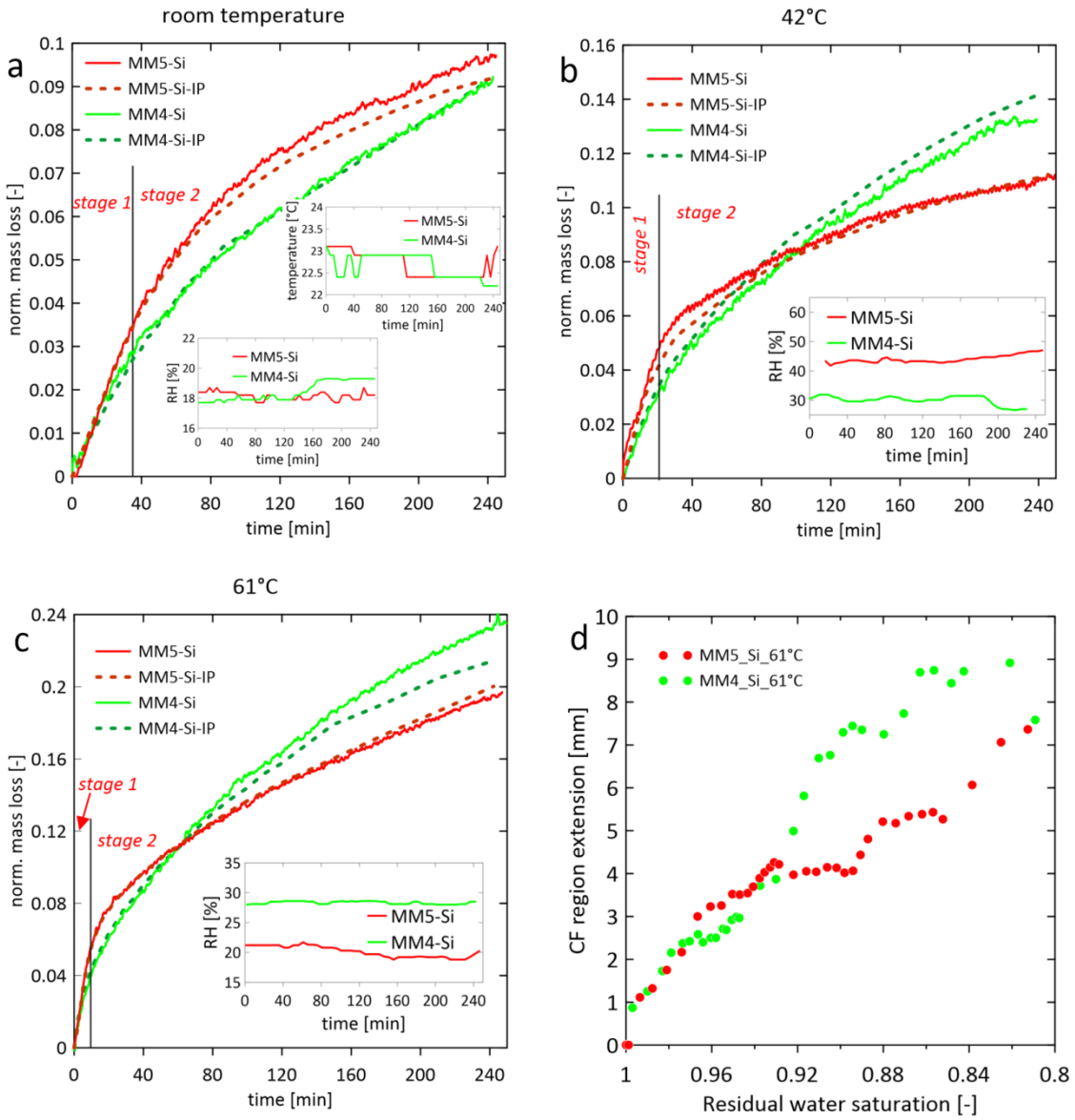

Figure 4. 27 Normalized time-dependent mass loss curves of MM4-Si and MM5-Si in (a) RT, (b) 42 °C, and (c) 61 °C, and (d) the corner flow extension as function of residual water saturation (61°C). Mass loss data derived from digital balance measurements and image processing are indicated by solid and dashed colored lines, respectively. The insets show the ambient temperature and RH during the experiments.

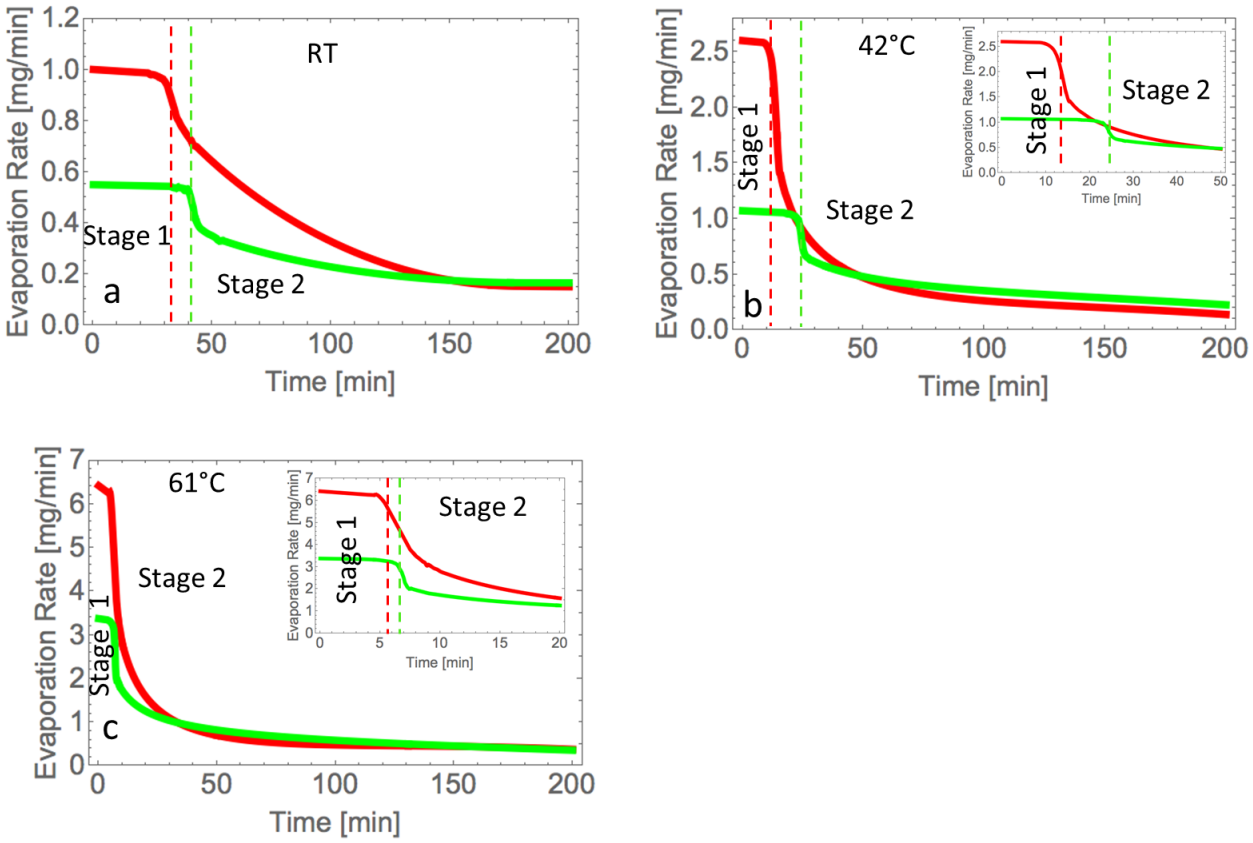

Figure 4. 28 Time-dependent evaporation rate curves of MM4-Si and MM5-Si at (a) RT, (b) 42 °C, and (c) 61 °C. The green curves represent evaporation rate Q_{ev} of MM4-Si with the detachment time t_c marked by green dashed lines. The red curves represent Q_{ev} of MM5-Si with t_c marked by red dashed lines. The insets show stage 1–stage 2 transitions.

4.8 Suppression on Evaporation Caused by the Fractal Displacement (Percolation) Front

The time-dependent mass loss curves of MM4-glass and MM5-glass at the three temperatures are shown in Fig. 4.29 with inserted experimental RH and ambient temperature figures. As shown in Fig. 4.17, in both MM4-glass and MM5-glass, the thick-film flow covers a large region and maintains the evaporation front close to the open surface. We would expect a similar strong evaporation behavior in MM4-glass as in MM5-glass. However, evaporation is suppressed by the fluctuated and fractal displacement (percolation) front in MM4-glass (Fig. 4.17). The flat and compact displacement in MM5 results a stable vapor concentration gradient from the displacement front to the open surface. While in MM4, the most advancing displacement regions continue to grow for a relatively long period, making the air invasion

fingers being embraced by saturated regions on the lateral sides, which suppresses the vapor diffusion in some directions. And the cumulated vapor molecules in the advancing regions further suppress the water-air displacement.

Since TFF is the dominant mechanism in glass micromodels rather than CF, the CF connectivity of MM4 structure doesn't play a key role.

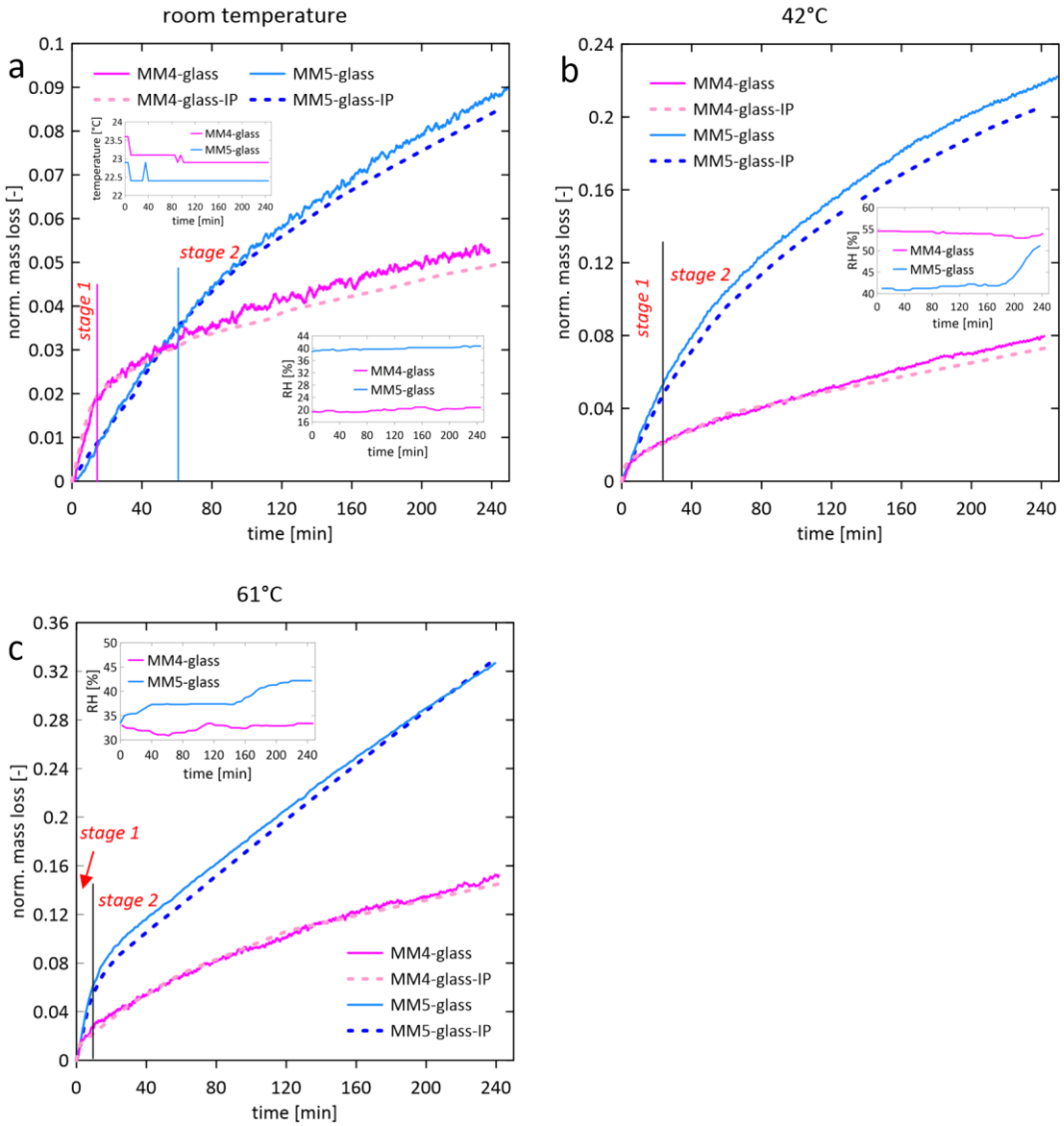

Figure 4. 29 Normalized time-dependent mass loss curves of MM4-glass and MM5-glass in (a) RT, (b) 42 °C, and (c) 61 °C. Mass loss data derived from digital balance measurements and image processing are indicated by solid and dashed colored lines, respectively. The insets show the ambient temperature and RH during the experiments.

4.9 Impact of Gravitational Force on Evaporation

To analyze the impact of gravitational forces on evaporation process, I conducted both vertical ($B_0 > 0$) and horizontal ($B_0 = 0$) evaporation experiments under room temperature with ethanol (ethanol performs fast evaporation in room temperature and displays more significant characteristics within short time). The contact angle of ethanol on the silicon wafer is between 0 (untreated wafer) to 10°C (water treated wafer) as previously discussed in Chap. 3.2, therefore, strong corner flow transport is expected.

In the vertical case, the gravitational forces stabilize the displacement front with a finite extension of corner flow region (Fig. 4.30 a, d). In the horizontal case, both MM5-Si and MM4-Si display unstable and fractal displacement front. The advancing displacement regions keep growing and lead to large air invasion fingers. Large extension of CF region are observed in the horizontal cases and the retarded regions keep the open surface remaining partially wet for a long period (Figs. 4.30 b, c). As a result, gravitational forces ($B_0 > 0$) stabilize the front and slow down the increase of mass loss (Fig. 4.31), as described by the solution of Eq. 2.2.9.

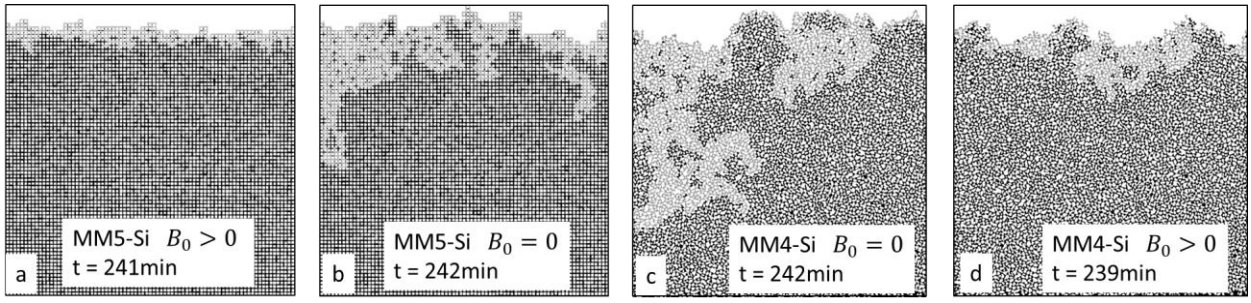

Figure 4. 30 Ethanol evaporation fluid patterns of MM4-Si and MM5-Si at around 4h for horizontal ($B_0 = 0$) and vertical ($B_0 > 0$) cases. The BF regions are displayed in black and CF regions are displayed in grey.

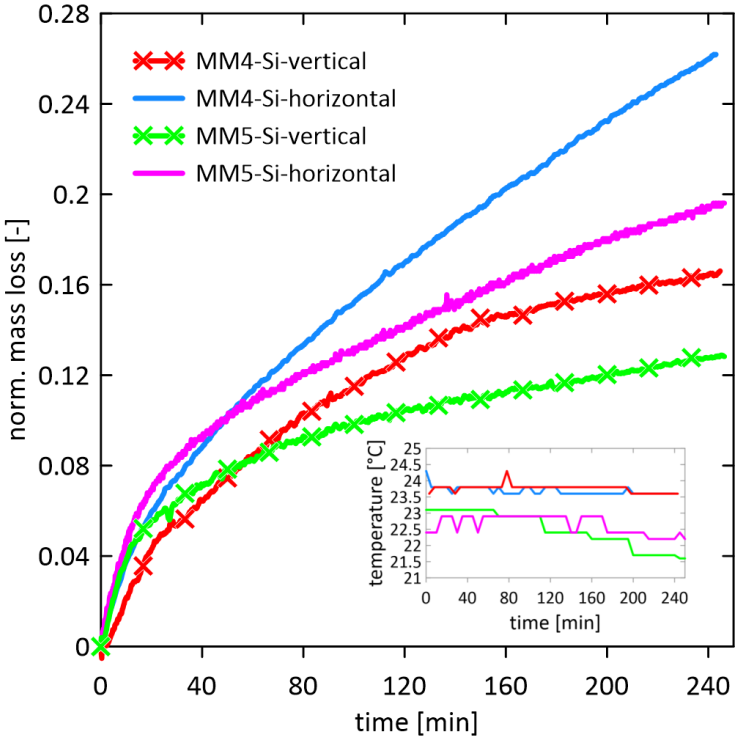

Figure 4. 31 Normalized ethanol mass loss curves of MM4-Si and MM5-Si in vertical and horizontal experiments. The inset shows the ambient temperatures.

4.10 Square Root Behavior of Evaporation in Micromodels

If viscous forces dominate the internal water flow, the viscous length and the mass loss are described by a diffusion-like $\sqrt{t}$-behavior as described by the desorption theory in Brutsaert and Chen (1995). A $\sqrt{t}$-behaviour with high statistical significance is observed (regression coefficients near 1) for all micromodels (Fig. 4.12 and Fig. 4.32), which gives answer for the problem 7 listed in Chapter 1, that, our experimental data derived from 2D micromodels are realistic results, and the 2D micromodels which allow good visualizations of multiphase flow dynamics at pore scale can be good representatives of soil.

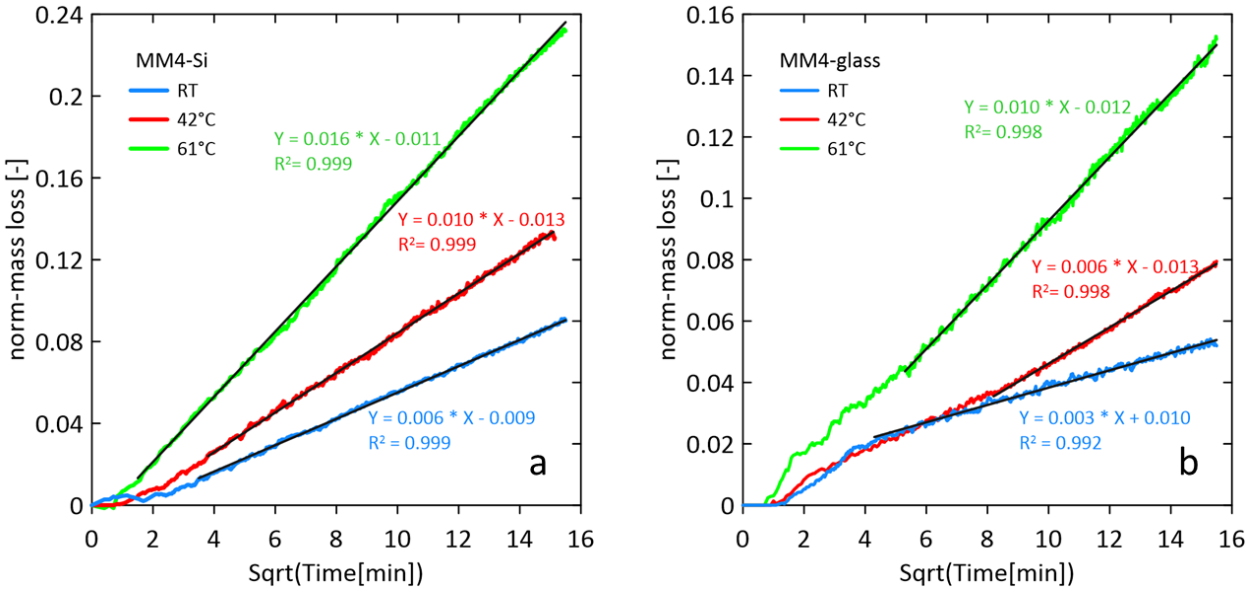

Figure 4. 32 Mass loss versus $\sqrt{t}$. The experimental data shows square-root behavior of stage 2 evaporation for MM4-Si and MM4-glass. The regression coefficient R^2 is approximately 1 for all fits.

4.11 Insights for Soil Treatments to Reduce Soil Water Evaporation

In the real soil system, water exists as gravitational water, capillary water or hygroscopic water (Fig. 4.33). The pores in soil are saturated after water infiltration, but water in the macropores (larger than 0.08mm; Easton and Bock, 2016) will drain out rapidly due to the gravitational pull, this free water is called the gravitational water and hardly for plant use. The rest water (named as capillary water) is held in the smaller pores because the capillary forces are stronger than the gravitational forces, and the corresponding water content defines the field capacity of the soil. The capillary water is capable of moving within the soil and carries dissolved nutrients, which is the main water available for plants use. Soil moisture is reducing because of evaporation and water uptake by root, below the wilting point (the minimum amount of water required by plants to avoid wilting), the retained water is bound tightly to the soil particle surface by adhesion in the form of hygroscopic water and no longer available for plant use. Therefore, the soil treatment should be aimed to largely minimize the evaporation of the capillary water in soil.

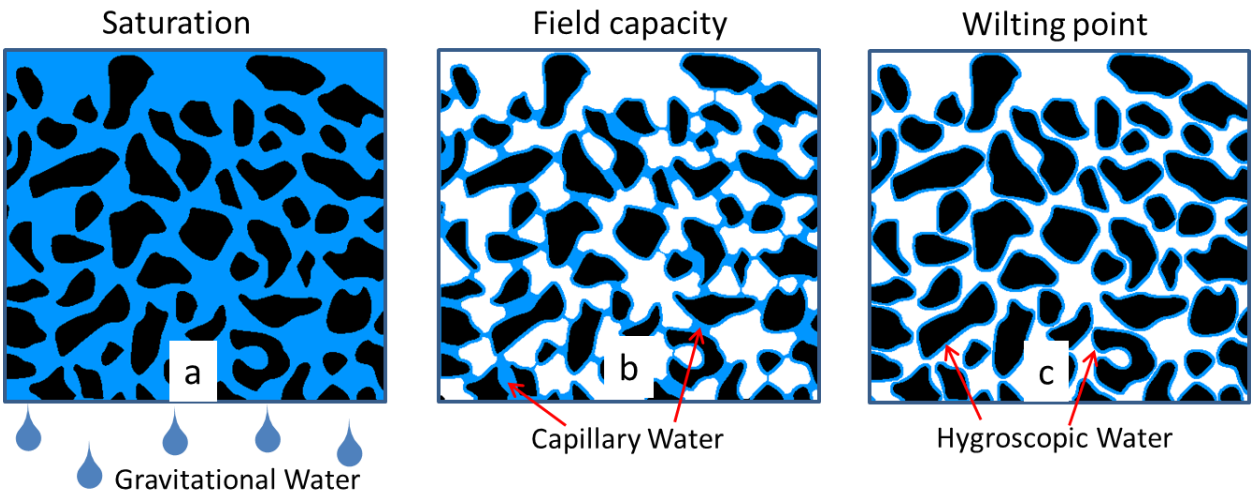

Figure 4. 33 The three types of soil water: (a) the gravitational water, (b) the capillary water and (c) the hygroscopic water.

Gupta et al. (2015) designed an experiment in which a layer of hydrophobic soil (organo-silane treated) was laid on the surface of normal hydrophilic soil. Compared to the evaporation from the uncovered ordinary soil, the cumulative water mass loss was reduced by 77.5%, 89.6% and 92.8% with the soil configurations of 1cm, 2cm and 3cm thickness of hydrophobic soil layer, respectively. Furtherly, the greater water retention due to the hydrophobic soil layer was proved to promote the growth of chick pea plants, referring the length of roots, height of shoot, number of branches, number of leaves, number of secondary roots, biomass etc. To explain those experimental results from the aspect of evaporation mechanism, it is clear that, the hydrophobicity disables the capillary flow (corner flow and thick-film flow) in this soil layer and cuts off the hydraulic connectivity to the soil surface, as a result, evaporation only occurs by vapor diffusion. This concept of water retention by placing a few centimeter layer of hydrophobic soil can be beneficial for crops grown underground, as the traditional plastic mulching method for reducing soil evaporation may cause unexpected soil temperature increase and the disposal issue after use. However, the hydrophobicity of soil will also reduce the rainfall infiltration (Jamison 1945; Jamison 1947), especially the initial intake rate is greatly influenced by the wettability of soil (Letey et al., 1962b), which may cause runoff if the rainfall cannot be adsorbed by soil.

Assume a soil pore structure (coarse sand) represented by MM4, the gravitational water will drain out from the macropores and the capillary water will mostly retain in the pore throats (Fig. 4.33b). Due to the corner flow and thick-film flow, the discrete capillary water clusters in pore throats form a continuous

hydraulic active network, which enables the water transport inside the soil pores and promote evaporation. The order of capillary water clusters to get dry is determined by the capillary resistances, which may cause heterogeneous residual water distribution inside the soil if the soil has a heterogeneous texture. With the absence of corner flow and thick-film flow, the retained water clusters in pore throats would be isolated and evaporate only by vapor diffusion, which is a rather slow process for the vapor molecules in the deep soil section to go through the highly tortuous pass to the soil surface. Therefore, creating a soil condition which enables least corner flow and thick-film flow is beneficial for water retention.

The appearance of corner flow must satisfy the geometric relation $\theta < (\pi - \alpha)/2$, where α is the corner angle and θ is the contact angle. The corner angles inside soil are hard to manipulate, hence, increasing the contact angle θ can be a concept to reduce corner flow appearance. The thick-film flow is caused by the complete wetting behavior of rough surface, with the precondition given in Eq.4.5.1, that is, the intrinsic contact angles θ_0 must be smaller than the critical value θ_c (= 60°; the grooves are approximated by equilateral triangles as shown in Fig.4.14). It is difficult to create a high degree of smoothness for soil grains surfaces, therefore, increasing the intrinsic contact angle is an optional concept also for reducing the thick-film flow. The hydrophobic soil may reduce the rainfall infiltration (Jamison 1945; Jamison 1947), as a result, a non-destructive soil treatment for the top soil layer to achieve a contact angle between 60° to 90° can be an optional concept for soil water retention. But the practicality and operability of this concept needs to be proved furtherly by lab and field experiments.

5 SSC-Model Application

I tested the SSC model for evaporation of water and ethanol, under different temperatures, for horizontal and vertical cases, with both MM5-Si and MM4-Si where corner flow is dominant for evaporation.

5.1 Input Mass Loss Data and Capillary Width Renormalization

As the SSC-model considers ***single*** square capillary, I assumed the number of capillaries in a micromodel equal to the number of pores at open surface, the original mass loss data and evaporation flux Q_{ev} were renormalized to one effective capillary. MM5 has 79 capillaries (80 grain particles) at the open surface, the average capillary width of 292 μm and the known depth of 300 μm give an equivalent width d_0 of the square capillary equal to 296μm (Fig. 2.4). In MM4, there are 91 capillaries (pore throats) at the first layer of grains. The average pore throat width (marked in yellow in Fig. 5.1) is 265 μm, which results an equivalent square capillary width d_0 of 282 μm.

Figure 5. 1 The equivalent square capillary width d_0 of MM4 is determined by the pore throats of the first layer grains (marked in yellow).

5.2 Parameter Sensitivity Analysis

The mass loss deviation between the analytical and experimental data is related to the contact angle input for mass loss calculation, which is the θ_{t_c} derived by detachment time t_c extrapolation (Fig. 2.8 & 2.10). Taking the horizontal water evaporation at room temperature (t = 8000s) as an example, the mass loss deviation stays constant when θ_{t_c} is below 35° and abruptly drops to 0 when θ_{t_c}= 39° (Fig. 5.2a). The mass loss deviation occurs in Stage 2, and the analytical mass loss of stage 2 is determined by the parameters a_3, a_4 and evaporation front depth x_i (see Eq. 2.2.24a). The parameters a_3 and a_4 show the

similar tendency (as function of contact angle; Fig. 5.2c, d) as the mass loss deviation in Fig. 5.2a, among which, a_4 is 4 orders of magnitude larger than a_3. The absolute dominant parameter a_4 is determined by the parameters a_0, a_1 and a_2 (see Eq.2.2.24c). The a_0 is contact angle independent, while a_1/a_2 displays the same tendency as a_4 and quantitatively responsible for a_4 (Fig. 5.2f). Separating a_1/a_2 into two sensitivity factors, i.e. a_1 and $1/a_2$, the $1/a_2$ (Fig. 5.2h) turns to be the controlling factor with the same tendency as a_1/a_2. Exclude the non-adjustable physical parameters in the a_2 determination (Eq.2.2.23b), the uncertain parameters include the cross sectional area of square capillary A_g^0 and the curvature radius of corner flow r_p (Eq. 2.2.2a), which are both dependent on the capillary width d_0. Therefore, the capillary width d_0 is the most sensitive parameter of the SSC-model for stage 2 mass loss calculation.

The equivalent square capillary width d_0 is initially given by the geometrical data of the micromodels. The initial d_0 describes the early stage case where all the pores at open surface are wet and "active" for evaporation. While in stage 2, due to the capillary pumping from larger pores to smaller pores, the smaller pores are kept wet at the open surface and "active" for evaporation. Therefore, by adjusting the initial d_0 with a factor between 0 and 1, we found the best fitting factor of 0.65 and an effective capillary width $d_{eff} = 192\ \mu m$ for MM5-Si, and the best fitting factor of 0.63 and an effective capillary width $d_{eff} = 178\ \mu m$ for MM4-Si. Note that, the modeling results shown below were applied with the effective capillary width d_{eff} instead of initial capillary width d_0.

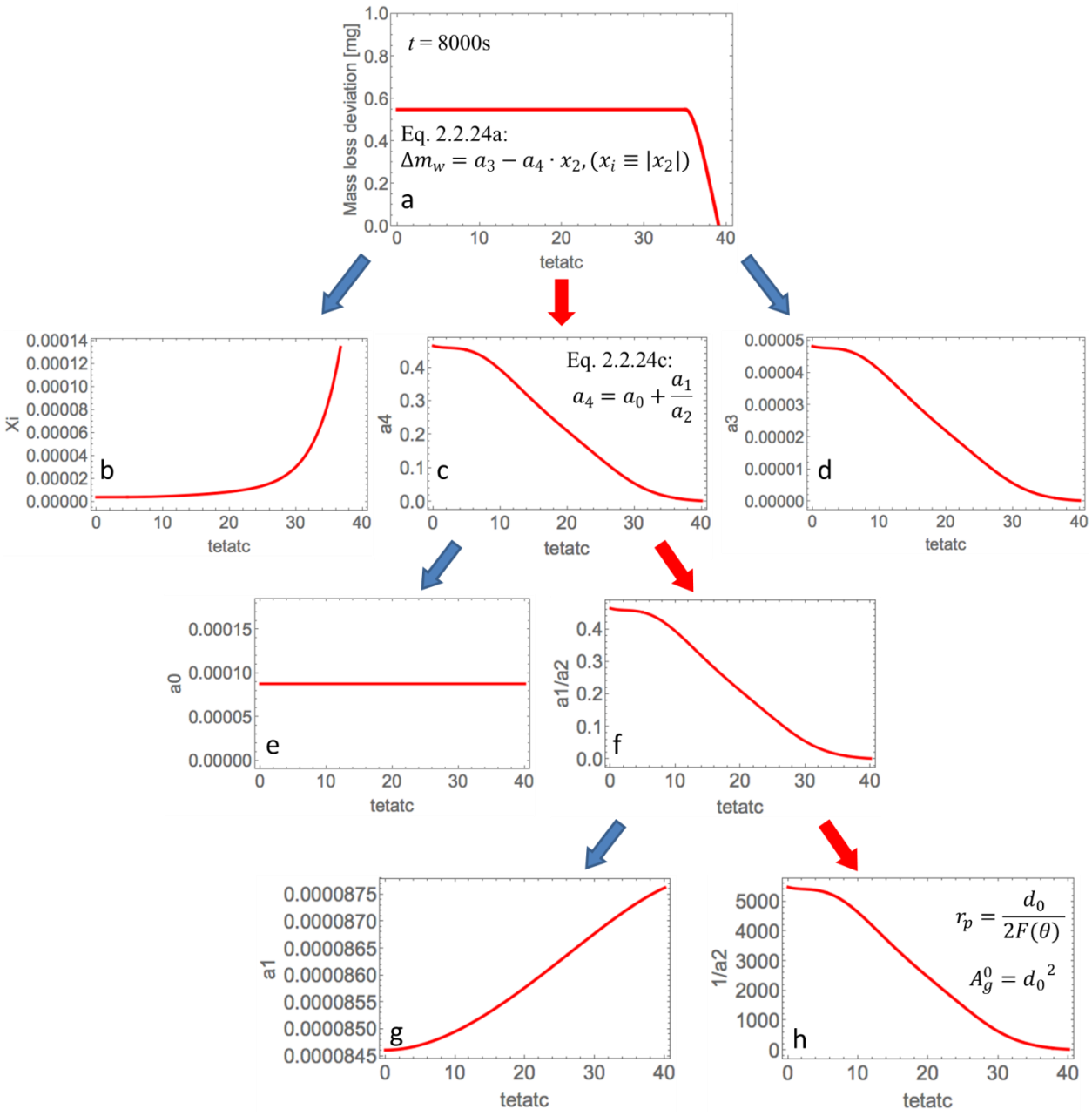

Figure 5. 2 SSC-model parameter sensitivity analysis workflow, the most sensitive parameter d_0 is deduced by the path marked by red arrows. The contact angle θ_{t_c} dependencies of (a) the mass loss deviation between the analytical and experimental data; (b) the mean evaporation front depth x_i; (c) the parameter a_4; (d) the parameter a_3; (e) the parameter a_0; (f) the ratio of parameter a_1 over a_2; (g) the parameter a_1 and (h) the reciprocal of parameter a_2.

5.3 The Contact Angle Dependency of Cross-sectional Area of Corner Flow

The cross sectional area of corner flow is highly dependent on contact angle. For a given interfacial curvature, the interface of corner flow is forced further into the corner when the contact angle θ increases, thereby reducing the cross-sectional area available for corner flow. The SSC-model verifies the reducing cross sectional area of corner flow $A(\theta)$ with increasing contact angle θ. Fig. 5.3 presents the ratio of $A(\theta)$ over $A(0)$ ($\theta = 0$) for MM5-Si water evaporation. If one neglects the contact angle dependence and simply assumes complete wetting ($\theta = 0$), the relative error is 25.7% when the actual contact angle is 15° and can approach to 75% if the actual contact angle is 30°. Therefore, for any model which doesn't count contact angle as constraint, is theoretically not realistic.

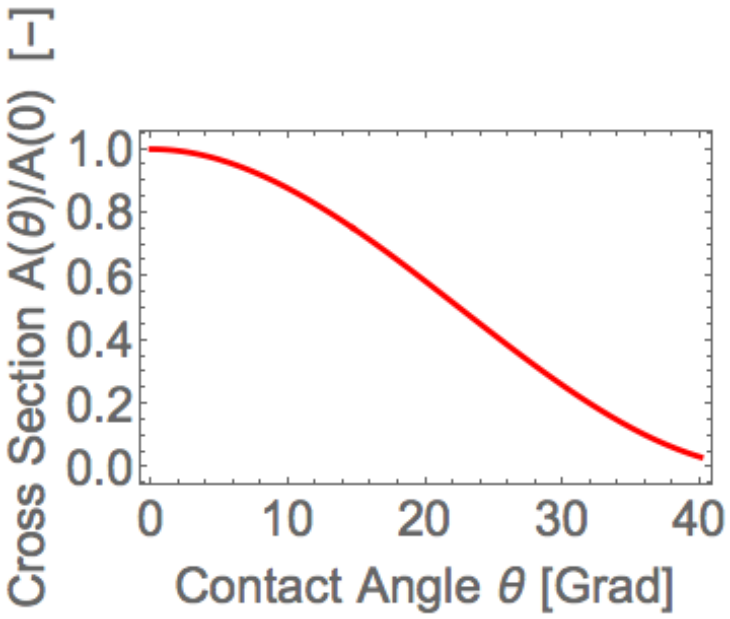

Figure 5. 3 The contact angle dependency of cross sectional area of corner flow $A(\theta)$.

5.4 SSC-model Application Results of Water Evaporation

The mass loss curve versus time $\Delta m(t)$ derived by SSC-model for both horizontal ($B_0 = 0$) and vertical ($B_0 > 0$) cases are displayed below. The corresponding parameters applied in SSC-model for each experiment are listed in Table 5.1. Note that, the experimental data shown below are renormalized data, that is, the mass loss and stage 1 evaporation rate Q_{ev} for ***one effective capillary***. There are two constraints for the model, i.e. the effective capillary width d_{eff} and the detachment time t_c. The x_p and Q_{ev} data applied in the model are the corresponding experimental values taken at $t = t_c$.

For MM4-Si, the model presents good fittings through the entire stages for all temperatures (Fig. 5.4). For MM5-Si, the model has good representatives for both stage 1 and stage 2 behaviors of the room temperature experiments (Fig. 5.5 a, b). The model presents a good fitting of stage 2 for the above-ambient temperature experiments, but displays a relatively short period of stage 1, and the premature transition from stage 1 to stage 2 leads to a lower mass loss than the experimental data during the transition period (Fig. 5.5 c, d).

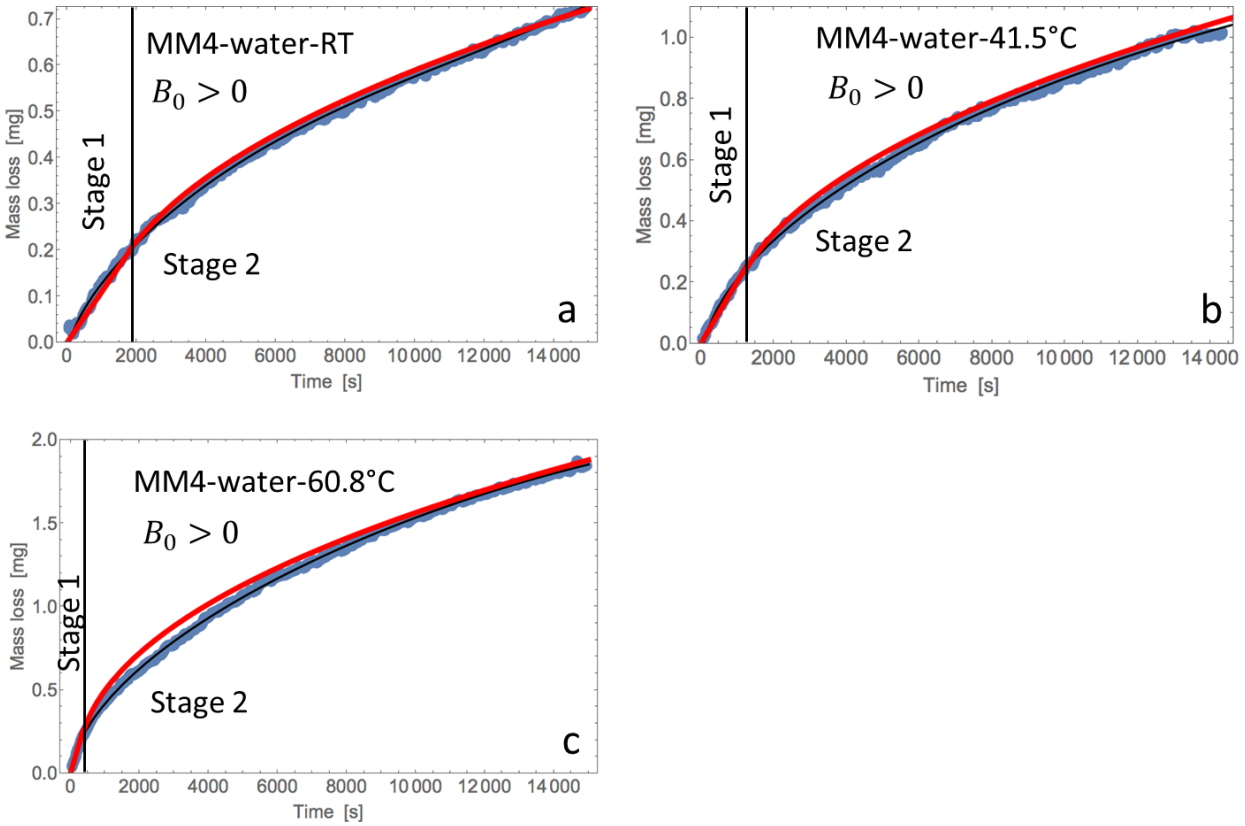

Figure 5. 4 Comparison of the theoretical and experimental mass loss curves of water evaporation of MM4-Si for: (a) vertical experiment at room temperature (Exp.1); (b) vertical experiment at around 42°C (Exp.2); (c) vertical experiment at around 61°C (Exp.3). The red curves represent the theoretical mass loss curves derived by SSC-model, the black curves show the best fit to the experimental data (blue dots). Stage 1 and stage 2 are divided by the black lines.

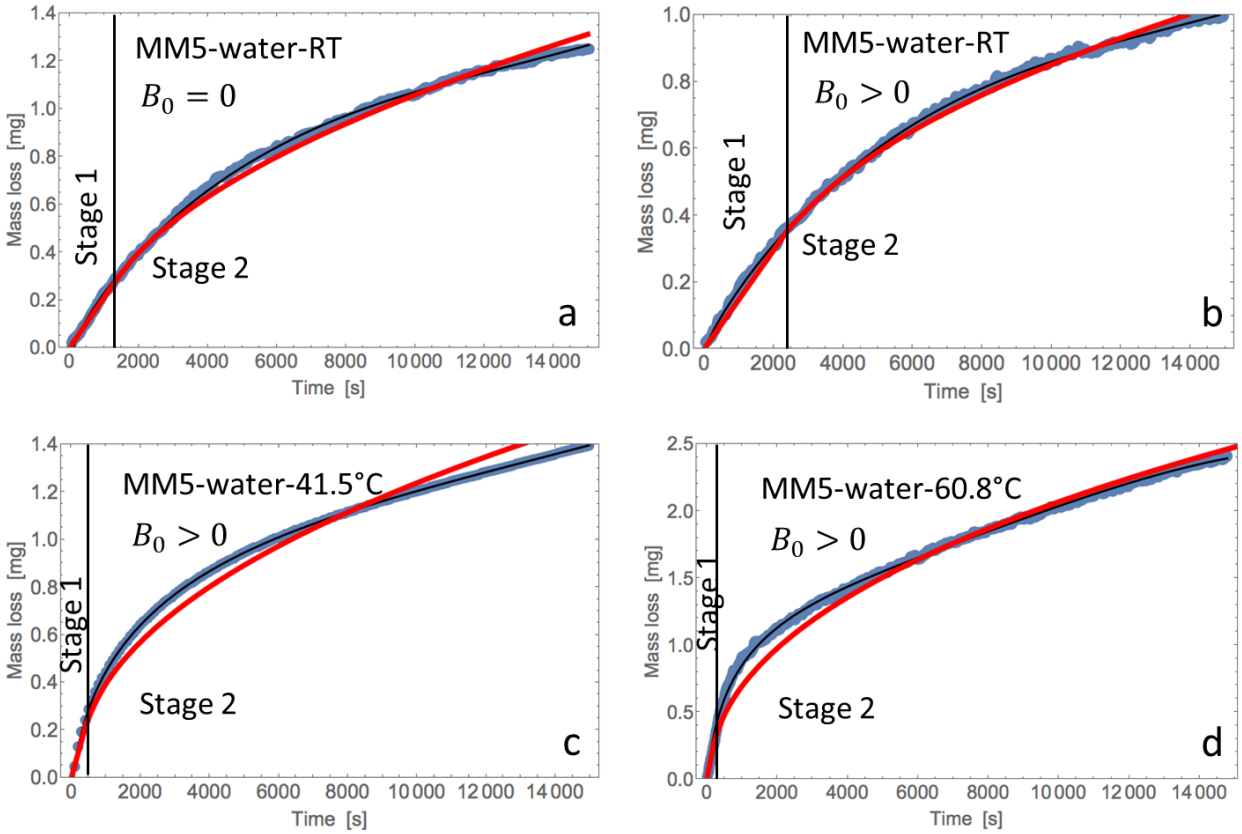

Figure 5. 5 Comparison of the theoretical and experimental mass loss curves of MM5-Si (water evaporation) for: (a) horizontal experiment at room temperature (Exp. 4); (b) vertical experiment at room temperature (Exp.1); (c) vertical experiment at around 42°C (Exp.2); (d) vertical experiment at around 61°C (Exp.3). The red curves represent the theoretical mass loss curves derived by SSC-model, the black curves show the best fit to the experimental data (blue dots). Stage 1 and stage 2 are divided by the black lines.

Note that, the SSC-model is dependent on the mean pore size not the pore size distribution. The mean pore size is represented by an effective capillary width d_{eff}, because the equivalent capillary width d_0 at open surface can only describe the early stage of evaporation when the pores at open surface are all "*active*", in stage 2, evaporation from small capillaries become dominant, the SSC-model would overestimate evaporation rate without applying the proper "*active*" capillary width (Geistlinger et al., 2019).

The theoretical contact angles derived by SSC model are listed in Table 5.1, which yields an overall mean contact angle of 32.95 $\pm$ 4.35° for water. The consistency of the theoretical contact angle and

experimental measurement (35.5°; Chap.3.2) demonstrates the validity of the θ-dependent SSC model. The contact angle extrapolations from x_p and t_c are independent, the θ_{x_p} has relatively higher values than θ_{t_c} with maximum deviation of 4.6° (5.1% < relative error < 13.8%). This error is caused by the actual tortuous path of the corner flow in micromodels (Fig. 4.2d), while the model describes a straight path in a capillary (Geistlinger et al., 2019). The applied x_p data in the model (derived by geometrical averaging with IP method) is supposed to be smaller than the realistic x_p, which yields a higher θ_{x_p}. Therefore, θ_{t_c} was applied for the mass loss curve modeling.

Table 5. 1 The applied parameters of water evaporation experiments for SSC modeling.

Water Exp.	B_0	T [°C]	RH [%]	BL [mm]	d_{eff} [um]	t_c [s]	Xp [mm]	Qev* 10^{-4} $[mg/s]$	θ_{xp} [°]	θ_{tc} [°]
MM5-RT-hori	$= 0$	20.3	36.9	0.04	192	1350	2.894	2.1	36.3	33
MM5-RT	> 0	21.7	36.3	0.062	192	2370	2.875	1.48	37.3	33.3
MM5-40	> 0	42	44.2	0.05	192	400	1.3	5.27	37.1	32.1
MM5-60	> 0	60.8	20.1	0.075	192	160	2.3	13.5	33.2	28.6
MM4-RT	> 0	22.6	18.4	0.093	178	1800	3.46	1.1	37	35.1
MM4-40	> 0	42	29.9	0.137	178	1200	3.57	2.02	36.2	33.6
MM4-60	> 0	60.8	28.3	0.105	178	330	3.33	7.14	33.3	29.7

5.5 SSC-model Application Results of Ethanol Evaporation

The mass loss curve versus time $\Delta m(t)$ derived by SSC-model for the ethanol evaporation (horizontal case), at room temperature, for both MM4-Si and MM5-Si are displayed in Fig 5.6. The corresponding parameters applied in SSC model of each experiment are listed in Table 5.2. The RH corresponds to the ethanol gas concentration in the experimental ambient, which was assumed to be 0. The model achieves good representations of both stage 1 and stage 2 behaviors for MM4-Si (Fig. 5.6b), note that, the theoretical curve was derived with the original experimental parameters. While for MM5-Si, the model presents a good fitting of stage 2 but a relatively short period of stage 1, and a lower theoretical mass loss than the experimental data during the stage 1-stage 2 transition period (Fig. 5.6a). The theoretical contact angles derived by SSC model (Table 5.2) yields a mean contact angle θ_{t_c} of 11.2° for ethanol, in consistency with the measured value around 9° (Chapter 3.2).

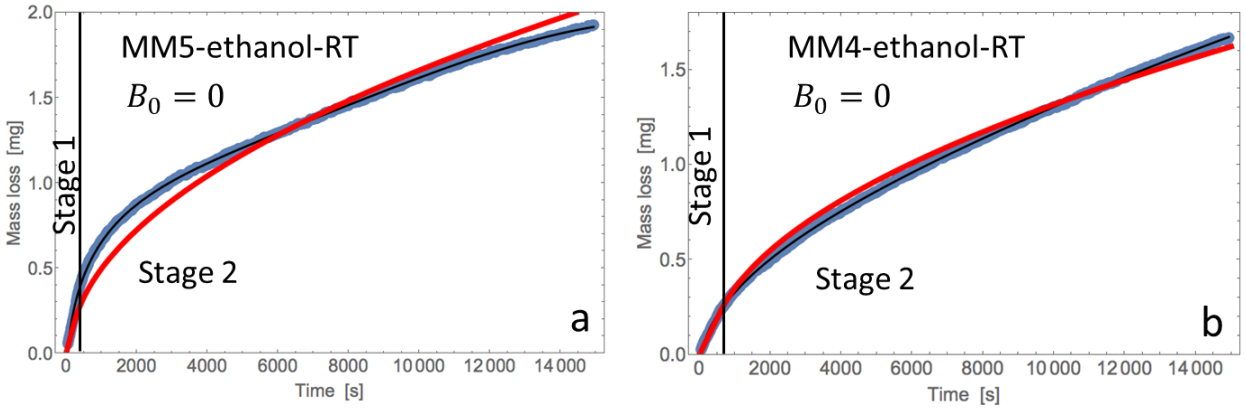

Figure 5. 6 Comparison of theoretical and experimental mass loss curves of ethanol evaporation in horizontal direction at room temperature for: (a) MM5-Si and (b) MM4-Si. The red curves represent the theoretical mass loss curves derived by SSC-model, the black curves show the best fit to the experimental data (blue dots). Stage 1 and stage 2 are divided by the black lines.

Table 5. 2 The applied parameters of ethanol evaporation experiments for SSC modeling.

Ethanol Exp.	B_0	T [°C]	RH [%]	BL [mm]	d_{eff} [um]	t_c [s]	Xp [mm]	Qev* 10^{-4} $[mg/s]$	θ_{xp} [°]	θ_{tc} [°]
MM5-RT-hori	$= 0$	22.6	0	0.078	192	222	3.1	7.8	21.1	10.6
MM4-RT-hori	$= 0$	23.7	0	0.14	178	600	3.45	3.8	24.8	11.8

In general, the SSC model gives good agreements between experiments and theory, which furtherly proved the answer of the problem 6 in Chapter 1, that, corner flow is the dominant mechanism of evaporation in MM4-Si and MM5-Si. The soil-alike structure MM4-Si shows better fitting than the artificial regular structure MM5-Si, especially the smooth stage 1-stage 2 transition. This indicates the application of SSC-model can be recommended as an option for the evaporation estimation. This model is independent from the pore size distribution and gives direct quantification of the evaporation component (E), providing new contributions for the listed issues 1 and 3 in Chapter 1 and showing potentials to be applied and incorporated in land surface models and remote sensing estimations.

6 Summary and Conclusions

6.1 Summary

Evaporation is a key component of the global hydrologic cycle, it is necessary to provide reliable quantifications of evaporation for the hydrological and climate models, and water resource management. Many evaporation models only consider the capillary flow through the pore ducts (bulk flow) determined by pore size distribution, e.g. the IPE model introduced in Chapter 2.1, while the retained liquid films in surface roughness (thick-film flow) and angular corners (corner flow) have been found to facilitate and dominate evaporation (Tuller and Or, 2001; Eijkel et al., 2005; Yiotis et al., 2003, 2012). As there is no systematic study on the complex influence of the corner and thick-film flow on evaporation process in the literatures, for the first time, this thesis gives visualizations of the corner and thick-film flow during the evaporation process, and presents the enhanced hydraulic continuity by corner and thick-film flow in evaporation process. The validity of the SSC-model, which assumes corner flow is dominant for the mass transport during evaporation, is tested with 2D micromodel experiments. Since the SSC model gives direct quantification of the evaporation component (E), the good agreements between experiments and theory suggests, the SSC-model can be an option for the evaporation estimation and potentially applied and incorporated in land surface models and remote sensing estimations. The importance of surface roughness on evaporation efficiency is experimentally and theoretically proved in this thesis, that, surface roughness may lead to complete wetting (spontaneous thick-film flow) and largely enlarge the hydraulic connection region. Furthermore, this thesis shows that for a consistent description of the time-dependent mass loss and the geometry of the corner/thick-film flow region, the fractality of the evaporation front must be taken into account. The 2D micromodels allow direct visualization of the multiphase flow dynamics at the fronts, and the viscous length and the mass loss show a diffusion-like $\sqrt{t}$-behavior as described by the desorption theory (Brutsaert and Chen, 1995) with high statistical significance (regression coefficients near 1) for all micromodels, which suggests micromodels can be good representatives of soil in lab studies.

6.2 Specific Results and Conclusions

In this work, evaporation in porous media has been experimentally and numerically addressed by pore-scale and REV scale visualizations and quantifications. I applied 2D micromodels manufactured with two types of materials (silicon vs glass-ceramic), and two types of pore structures (irregular structure MM4 and regular structure MM5). The silicon micromodels contain an ultra-smooth inner surface where only the corner flow (enabled by the geometrical structure of sharp corners) occurs, while the glass-ceramic micromodels contain a rough inner surface where both corner flow and thick-film flow (inside the surface cavities) occur. MM5 is quadratic-lattice pore structure and the geometrical centers of the grain particles are equidistant and connected by lognormal distributed throats with a width $d_{mean} = 400 \pm 62\mu m$. The irregular pore structure MM4 was derived by a 3D-2D topological mapping algorithm and is the representative for real soil. Although MM4 has a similar mean pore radius of 205 μm as MM5, the irregular pore structure causes a wider pore size distribution, especially the tiny pore throats in the range of 50-100 μm. The focus of the experiments is to display the impacts of surface roughness, fractality of fronts, and pore structures on evaporation.

A series of water and ethanol evaporation experiments were conducted vertically ($B_0 > 0$) and horizontally ($B_0 = 0$) at three temperatures (room temperature, 42°C and 61°C), with the process being monitored by a DSLR camera and the mass measured by a high-precision digital balance. Fluorescence microscopy was also applied to give good visualizations of the corner flow, thick-film flow, and the liquid transport between different capillary flows during evaporation.

Furthermore, I tested the extended SSC-model (Geistlinger et al., 2019) with silicon micromodel experiments. The SSC-model describes very well of the evaporation process from square capillary with smooth surface, where corner flow transport is dominant. The contact angle dependence on evaporation process is derived by the inverse modeling.

The main conclusions of the experimental study are:

1. The answer of problem 6 in Chap.1 is clear, that, apart from the bulk flow, the corner and thick-film flow also play important role in evaporation. The capillary flow hierarchy between bulk flow (BF), corner flow (CF) and thick-film flow (TFF) is determined by the driving water pressure P_w *(*$P_w = -P_c$*)*. As the curvature radii of the three capillary flows obey the following relationship: $r_{BF} > r_{CF} > r_{TFF}$, the water pressure shows the gradient: $P_{w,BF} > P_{w,CF} > P_{w,TFF}$. In a single pore channel of MM5-glass, bulk flow was observed to disappear first, followed by corner flow, thick-film flow was the last water to dry out. In the silicon micromodels, with the bulk flow

meniscus receding, the water pressure gradient drives water transporting from bulk flow to the open surface through corner flow. In the glass micromodels, thick-film flow spontaneously carpets the whole rough surface, water transports from bulk flow to the open surface through corner flow and thick-film flow.

2. MM5-Si and MM5-glass which possess an identical pore structure show a similar stage1-behaviour, which is controlled by water redistribution through "capillary pumping". If the menisci have receded into the pores, water flow still exists within the pore corners and along the rough pore surfaces. Stage 2 is controlled by the internal water flow and the different driving forces of corner flow and thick-film flow are responsible for the different stage2-behvaiour of the evaporation process. The experimental study shows that the interplay of surface roughness and wettability plays a key role for the time- and temperature behavior of the evaporation process. The weak hydrophilic wettability (contact angle of approximately 35.5°; partial wetting) of the oxidized silicon micromodels causes a weak driving force for the corner flow. This results in a less mass loss and smaller viscous flow length (= extension of the CF-region). As the answer of problem 8 in Chapter 1, surface roughness of the glass-ceramic micromodel causes complete wetting and hence a strong driving force, which results in a higher mass loss and a larger viscous length compared to those of the Si-micromodel. The spontaneous thick-film flow caused by surface roughness keeps the open surface partially wet and prolongs the stage 1 in MM5-glass. Moreover, the thick-film flow maintains the evaporation front close to open surface in stage 2 and leads to a larger mass loss than MM5-Si.

3. There exist a similar $\sqrt{t}$-behavior up to 42° and a transition to linear *t*-behavior for higher temperatures (61°) with high statistical significance (regression coefficients near 1) for both MM5-Si and MM5-glass. Our experimental results elucidate the strong temporal correlation between mass loss and geometric pattern of the unsaturated CF- and TFF-region. Both show a similar time-behavior with high statistical significance. However, MM5-glass exhibits always a stronger increase of the evaporation characteristics (mass loss, extension of the CF/TFF-region) with increasing time and temperature due to the complete wetting and strong driving force. The $\sqrt{t}$-behaviour with high statistical significance is also observed (regression coefficients near 1) in all MM4-Si and MM4-glass experiments. Based on those results, the answer of problem 7 listed in Chapter 1 is obvious, that, the 2D micromodels which allow good visualizations of multiphase flow dynamics at pore scale can be good representatives of soil.

4. The evaporation pore invasion resembles invasion percolation similar to a drainage process, the percolation and evaporation fronts hold the same fractal characteristic as drainage front. The approximated flat evaporation front mentioned in Problem 9 in Chapter 1 is only valid when the pore size distribution is very narrow. For a consistent description of the time-dependent mass loss and the geometry of the CF/TFF-region, one has to take into account the fractality of the evaporation front. A averaged flat evaporation front always lead to a principal inconsistency, which is inherent to the SSC-model as we have shown in Geistlinger et al. (2019).

5. The irregular pore structure has both enhancement and suppression effects on evaporation. As stage 1 is controlled by the water redistribution (capillary pumping) from large pores to small pores, the pore throats of MM4-Si cause higher capillary resistances for air invasion, and lead to a weaker stage 1 evaporation than MM5-Si. In stage2, corner flow becomes the dominant evaporation mechanism in silicon micromodels, it transports water from the saturated region to a position closer to open surface and supply for evaporation. MM4-Si maintains thinner corner flow than MM5-Si due to the small pore throat widths, which leads to a stronger capillary rise and connectivity of corner flow. Besides, the irregular structure MM4 display more fractal evaporation fronts and hence larger front lengths than MM5, which also plays a role to enhance evaporation with a larger cross sectional area $A_{gw}^{fractal}$.

   On the other hand, the irregular structure causes unstable and fractal displacements, which may suppress evaporation. The flat and compact displacement in MM5-glass results a stable vapor concentration gradient from the displacement front to the open surface. While in MM4-glass, the most advancing displacement regions continue to grow for a relatively long period, making the air invasion fingers being embraced by saturated regions on the lateral sides, which suppresses the vapor diffusion in some directions. And the cumulated vapor molecules in the advancing regions further suppresses the water-gas displacement.

6. In the vertical case ($B_0 > 0$), the gravitational forces stabilize the displacement front and bulk flow sustains a certain extension of corner flow region. In the horizontal case ($\mathrm{B}_0 = 0$), the advancing displacement sections prefer to keep growing and lead to large air invasion fingers, bulk flow sustains a large extension of corner flow region and keeps the open surface remaining partially wet for a long period. As a result, evaporation is enhanced when gravitational force is absent compared to the vertical case $B_0 > 0$.

7. To reduce the soil capillary water evaporation by eliminating the corner flow and thick-film flow, a non-destructive soil treatment of the top soil layer to achieve a contact angle between 60° to 90° can be an optional concept.

The main conclusions of the SSC-model applications for MM4-Si and MM5-Si are:

1. The capillary width d_0 is the most sensitive parameter of the SSC-model for stage 2 mass loss estimation. The mean capillary width at open surface (given by the micromodel geometry) describes the early stage case when all the pores at open surface are wet and "active" for evaporation, while for stage 2, a smaller pore width dominates the evaporation process due to the capillary pumping. The input effective capillary width $d_{eff} = 192\ \mu m$ of MM5-Si and $d_{eff} = 178\ \mu m$ of MM4-Si give the best fittings between the analytical and experimental mass loss curves.

2. For water evaporation, the SSC-model gives good agreements between the analytical and experimental mass loss curves of MM4-Si, through the entire stages, for all experimental temperatures. For MM5-Si, the model has good fittings of both stage 1 and stage 2 for the room temperature experiments in both vertical and horizontal cases. Those results give answer to the problem 8 in Chapter 1, that, corner flow is the dominant mechanism of evaporation in MM4-Si and MM5-Si. The model also has good representations of the stage 2 behavior for the 42°C and 61°C experiments, but displays a relatively short period of stage 1, the premature transition from stage 1 to stage 2 leads to a lower mass loss than the experimental data during the transition period. For the ethanol evaporation (room temperature), the model has good representations of both stage 1 and stage 2 behaviors for MM4-Si. While for MM5-Si, the model presents a good fitting of stage 2 but a relatively short period of stage 1, and a lower analytical mass loss than the experimental data during the stage 1-stage 2 transition period. In general, the soil-alike structure MM4-Si shows better fitting than the artificial regular structure MM5-Si, especially the smooth stage 1-stage 2 transition. This means the application of SSC-model can be recommended as an option for the evaporation estimation. This model gives direct quantification of the evaporation component (E), providing new contributions for the listed issues 1 and 3 in Chapter 1 and showing potentials to be applied and incorporated in land surface models and remote sensing estimations.

3. The SSC-model verifies the reducing cross sectional area of corner flow $A(\theta)$ with increasing contact angle θ. If one neglects the contact angle dependence and simply assume complete wetting ($\theta = 0$), the relative error can approach to 75% when the actual contact angle is 30°. Therefore, for any model which doesn't count contact angle as constraint, is theoretically not realistic. The contact angle is derived by the extrapolations from x_p and t_c independently. The SSC-model yields an overall mean contact angle of $32.95 \pm 4.35°$ for water and a mean contact angle of 11.2° for ethanol on the Si-SiO_2 wafer, the consistency of the theoretical contact angles and the experimental measurements (35.5° of water and 9° of ethanol) demonstrates the validity of the θ-dependent SSC model. The contact angle θ_{xp} derived from x_p data has higher values than the contact angle θ_{tc} derived from t_c data, the error is caused by the actual tortuous path of the corner flow in micromodels, which is larger than the x_p value applied in the model assuming a straight path in a capillary.

References

Abolafia-Rosenzweig, R., Badger, A.M., Small, E.E. & Livneh, B. (2020). A continental-scale soil evaporation dataset derived from Soil Moisture Active Passive satellite drying rates. Scientific Data, 7, 406. https://doi.org/10.1038/s41597-020-00748-z

Allen, R. G., Pereira, L. S., Raes, D., and Smith, M. (1998). Crop evapotranspiration: Guidelines for computing crop requirements. Irrigation and Drainage Paper No. 56, FAO, Rome, Italy.

Allen, R.G., Tasumi, M., Morse, A., Trezza, R., Wright, J.L.; Bastiaanssen, W., Kramber, W., Lorite, I., Robison, C.W. (2007). Satellite-Based Energy Balance for Mapping Evapotranspiration with Internalized Calibration (METRIC)-Applications. J. Irrig. Drain. Eng., 133, 395–406. DOI: 10.1061/(ASCE)0733-9437(2007)133:4(395)

Anbari, Alimohammad; Chien, Hung-Ta; Datta, Sujit S.; Deng, Wen; Weitz, David A.; Fan, Jing (2018). Microfluidic Model Porous Media: Fabrication and Applications. Small, 1703575–. doi:10.1002/smll.201703575

Anderson, M.C., Norman, J.M., Diak, G.R., Kustas, W.P., Mecikalski, J.R. (1997). A Two-Source Time-Integrated Model for Estimating Surface Fluxes Using Thermal Infrared Remote Sensing. Remote Sens. Environ., 60, 195–216. https://doi.org/10.1016/S0034-4257(96)00215-5

Baldocchi, D., et al. (2001). FLUXNET: A new tool to study the temporal and spatial variability of ecosystem–scale carbon dioxide, water vapor, and energy flux densities. Bulletin of the American Meteorological Society, 82, 2415–2434. https://doi.org/10.1175/1520-0477(2001)082<2415:FANTTS>2.3.CO;2

Balugani, E.; Lubczynski, M.W.; van der Tol, C.; Metselaar, K. (2018). Testing three approaches to estimate soil evaporation through a dry soil layer in a semi-arid area. Journal of Hydrology, 567,405-419. doi:10.1016/j.jhydrol.2018.10.018

Bastiaanssen, W.G.M., Menenti, M., Feddes, R.A., Holtslag, A.A.M. (1998). A remote sensing surface energy balance algorithm for land (SEBAL). 1. Formulation. J. Hydrol. 212–213, 198–212. doi:10.1016/s0022-1694(98)00253-4

Bico, J., Tordeux, C., & Quéré, D. (2001). Rough wetting. Europhysics Letters, 55(2), 214–220. https://doi.org/10.1209/epl/i2001-00402-x

Blunt, M. J., & Scher, H. (1995). Pore-level modeling of wetting. *Physical Review E*, 5, 6387–6403 https://doi.org/10.1103/PhysRevE.52.6387

Bogovic, J. A., Hanslovsky, P., Wong, A., & Saalfeld, S. (2016). Robust registration of calcium images by learned contrast synthesis. 2016 IEEE 13th International Symposium on Biomedical Imaging (ISBI). doi:10.1109/isbi.2016.7493463

Brutsaert, W., and Chen, D. (1995), Desorption and the two Stages of Drying of Natural Tallgrass Prairie, Water Resour. Res., 31(5), 1305– 1313, doi:10.1029/95WR00323.

Brücher, M. and Bottlinger, M. (2006), Dreidimensionale Computersimulation zur Untersuchung von Partikelschüttungen aus unregelmäßig geformten Partikeln. Chemie Ingenieur Technik, 78: 727-733. https://doi.org/10.1002/cite.200500185

Burt, C.M., Mutziger, A.J., Allen, R.G., Howell, T.A. (2005). Evaporation research: Review and interpretation. Journal of Irrigation and Drainage Engineering, 131(1): 37-58. DOI: 10.1061/(ASCE)0733-9437(2005)131:1(37)

Chomsurin, C., & Werth,C. J. (2003). Analysis of pore-scale nonaqueous phase liquid dissolution in etched silicon pore networks. Water Resources Research, 39 (9), 1265–1275. https://doi.org/10.1029/2002WR001643

Córdova, M., Carrillo-Rojas, G., Crespo, P., Wilcox, B., and Célleri, R. (2015). Evaluation of the Penman-Monteith (FAO 56 PM) Method for Calculating Reference Evapotranspiration Using Limited Data. Mountain Research and Development, 35(3), 230-239. https://doi.org/10.1659/MRD-JOURNAL-D-14-0024.1

de Gennes, P. G. (1985). Wetting: Statics and dynamics. Reviews of Modern Physics, 57(3), 827–863. https://doi.org/10.1103/RevModPhys.57.827

Ding, Y., & Geistlinger, H. (2021). Impact of surface roughness on evaporation in 2D micromodels. Water Resources Research, 57, e2021WR029861. https://doi.org/10.1029/2021WR029861

Dong, M., & Chatzis, I.(1995).The imbibition and flow of a wetting liquid along the corners of square capillary tube. Journal of Colloid and Interface Science, 172(2), 278–288. https://doi.org/10.1006/jcis.1995.1253

Dortmund Data Bank. [online] Available at: www.ddbst.com [Accessed in 2021]
Dougherty, R., & Kunzelmann, K. (2007). Computing Local Thickness of 3D Structures with ImageJ. Microscopy and Microanalysis, 13(S02), 1678-1679. doi:10.1017/S1431927607074430
Dullien, F. A. L., Zarcone, C., McDonald, I. F., Collins, A. and Bochard, R. D. E. (1989) The effect of surface roughness on the capillary pressure curves and the heights of capillary rise in glass bead packs. Journal of Colloid and Interface Science,127 (2), 362. https://doi.org/10.1016/0021-9797(89)90042-8
Easton, Z.M., & Bock, E. (2016). Soil and soil water relationships. Virginia Cooperative Extension, March, BSE-194P, http://hdl.handle.net/10919/75545
Eijkel, J. C. T.; Dan, B.; Reemeijer, H. W.; Hermes, D. C.; Bomer, J. G.; van den Berg, A. (2005). Strongly Accelerated and Humidity-Independent Drying of Nanochannels Induced by Sharp Corners. Physical Review Letters, 95(25), 256107–. doi:10.1103/PhysRevLett.95.256107
Engineering ToolBox, (2001). [online] Available at: https://www.engineeringtoolbox.com [Accessed in 2021]
Geistlinger, H., Ataei-Dadavi, I., Mohammadian, S., & Vogel, H. J. (2015). The impact of pore structure and surface roughness on capillary trapping for 2-D and 3-D porous media: Comparison with percolation theory. Water Resources Research, 51, 9094–9111. https://doi.org/10.1002/2015WR017852
Geistlinger, H., Ataei-Dadavi, I., Vogel, H.J. (2016). Impact of surface roughness on capillary trapping using 2D-micromodel visualization experiments. Transport in Porous Media, 112, 207-227. https://doi.org/10.1007/s11242-016-0641
Geistlinger, H., Ding, Y., Apelt, B., Schlüter, S., Küchler, M., Reuter, D., et al. (2019). Evaporation study based on micromodel experiments: Comparison of theory and experiment. Water Resources Research, 55, 6653–6672. https://doi.org/10.1029/2018WR024647
Geistlinger, H. and Leuther, F. (2018), Evaporation Study for Real Soils Based on HYPROP Hydraulic Functions and Micro-CT-Measured Pore-Size Distribution. Vadose Zone Journal, 17: 1-17 180041. https://doi.org/10.2136/vzj2018.02.0041
Geistlinger, H., & Zulfiqar, B. (2020). The impact of wettability and surface roughness on fluid displacement and capillary trapping in 2-D and 3-D porous media: 1. Wettability-controlled phase transition of trapping efficiency in glass beads packs. Water Resources Research, 56, e2019WR026826. https://doi.org/10.1029/2019WR026826
Ghajarnia, N., Kalantari, Z., Orth, R., & Destouni, G. (2020). Close co-variation between soil moisture and runoff emerging from mul-ti-catchment data across Europe. Scientific Reports, 10(1), 4817. https://doi.org/10.1038/s41598-020-61621-y
Gupta, B., Shah, D.O., Mishra, B., Joshi, P.A., Gandhi, V.G., Fougat, R.S. (2015). Effect of top soil wettability on water evaporation and plant growth. J Colloid Interface Sci. Jul 1;449:506-13. doi: 10.1016/j.jcis.2015.02.018. Epub 2015 Mar 6. PMID: 25801650.
Hu, H., Weibel, J.A., Garimella, S.V. (2020). Role of Nanoscale Roughness in the Heat Transfer Characteristics of Thin Film Evaporation. International Journal of Heat and Mass Transfer, 150, https://doi.org/10.1016/j.ijheatmasstransfer.2020.119306
Hyndman R.J. (2011). Moving Averages. International Encyclopedia of Statistical Science. https://doi.org/10.1007/978-3-642-04898-2_380
ISO-standard: International Organization for Standardization. (1997). Geometrical product specifications (GPS)—Surface texture: Profile method—Terms, definitions and surface texture parameters (ISO Standard No 4287). Retrieved from https://www.iso.org/standard/10132.html
Jamison, V.C. (1946), The Penetration of Irrigation and Rain Water into Sandy Soils of Central Florida. Soil Science Society of America Journal, 10: 25-29. https://doi.org/10.2136/sssaj1946.03615995001000C00004x
Jamison, V.C. (1947), Resistance to Wetting in the Surface of Sandy Soils Under Citrus Trees in Central Florida and Its Effect Upon Penetration and the Efficiency of Irrigation. Soil Science Society of America Journal, 11: 103-109. https://doi.org/10.2136/sssaj1947.036159950011000C0020x
Kollas, C., Randin, CF., Vitasse, Y., Körner, C. (2014). How accurately can minimum temperatures at the cold limits of tree species be extrapolated from weather station data? Agricultural and Forest Meteorology, 184:257–266. DOI: 10.1016/j.agrformet.2013.10.001

Kustas, W.P., Norman, J.M. Evaluation of Soil and Vegetation Heat Flux Predictions Using a Simple Two-Source Model with Radiometric Temperatures for Partial Canopy Cover. (1999). Agric. For. Meteorol., 94, 13–29. https://doi.org/10.1016/S0168-1923(99)00005-2

Küchler, M., Otto, T., Gessner, T., Ebling, F., & Schröder, H. (2003). Hot embossing for MEMS using silicon tools. International Journal of Computational Engineering Science, 04(03), 609–612. https://doi.org/10.1142/S1465876303001873

Lawrence, D. M., Thornton, P. E., Oleson, K. W. & Bonan, G. B. (2007). The partitioning of evapotranspiration into transpiration, soil evaporation, and canopy evaporation in a GCM: Impacts on land–atmosphere interaction. Journal of Hydrometeorology, 8, 862–880. DOI: 10.1175/JHM596.1

Laurindo, J.B., Prat, M. (1998). Numerical and experimental network study of evaporation in capillary porous media. Drying rates. , 53(12), 2257–2269. doi:10.1016/s0009-2509(97)00348-5

Lehmann, P., Assouline, S., Or, D. (2008). Characteristic lengths affecting evaporative drying of porous media. Physical Review E, 77(5), 056309–. doi:10.1103/PhysRevE.77.056309

Lehmann, P., Merlin, O., Gentine, P., & Or, D. (2018). Soil texture effects on surface resistance to bare-soil evaporation. Geophysical Research Letters, 45, 10,398–10,405. https://doi. org/10.1029/2018GL078803

Lenormand, R., Touboul, E., & Zarcone, C. (1988). Numerical models and experiments on immiscible displacement in porous media. Journal of Fluid Mechanics, 189, 165–187. https://doi.org/10.1017/S0022112088000953

Lenormand, R., & Zarcone, C. (1984). Role of Roughness and Edges during Imbibition in Square Capillaries. Houston, Texas: Society of Petroleum Engineers. https://doi.org/10.2118/13264-MS

Letey, J., Osborn, J., Pelishek, R. E. (1962a). Measurement of liquid-solid contact angles in soil and sand. Soil Science: March - Volume 93 - Issue 3 - p 149-153

Letey, J., Osborn, J., Pelishek, R. E. (1962b). The influence of the water-solid contact angle on water movement in soil. Hydrological Sciences Journal, 7:3, 75-81, DOI: 10.1080/02626666209493272

Levinson, P., Cazabat, A.M., Cohen Stuart, M.A., Heslot, F., Nicolet, S. (1988). The spreading of macroscopic droplets. Rev. Phys. Appl. 23, 1009–1016. https://doi.org/10.1051/rphysap:019880023060100900

Li, Z, Zheng, F-L, Liu, W-Z. (2012). Spatiotemporal characteristics of reference evapotranspiration during 1961–2009 and its projected changes during 2011–2099 on the Loess Plateau of China. Agricultural and Forest Meteorology, 154–155:147–155. https://doi.org/10.1016/j.agrformet.2011.10.019

Merlin, O., Stefan, V. G., Amazirh, A., Chanzy, A., Ceschia, E., Er-Raki, S., et al. (2016). Modeling soil evaporation efficiency in a range of soil and atmospheric conditions using a meta-analysis approach. Water Resources Research, 52, 3663–3684. https://doi.org/10.1002/2015WR018233

Millington, R. J.,and Quirk, J.P. (1961). Transport in porous media [in soil science], Trans. Int. Congr. Soil Sci., 7, 97–106.

Monteith, J. L. (1965). Evaporation and environment. Symposium of the society of experimental biology, 19, 205–234.

Oki, T., & Kanae, S. (2006). Global hydrological cycles and world water resources. Science, 313(5790), 1068–1072. https://doi.org/10.1126/science.1128845

Or, D., & Lehmann, P. (2019). Surface evaporative capacitance: How soil type and rainfall characteristics affect Global - scale surface evaporation. Water Resources Research, 55, 519–539. https://doi.org/10.1029/2018WR024050

Or, D., Lehmann, P., Shahraeeni, E., & Shokri, N. (2013). Advances in soil evaporation physics—A review. Vadose Zone Journal, 12(4), 1–16. https://doi.org/10.2136/vzj2012.0163

Penman, H. L. (1948). Natural evaporation from open water, bare soil and grass. Proceedings of the Royal Society of London A, 193, 120-145.

Philip, J. R., & de Vries, D. A. (1957). Moisture movement in porous materials under temperature gradients. Eos, Transactions American Geophysical Union, 38(2), 222–232. https://doi.org/10.1029/TR038i002p00222

Prat, M. (1995). Isothermal drying of non-hygroscopic capillary-porous materials as an invasion percolation process. International Journal of Multiphase Flow, 21, 875—892. https://doi.org/10.1016/0301-9322(95)00022-P

Rahimikhoob, A., Behbahani, MR., Fakheri, J.(2012). An evaluation of four reference evapotranspiration models in a subtropical climate. Water Resources Management, 26(10):2867–2881. 10.1007/s11269-012-0054-9

Ransohoff, T. C., & Radke, C. J. (1988). Laminar flow of a wetting liquid along the corners of a predominantly gas-occupied noncircular pore. Journal of Colloid and Interface Science, 121(2), 392–401. https://doi.org/10.1016/0021-9797(88)90442-0

Robock, A., et al. (2013). Evaluation of the North American Land Data Assimilation System over the southern Great Plains during the warm season. Journal of Geophysical Research, 108 (2003). https://doi.org/10.1029/2002JD003245

Sato, Y., Nakajima, S., Shiraga, N., Atsumi, H., Yoshida, S., Koller, T., Gerig, G., Kikinis, R. (1998). Three-dimensional multi-scale line filter for segmentation and visualization of curvilinear structures in medical images. Med Image Anal. Jun;2(2):143-68. doi: 10.1016/s1361-8415(98)80009-1. PMID: 10646760.

Schindelin, J., Arganda-Carreras, I., Frise, E., Kaynig, V., Longair, M., Pietzsch, T., & Schmid, B. (2012). Fiji: An open-source platform for biological-image analysis. Nature Methods, 9(7), 676–682. https://doi.org/10.1038/nmeth.2019

Shahraeeni, E., Lehmann, P., and Or, D. (2012), Coupling of evaporative fluxes from drying porous surfaces with air boundary layer: Characteristics of evaporation from discrete pores, Water Resour. Res., 48, W09525, doi:10.1029/2012WR011857.

Shaw, T. M. (1987). Drying as an immiscible displacement process with fluid counterflow. Physical Review Letters, 59(15), 1671–1674. doi:10.1103/physrevlett.59.1671

Small, E., Badger, A.W., Abolafia-Rosenzweig, R., Livneh, B. (2018). Estimating Soil Evaporation Using Drying Rates Determined from Satellite-Based Soil Moisture Records. Remote Sensing, 10(12), 1945. doi:10.3390/rs10121945

Smith, T.G. Jr; Lange, G.D.; Marks, W.B. (1996) Fractal methods and results in cellular morphology--dimensions, lacunarity and multifractals. J Neurosci Methods. Nov;69(2):123-36. doi: 10.1016/S0165-0270(96)00080-5. PMID: 8946315.

Spittlehouse, D.L. & Black, T.A. (1980). Evaluation of the Bowen ratio/energy balance method for determining forest evapotranspiration. Atmosphere-Ocean, 18:2, 98-116, DOI: 10.1080/07055900.1980.9649081

Stöckle, C., Kjelgaard, J., Bellocchi, G. (2004). Evaluation of estimated weather data for calculating Penman-Monteith reference crop evapotranspiration. Irrigation Science 23(1):39–46. DOI: 10.1007/s00271-004-0091-0

Suzuki, M. and Maeda, S. (1968). ON THE MECHANISM OF DRYING OF GRANULAR BEDS. Journal of Chemical Engineering of Japan, 1(1), 26–31. doi:10.1252/jcej.1.26

Trajkovic, S., Kolakovic, S. (2009). Evaluation of reference evapotranspiration equations under humid conditions. Water Resources Management, 23(14):3057–3067. DOI: 10.1007/s11269-009-9423-4

Trenberth, K.E., Fasullo, J.T., and Kiehl, J. (2009). Earth's global energy budget. Bull. Am. Meteorol. Soc., 90:311–323. doi:10.1175/2008BAMS2634.1

Tuller, M., and Or, D. (2001), Hydraulic conductivity of variably saturated porous media: Film and corner flow in angular pore space, Water Resour. Res., 37(5), 1257– 1276, doi:10.1029/2000WR900328.

Udden, J.A. (1914). Mechanical composition of clastic sediments. GSA Bulletin, 25 (1): 655–744. doi: https://doi.org/10.1130/GSAB-25-655

Vogel, Hannes. (2017). Researches to the CCS storage process "capillary trapping" through 2D micromodel experiments [Master thesis]. Faculty of Geosciences, Geoengineering and Mining, TU Bergakademie Freiberg.

Voburger, T. V., & Raja, J. (1990). Surface finish metrology tutorial (NISTIR 89–4088). Gaithersburg, MD: US Department of Commerce, National Institute of Standards and Technology.

Vorhauer, N., Wang, Y. J., Karaghani, A., Tsotsas, E., & Prat, M. (2015). Drying with formation of capillary rings in a model porous medium. Transport in Porous Media, 110(2), 197–223. https://doi.org/10.1007/s11242-015-0538-1

Wang, Y., Merlin, O., Zhu, G., & Zhang, K. (2019). A physically based method for soil evaporation estimation by revisiting the soil drying process. Water Resources Research, 55, 9092–9110. https://doi.org/10.1029/2019WR025003

Wentworth, C. K. (1922). A Scale of Grade and Class Terms for Clastic Sediments. The Journal of Geology, 30(5), 377–392. doi:10.1086/622910

Wenzel, R. N. (1936). Resistance of solid surfaces to wetting by water. Industrial and Engineering Chemistry Research, 28(8), 988–994. https://doi.org/10.1021/ie50320a024

Willingham, T. W., Werth, C. J., & Valocchi, A. J. (2008). Evaluation of the effects of porous media structure on mixing-controlled reactions using pore-scale modeling and micromodel experiments. Environmental Science & Technology, 42 (9), 3185–3193. https://doi.org/10.1021/es7022835

Witkowska-Walczak, B. (2000). Influence of aggregate size of eutric cambisol and gleyic phaeozem on evaporation. Int. Agrophys., 14(4), 469-475.

Wohl, E., Barros, A., Brunsell, N. et al. The hydrology of the humid tropics. Nature Clim Change, 2, 655–662 (2012). https://doi.org/10.1038/nclimate1556

Yiotis, A. G.; Boudouvis, A. G.; Stubos, A. K.; Tsimpanogiannis, I. N.; Yortsos, Y. C. (2003). Effect of liquid films on the isothermal drying of porous media. Physical Review E, 68(3), 037303–. doi:10.1103/PhysRevE.68.037303

Yiotis, A. G., Salin, D., Tajer, E. S., & Yortsos, Y. C. (2012). Analytical solutions of drying in porous media for gravity-stabilized fronts. Physical Review E, 85(4), 046308. https://doi.org/10.1103/PhysRevE.85.046308

Yiotis, A. G.; Salin, D.; Tajer, E. S.; Yortsos, Y. C. (2012b). Drying in porous media with gravity-stabilized fronts: Experimental results. Physical Review E, 86(2), 026310–. doi:10.1103/PhysRevE.86.026310

Yiotis, A. G. , Tsimpanogiannis, I. N. and Stubos, A. K.(2010). Fractal Characteristics and Scaling of the Drying Front in Porous Media: A Pore Network Study. Drying Technology, 28: 8, 981-990. http://dx.doi.org/10.1080/07373937.2010.497087

Zhao, B., MacMinn, C.W., Juanes, R. (2016). Wettability control on multiphase flow in patterned microfluidics. Proceedings of the National Academy of Sciences, 113 (37) 10251-10256; DOI: 10.1073/pnas.1603387113

Zulfiqar, B., Vogel, H., Ding, Y., Golmohammadi, S., Küchler, M., Reuter, D., & Geistlinger, H. (2020). The impact of wettability and surface roughness on fluid displacement and capillary trapping in 2-D and 3-D porous media: 2. Combined effect of wettability, surface roughness, and pore space structure on trapping efficiency in sand packs and micromodels. Water Resources Research, 56, e2020WR027965. https://doi.org/10.1029/2020WR027965

Zuo, L., Zhang, C., Falta, R. W., & Benson, S. M. (2013). Micromodel investigations of CO2 exsolution from carbonated water in sedimentary rocks. Advances in Water Resources, 53, 188–197. https://doi.org/10.1016/j.advwatres.2012.11.004

Appendix

I. Temperature dependency of the physico-chemical parameters of water and ethanol

Table A1 The saturated vapor pressure, kinematic viscosity of water, and water-air interfacial tension at different temperatures (data are taken from Engineering ToolBox and Dortmund Data Bank).

Temperature	Saturated Vapor Pressure	Kinematic viscosity	Water-Air interfacial tension
[°C]	[mbar]	[$m^2/s*10^{-6}$]	[10^{-3} N/m]
0.01	6.117	1.7918	75.6
10	12.281	1.3065	74.2
20	23.392	1.0035	72.8
30	42.47	0.8007	71.2
40	73.853	0.6579	69.6
50	123.53	0.5531	67.9
60	199.48	0.474	66.2
70	312.02	0.4127	64.4
80	474.16	0.3643	62.6
90	701.82	0.3255	60.8
100	1014.19	0.2938	58.9

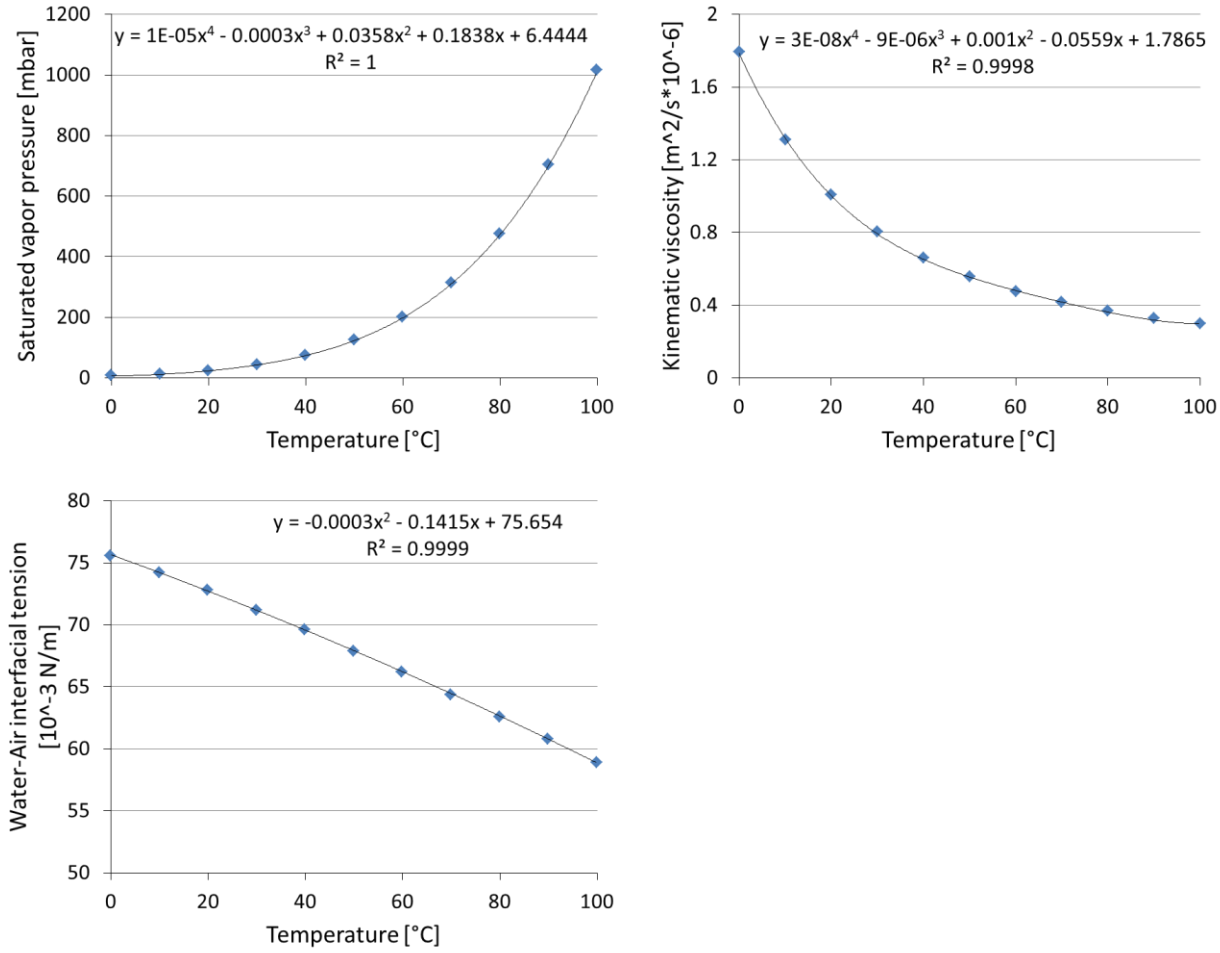

Figure A1. Temperature dependency of the physico-chemical parameters of water.

Table A2 The saturated pressure, kinematic viscosity of ethanol, and ethanol-air interfacial tension at different temperatures (data are taken from Engineering ToolBox and Dortmund Data Bank).

Temperature	Saturated Pressure	Temperature	Kinematic viscosity	Temperature	Ethanol-Air interfacial tension
[°C]	[mbar]	[°C]	[$m^2/s*10^{-6}$]	[°C]	[10^{-3} N/m]
0.15	15.932	5.15	2.0205	20.15	22.29
5.15	22.395	10.15	1.82	30.15	21.48
10.15	31.4	15.15	1.6724	40.15	20.64
15.11	43.02	20.15	1.574	50.15	19.79
20.15	58.65	30.15	1.358	60.15	18.93
25.15	78.69	40.15	1.189	70.15	17.98
30.16	104.6	50.15	1.016	80.15	17.1
35.15	136.72	70.15	0.742	90.15	16.19
40.17	179.16	80.15	0.634	100.15	15.28
45.14	230.58	90.15	0.541	110.15	14.32
50.15	294.56	110.15	0.413	120.15	13.27
55.14	373.02	140.15	0.292	130.15	12.19
60.15	468.39	160.15	0.233	140.15	11.04
65.15	584			150.15	9.88
75.55	934.32			160.15	8.69
78.7	1022.2			170.15	7.52
				180.15	6.32
				190.15	5.11
				200.15	3.94
				210.15	2.76
				220.15	1.71

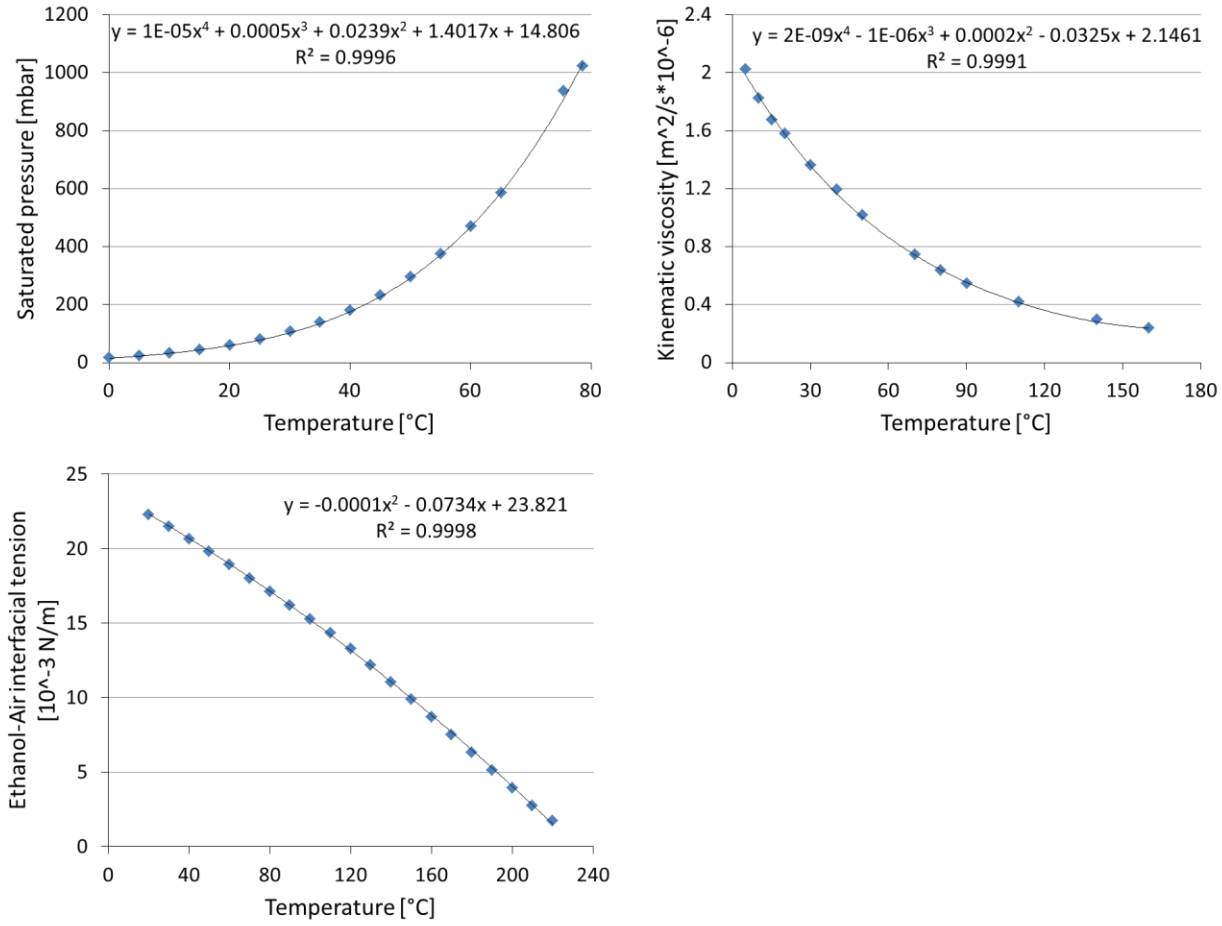

Figure A2. Temperature dependency of the physico-chemical parameters of ethanol.

II. Contact angle dependency of the flow resistance

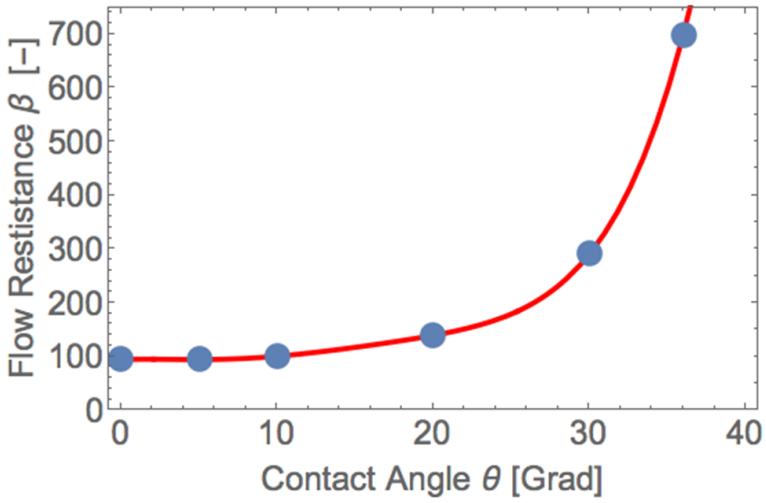

Contact Angle θ [°]	Flow Resistance β [-]
0	93.93
5	93.99
10	100.2
20	139
30	290.7
36	698.2

Figure A3. The contact angle dependence of flow resistance, data are taken from Ransohoff and Radke (1988, Table IV).

III. The contact angle measurement of deionized water and ethanol

Table A3 The measured contact angles of deionized water on Si-SiO_2 wafers and Borofloat glass cover wafers.

	Contact angle measurements of deionized water									
Si-SiO_2 wafer	47.9	43.9	47.4	49	49.8	48.9	47.7	45.2	49.9	50.8
	47.9	44.5	45.6	48.4	50.5	49.1	48.5	45.8	48.9	49.5
Borofloat-glass cover	24.8	18.9	24.9	22	22.6	26.2	19.5	22.4	28.9	21.3
	22.2	22.7	23.4	19.9	22	21.9	24.7	20.8	22.7	

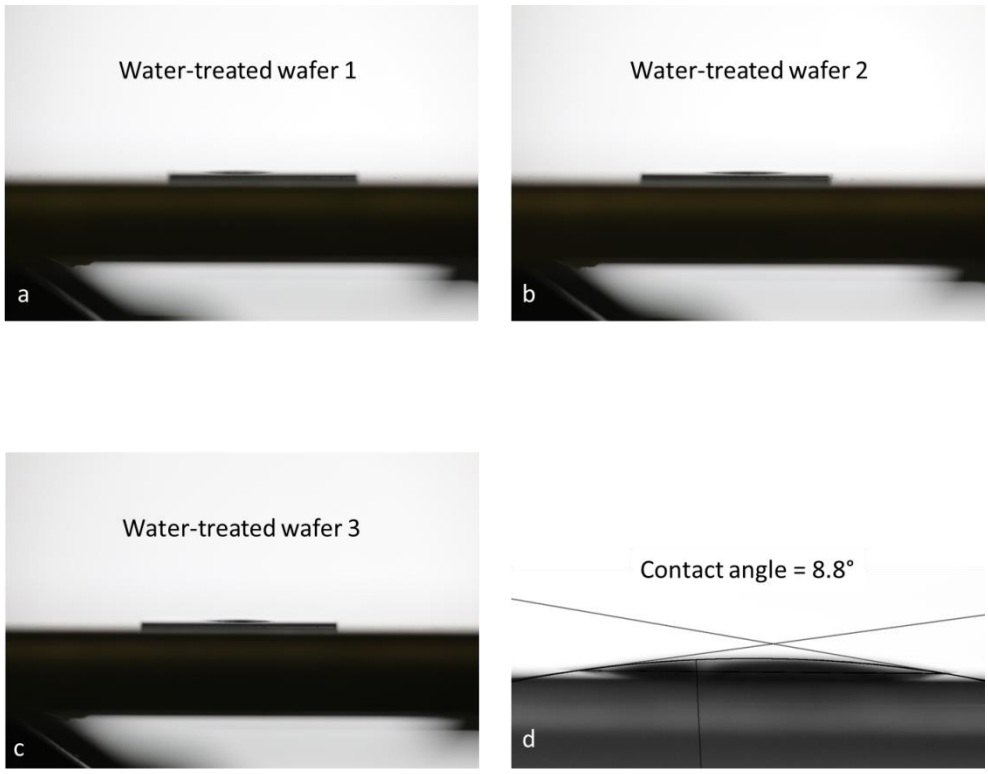

Figure A4. Pure ethanol is partial wetting on the water-treated Si-SiO_2 wafers. Figure a, b and c are three different ethanol droplets, the contact angle can be measured by the ellipse of the magnified flat droplet (d).

IV. The calibration of voltage supply for heating plate

Table A4 Calibration between the supplied voltage to heating plate and the micromodel surface temperature.

Voltage [v]	T_sensor [°C]	T_top [°C]	T_down [°C]	T_left [°C]	T_right [°C]	T_center [°C]	T_mean [°C]
6	37.4	34.8	35.3	34.1	35.2	35.2	34.9
7	41.6	39.5	39.2	38.5	39.6	39.2	39.2
8	46.6	43.6	43.4	41.2	43.4	43.5	43.0
9	51.3	48.3	47.3	47	47.9	48	47.7
10	56.3	52.5	50.6	50.6	52.4	51.7	51.6
11	61.3	57.6	54.6	54.8	57.7	56.4	56.2
12	66.7	62.8	60.4	60.2	62.3	61.9	61.5

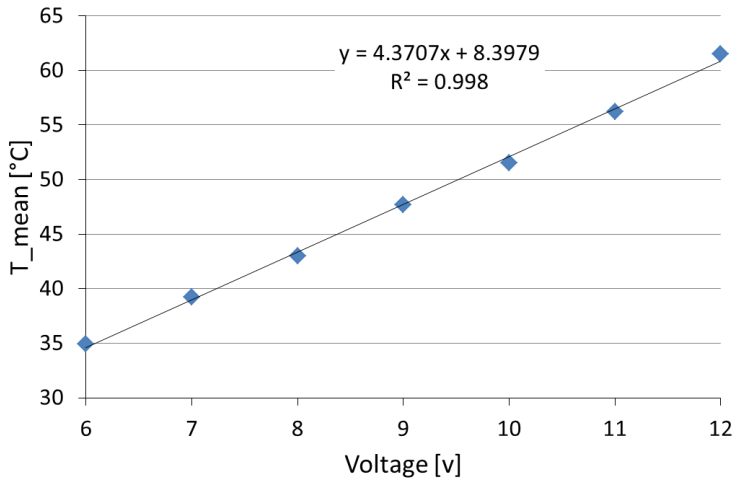

Figure A5. The linear relationship between the supplied voltage and the mean temperature on the micromodel surface.

Table A5 The mean surface temperature with voltage supply of 11.8v.

11.8v No.	T_top [°C]	T_down [°C]	T_left [°C]	T_right [°C]	T_center [°C]	T_mean [°C]
1	62.4	60.3	59.5	58.6	60.8	60.3
2	62.2	59.7	59	59.2	60.7	60.2
3	62.4	61	60	59.5	60.7	60.7
4	62.5	60.7	60.6	59.8	61.1	60.9
5	62.6	61.5	60.3	60	61	61.1
6	62.7	60.8	60.9	60.2	61.3	61.2
7	62.1	60.8	60.3	59.3	61.1	60.7
8	62.7	60.8	59.5	59.3	60.2	60.5
9	63.3	61.2	60.4	59.8	61.6	61.3
10	62.5	60.7	60.3	59.9	61.1	60.9
						60.8

Table A6 The mean surface temperature with voltage supply of 7.8v.

7.8v No.	T_top [°C]	T_down [°C]	T_left [°C]	T_right [°C]	T_center [°C]	T_mean [°C]
1	41.8	41.8	41.1	41	41.6	41.5
2	40.7	41.9	42	40.9	41.5	41.4
3	41.7	42.6	42.6	41.7	42.6	42.2
4	41.7	42.4	42.3	40.7	41.1	41.6
5	41	41.7	42.2	40.7	41.1	41.3
6	41.9	41.9	42.5	41.3	42.5	42.0
7	41.4	42.4	41.4	40.6	41.5	41.5
8	40.7	42	41.3	40.4	42.3	41.3
9	40.1	41	41.3	40	42.2	40.9
10	41	40.8	41.2	40.5	40.9	40.9
						41.5

V. Bubble effect in silicon micromodels

According to a realistic wetting model derived by modifying Wenzel's model, the *complete-wetting* condition (Zulfiqar et al., 2020, Sect. 4.1.1.) is given by:

$$\theta_0 \leq \theta_c, \qquad \text{with } \theta_c = arccos\left(\frac{1-\phi_s}{r_F-\phi_s}\right),$$

where θ_0 is the equilibrium contact angle of the liquid on an ideal flat surface of the same chemical composition (i.e., the intrinsic contact angle) and ϕ_s is the dry part of the surface area. The range of the critical contact angle θ_c is determined by the degree of surface roughness r_F (the ratio of rough surface area to flat surface area). For the smooth surface of Si micromodels ($r_F = 1$, $\theta_c = 0$), complete wetting and is only possible when $\theta_0 = 0$. As we have shown in Chapter 3.2, the measured contact angle of deionized water in silicon micromodel is 35.5°, therefore, the impossibility of complete wetting causes the water in the CF region accumulating as bubbles. As pure ethanol presents strong wettability on the Si-SiO_2 wafers, this bubble effect doesn't occur in ethanol experiments.

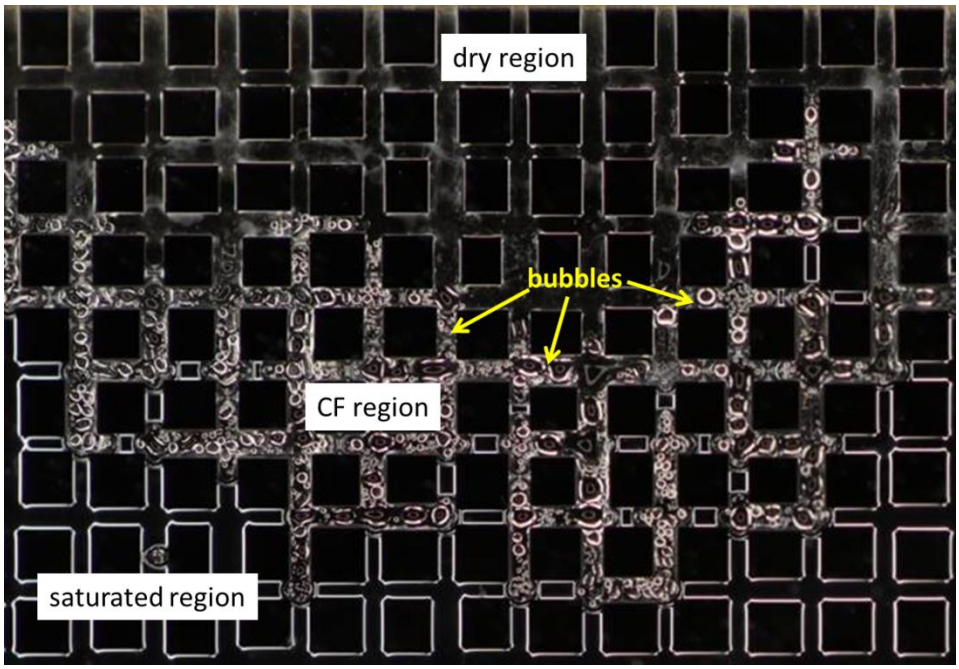

Figure A6. The bubble effect in the corner flow (CF) region of silicon micromodels during water evaporation experiments.

VI. Polynomial fitting of the cumulative mass loss curves

The experimental mass loss curve versus time (e.g. Fig. 4.6) shows the polynomial and square root fit with function

$$m_{loss}(t) = a_1 + a_2 \mathrm{t} + a_3 t^2 + a_4 t^3 + a_5 \sqrt{t},$$

with the best fitting parameters a_1, a_2, a_3, a_4 and a_5.

Therefore, the evaporation rate Q_{ev} in stage 2 can be derived by the derivation of the $m_{loss}(t)$ function,

$$Q_{ev}(t) = a_2 + 2a_3 t + 3a_4 t^2 + \frac{a_5}{2\sqrt{t}}..$$

Declaration

I hereby declare that I completed this work without any improper help from a third party and without using any aids other than those cited. All ideas derived directly or indirectly from other sources are identified as such.

In the selection and use of materials and in the writing of the manuscript I received support from the following persons:

Prof. Dr. Helmut Geistlinger

Persons other than those above did not contribute to the writing of this thesis. I did not seek the help of a professional doctorate-consultant. Only those persons identified as having done so received any financial payment from me for any work done for me.

This thesis has not previously been published in the same or a similar form in Germany or abroad.

_____

Date, signature